Dissertation
submitted to the
Combined Faculties for the Natural Sciences and for Mathematics
of the Ruperto-Carola University of Heidelberg, Germany
for the degree of
Doctor of Natural Sciences

Put forward by

Diplom-Physiker: Tobias Schuster
Born in: Kirchheimbolanden, Germany

Oral examination: 20. June, 2012

Feshbach Resonances and Periodic Potentials in Ultracold Bose-Fermi Mixtures

Referees: Prof. Dr. Markus K. Oberthaler
Prof. Dr. Selim Jochim

Meinem Papa gewidmet.

Zusammenfassung

In der vorliegenden Arbeit werden die Möglichkeiten, stark korrelierte Quantensysteme anhand der Bose-Fermi Mischung von Natrium und Lithium experimentell umzusetzen, untersucht. Zu diesem Zweck wurden die intraspezies Wechselwirkung von Natrium sowie die interspezies Wechselwirkung zwischen Natrium und Lithium erforscht. Durch eine quantitative Analyse des Natrium Feshbach Resonanz Spektrums konnten wir dessen Wechselwirkungseigenschaften präzise bestimmen und insbesondere die Genauigkeit der Energie des letzten gebundenen Zustands um einen Faktor 50 erhöhen. Zur Untersuchung der interspezies Wechselwirkungseigenschaften haben wir einen allgemeingültigen Ansatz entwickelt, dessen Anwendbarkeit wir anhand der Natrium-Lithium Mischung zeigen konnten: Vorzeichen und Größe der Streulänge wurden bestimmt und dieser Wert verwendet, um die Energie des letzten gebundenen Zustands zu bestimmen, was als Ausgangspunkt für die Erklärung des gemessenen Feshbach Spektrums diente. Im Spezialfall Natrium-Lithium konnten wir 23 der 26 beobachteten Resonanzen als d-Wellen einordnen. Dieses unerwartete Ergebnis wurde durch eine Coupled-Channels Rechnung bestätigt, deren Resultate für die Wechselwirkungseigenschaften auch mit den unabhängig experimentell ermittelten Größen übereinstimmen.

Als ergänzende Herangehensweise, um stark korrelierte Systeme zu untersuchen, haben wir unseren experimentellen Aufbau durch ein optisches Gitter ergänzt. Wir konnten Methoden, um die Bandbesetzung zu bestimmen und kohärent zu manipulieren, demonstrieren und den interspezies Energieübertrag auf verschiedene Weisen untersuchen. Die Gitterfrequenz wurde mit besonderem Augenmerk auf die erreichbare Genauigkeit bestimmt. Der ermittelte Wert in Kombination mit den Ergebnissen der Wechselwirkungsanalyse zeigt, dass Fröhlich Polaronen in der ultrakalten Bose-Fermi Mischung von Natrium und Lithium erfolgreich über den Anstieg in effektiver Masse detektiert werden könnten.

Abstract

This thesis investigates the possibilities to experimentally realize strongly correlated quantum systems by means of the sodium-lithium Bose-Fermi mixture. For that purpose, we have studied the intraspecies interactions of sodium as well as the interspecies interactions within the mixture. With a quantitative analysis of the sodium Feshbach spectrum, we were able to refine its scattering properties and in particular improve the accuracy of the last bound state's energy by a factor of 50. For determining the interspecies scattering properties, we developed a widely applicable approach, which we demonstrated by means of the sodium-lithium mixture: We obtained sign and magnitude of the scattering length experimentally and used this value to determine the last bound state energy, which served as the starting point for the explanation of the measured Feshbach spectrum. In the particular case of sodium-lithium we could assign 23 of 26 observed resonances as d-waves. This unexpected result was confirmed by a coupled-channels calculation, which also yielded scattering properties in good agreement with our experimental findings.

As a complementary approach to study strongly correlated systems by directly tuning the interactions, we implemented an otical lattice into our system. Methods to map out the band population as well as coherently manipulate it were demonstrated and interspecies energy transfer was studied in different ways. We investigated the determination of the lattice frequency with regard to the achievable precision. The value obtained combined with the results from the interaction analysis show that in the ultracold Bose-Fermi mixture of sodium-lithium Fröhlich polarons could be observed succesfully via detecting the increase in effective mass.

Contents

1. Introduction

Der Weg entsteht im Gehen.

Reinhold Messner

Since the first experimental realization of Bose-Einstein-Condensation in 1995 [1, 2], the research field of ultracold atomic gases has been growing rapidly. Whereas the first experiments investigated rather weakly interacting systems, after some years there were several developements making it possible to realize strongly interacting systems, which are in the focus of interest of today's ultracold atom research [3].

A system is called strongly interacting if its interaction energy E_{int} is much larger than its kinetic energy E_{kin}, i. e. $E_{\mathrm{int}}/E_{\mathrm{kin}} \gg 1$. In contrast to this case, for a simplified description of gases one often considers the ideal gas, which is by definition non-interacting. To take also interactions into account, most gases can – outside of critical points – be correctly described by the van der Waals equation. This regime of weak interactions is both experimentally and theoretically well understood. To be able to investigate more complicated systems, tools have been developed for tuning ultracold quantum gases into the strongly interacting regime, where the strong correlations make a correct theoretical description more challenging. On the one hand, Feshbach resonances [4, 5] make it possible to get a direct handle on the interaction energy E_{int}. On the other hand, the use of optical lattice systems [6] gives access to experimentally tune the ratio $E_{\mathrm{int}}/E_{\mathrm{kin}}$, e. g. by lowering the dimensionality of the system [7, 8].

These developments paved the way to realize the long-standing proposal of a quantum simulator [9] in the field of ultracold atom research: In 1982, R. P. Feynman showed that the computation time 'classical' computers require to simulate a quantum system scales exponentially with the size of its Hilbert space. To circumvent this problem, he proposed to use a so-called quantum simulator, on which the Hamiltonian of the system of interest could be emulated. A famous example, where in an ultracold atom system a problem of condensed matter has been tackled and solved this way, are imbalanced Fermi gases: It was well-known that for sufficiently strong interactions, ultracold Fermi gases of two spin states will show superfluidity induced by a BCS-like pairing mechanism [10, 11, 12]. But it had not been clear, which imbalance between the two spin states is necessary to destroy this superfluidity

completely. In ultracold atom systems, where one – in contrast to condensed matter systems – is able to set an arbitrary imbalance at will, this Clogston-Chandrasekhar limit [13, 14] has been mapped out [15], being an impressive demonstration of practicability of the quantum simulator.

In the extreme limit of imbalance, where one impurity of spin down is immersed in a sea of spin up Fermions, a quasiparticle, the so-called Fermi polaron is formed [16]. One can think of it as a particle, which drags a cloud of particle-hole excitations with it due to its strong interaction with the atoms in the other spin states. This gives rise to an increase in effective mass $m^* > m$, which could be measured experimentally by mapping out the resulting shift in oscillation frequency [17]. Until recently, experiments have only investigated Fermi polarons composed of equal [16] and different [18] fermionic atom species. The polaron concept has first been introduced in condensed matter theory [19], where it describes an electron travelling through a (ionic) crystal. The coulomb interaction results in a displacement of the atomic cores, i. e. the lattice sites, which can be described by lattice phonons. The quasiparticle formed by the coupled electron-phonon system is called polaron and can be attributed an effective mass $m_e^* > m_e$ being bigger than the bare electron mass m_e.

For ultracold atomic gases, there are proposals to simulate this polaronic Hamiltonian using an impurity atom immersed in a bosonic background [20, 21]: In comparison to the condensed matter system, the phonons correspond to the Bogoliubov modes of the condensate and the role of the electron is taken by the impurity atom. As long as one only considers the single polaron case, there is no difference between bosonic and fermionic impurities. To express the strength of the coupling between impurity and phonons, the commonly used parameter is denoted α, which in the case of an ultracold atom system reads

$$\alpha = \frac{a_{IB}^2}{a_{BB}\xi}\,. \tag{1.1}$$

Here, a_{IB} denotes the interspecies scattering length between impurity and background atoms[1], a_{BB} the intraspecies scattering length of the bosons and $\xi = 1/\sqrt{8\pi n a_{BB}}$ the condensate healing length with n being the bosonic atom's density. We see that α, whose value is fixed for a condensed matter system, can be tuned by changing e. g. the scattering lengths a_{IB} or a_{BB}. Of special interest is the strongly interacting regime $\alpha > 1$, where there are different theoretical approaches to solve the problem, e. g. variational Feynman path-integral [21] and quantum monte carlo treatment [22]. Those calculations, which have been performed for different experimental situations, could be validated by experiment, in particular their results for the effective mass m^*. The impact of a deep understanding of the polaron problem outreaches the field of ultracold atom systems: As they are considered to

[1]Depending on the context, in this thesis the abbreviations a_{IB} (Impurity-Boson) and a_{BF} (Bose-Fermi) are used equivalently, as our impurity ^{6}Li is a fermion.

play an important role in the understanding of high-T_c superconductors [23], results of such measurements would also be highly interesting for the condensed matter community.

So far, the investigation of polarons in Bose-Fermi mixtures has only been done in one dimension [24]. To be able to study them in our experiment, which uses bosonic sodium and fermionic lithium, we first have to understand the tuning properties of a_{BB} and a_{IB}. Moreover, the experimental tools to detect a small increase in effective mass $m^* > m$ have to be developed. The implementation of a species selective optical lattice does not only give the possibility to measure precisely the oscillation frequency of lithium $\omega^* \propto 1/\sqrt{m^*}$, but also provides the versatility to investigate physics in lower dimensions.

Contents of this Thesis

The first part of this thesis deals with Feshbach resonances, i. e. the tuning properties of a_{BB} and a_{IB} are investigated in detail. For that purpose, we start with basic scattering theory in chapter 2, where important terms as the scattering length are introduced and its connection to repulsive and attractive interactions within a simple mean-field picture is derived. In chapter 3, we give a short introduction to our experimental setup, with a focus on the preparation of different spin state combinations. Loss mechanisms in ultracold samples are treated theoretically in detail and the results are applied to interpret experimentally obtained loss curves. As a main result of this chapter, the difference between the sodium-lithium singlet and triplet interspecies scattering lengths is determined.

In chapter 4, Moerdijk and asymptotic bound-state model are introduced and applied to develop an understanding of the sodium intraspecies Feshbach resonance spectrum. Starting with a model only involving s-wave resonances, we extend our theory to higher partial waves and compare our results to a coupled-channels calculation.

Chapter 5 first presents measurements performed to understand the sodium-lithium interspecies Feshbach resonance spectrum. We obtain sign and absolute value of a_{IB} experimentally and relate it to the least bound state energy, which finally serves as a guidance to develop an explanation of the measured Feshbach resonances, most of which are assigned d-wave resonances. The results of a coupled-channels calculation confirm the experimental data and our assignment of resonances with the asymptotic bound-state model.

In the second part of this thesis, Bose-Fermi mixtures in periodic potentials are investigated. In order to design a species selective optical dipole trap in form of an optical lattice in chapter 6, we derive different criteria which our system has to fulfil. Starting with analytic approximations, we extend our picture to a full quantum-mechanical treatment of the periodic potential. First results of the effects of the periodic potential on sodium and lithium are shown and analyzed quantitatively.

As a tool to investigate the states in the optical lattice in detail, we introduce Brillouin

zone mapping in chapter 7, a technique which allows to map out the population of the different Bloch bands. By adding a sodium background, we are able to optimize the lithium lattice loading process and thus prepare atoms only in the lowest Bloch band. Starting from that state, we show in chapter 8 how we can excite the lithium atoms in a controlled way and analyze the resulting state in terms of Bloch states. The interspecies energy transfer in the Bose-Fermi mixture is analyzed quantitatively, with the dynamics of the process giving the absolute value of a_{IB} in agreement with the results of the first part of the thesis. Finally, we show our control of the optical lattice by demonstrating Rabi oscillations.

The Outlook gives a perspective on the physics beyond this thesis, which can be investigated on basis of the results presented in the following.

Part I.

Feshbach Resonances

The first part of this thesis deals with Feshbach resonances in the NaLi mixture. In an introduction to basic scattering theory of ultracold atoms the important concept of the scattering length is introduced. We show how we prepare different spin mixtures and analyze their losses both theoretically and experimentally.
By means of the Feshbach spectrum of sodium, we introduce the Moerdijk and ABM models to explain our findings. For the sodium-lithium mixture, we present different measurements to obtain information about sign and magnitude of the scattering length. Guided by these results, we develop a model explaining all 26 NaLi resonances observed experimentally.

2. Scattering of Ultracold Atoms

In this chapter, we will investigate scattering of ultracold atoms from the theoretical point of view, starting with the van der Waals potential as an example of a typical interatomic potential. The scattering length a is introduced and exemplarily calculated using the box potential as a simple model. With the results, we connect the sign of a to repulsive and attractive interactions and show how they come into play in mean-field theory. The chapter concludes by explaining the underlying principles of a Feshbach resonance used to tune the scattering length.

2.1. Hamiltonian

As scattering processes of two atoms can be highly complex processes [25], we first want to investigate in which regime our experiments take place, i. e. which approximations can be made in order to simplify the description of interactions.

The interaction potential $U(r)$ between two alkali atoms, which have one electron in their outer shell, can be divided into two regions: For small interatomic distances, the potential is repulsive due to Pauli blocking of the electrons and the repulsive interaction between the positively charged nuclei. As this part strongly depends on the two electrons' spin state, which can be a singlet $S = 0$ or triplet $S = 1$, one can assign each S a different potential $U_S(r)$ as depicted in figure 2.1 a). The underlying reason for the different potentials is the required asymmetry of the two electrons' wavefunction: A spin triplet (singlet) is symmetric (antisymmetric), thus the spatial wavefunction must be antisymmetric (symmetric). This means, that the electrons have a higher probability to be found between the atoms in a spin singlet, thus they bind the two positively charged atom nuclei, which form the molecule, more strongly and so the singlet potential is deeper than the triplet. As an example, in the case of Na_2 there are $\nu_X = 64$ singlet and $\nu_a = 14$ triplet states [26], when there is no magnetic field applied.

The long-range part of the potential, which is the same for both singlet and triplet, is given by the induced dipole-dipole interaction between the atoms, scaling as

$$U(r) = -\frac{C_6}{r^6} \tag{2.1}$$

with the van der Waals coefficient C_6 given by the details of the atoms' electronic configu-

ration. The associated length scale scale of this potential is given by

$$R_{\mathrm{vdW}} = \frac{1}{2}\left(\frac{2\mu C_6}{\hbar^2}\right)^{1/4}, \tag{2.2}$$

where μ denotes the effective mass of the two interacting atoms. With typical values for the van der Waals coefficient C_6, we get an R_{vdW} ranging from $10a_0$ to $100a_0$ for the alkalis [5], where a_0 denotes the Bohr radius[1].

This value can be compared to other typical length scales of our system. Dealing with atom densities ranging from $n = 10^{12}\,\mathrm{cm}^{-3}$ in a thermal cloud to $n = 10^{15}\,\mathrm{cm}^{-3}$ in a BEC, the ratio of R_{vdW} to the mean interatomic distance $R_{\mathrm{vdW}} \cdot n^{1/3}$ is well below 0.1, which we call *dilute*.

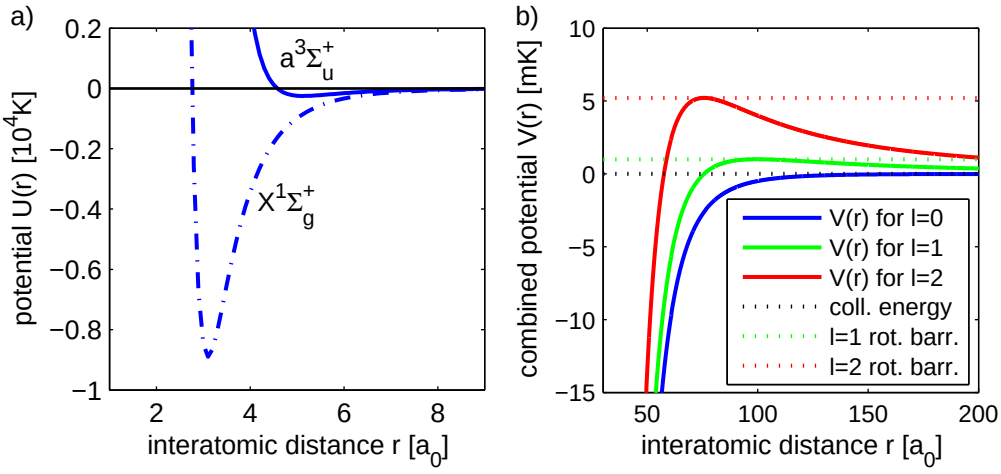

Figure 2.1.: ***a)*** *Van der Waals potential $U_S(r)$ for electrons in a singlet $S = 0$ and triplet $S = 1$ configuration (values taken from [26]). We see that the singlet state, spectroscopically labeled $X^3\Sigma_g^+$, is much deeper than the triplet state $a^3\Sigma_u^+$.* ***b)*** *Effective interatomic potential $V(r)$ for different angular momenta l. Note the different energy and distance scales in a) and b).*

Another length scale is given by the thermal de Broglie wavelength $\lambda_T = \sqrt{\frac{2\pi\hbar^2}{mk_BT}}$, which gets at the onset of quantum degeneracy at temperatures of about $1\,\mu$K on the order of the interparticle spacing $\lambda_T = \mathcal{O}(0.1...1)\,\mu$m [27]. Thus the details of the interaction potential can not be resolved in cold collisions and so a quantum mechanical treatment of the scattering processes is unavoidable.

[1] In the following, we will use the abbreviations for constants as listed in appendix A and will for reasons of brevity not explicitly introduce them unless required.

As to be found in every basic quantum mechanics textbook [28], a partial wave expansion[2] of the atoms' scattering wave function yields for its radial part $R_l(r)$ with angular momentum l

$$R_l''(r) + \frac{2}{r} R_l'(r) + \frac{2\mu}{\hbar^2} \left[E - V(r) \right] R_l(r) = 0 \,, \tag{2.3}$$

with

$$V(r) = U(r) + \frac{\hbar^2 l(l+1)}{2\mu r^2} \tag{2.4}$$

being the sum of bare interaction potential and rotational term, as sketched in figure 2.1 b). The resulting rotational barrier has a height of

$$U_{\mathrm{rot}} = \frac{1}{\sqrt{2C_6}} \left(\frac{\hbar^2 l(l+1)}{3\mu} \right)^{3/2} \tag{2.5}$$

which is for the p-states in sodium and lithium 1 mK and 8 mK, respectively. With our atomic samples having temperatures of around 1 μK, we see that for a basic understanding of the collisions it is sufficient to consider s-wave scattering only.[3]

2.2. Scattering Length

To gain first insight into the mechanisms of scattering, it is sufficient to replace the real potential by some model potential with wavefunctions that can be calculated easily. As we will see later, despite of this simplification the basic physics is still preserved.

A potential with well known energy eigenfunctions is the square well potential

$$U(r) = \begin{cases} -V_0 & \text{for} \quad 0 \le r \le r_0 \\ 0 & \text{for} \quad r > r_0 \end{cases} \tag{2.6}$$

Plugging this potential into eq. (2.3) and substituting $\chi_l(r) = r \cdot R_l(r)$, we get the one-dimensional Schrödinger equation

$$\chi_l'' + [\varepsilon - \widetilde{V}(r)] \chi_l(r) = 0 \tag{2.7}$$

with $\varepsilon = 2\mu E/\hbar^2$ and $\widetilde{V}(r) = 2\mu V(r)/\hbar^2$. With $E = \frac{\hbar^2 k^2}{2\mu}$, the solution of eq. (2.7) for $V_0 = 0$, i. e. free particles, reads

$$\chi_l(r) = c \cdot \sin\left(kr + \eta_0\right). \tag{2.8}$$

[2]The kind of partial wave expansion applied here is only valid in the case of a spherically symmetric potential, which is justified in our case due to our atoms not having a permanent dipole moment. Note that there are also numerous cold atoms experiments where the dipolar interactions are in the focus of interest [29, 30] and thus scattering has to be analyzed differently.

[3]As we will see later in chapter 4 and 5, this is not completely true, as e. g. the dipole-dipole interaction couples $l = 0$ to $l = 2$ states.

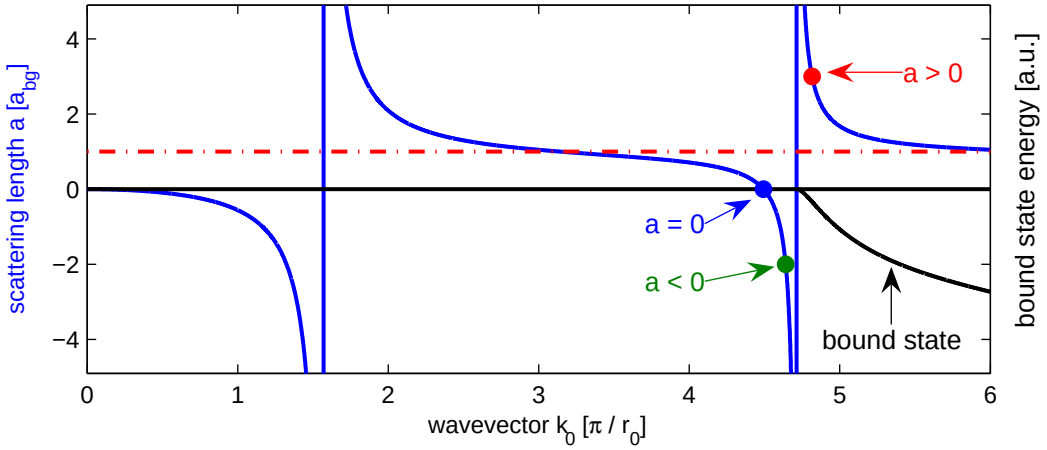

Figure 2.2.: *Scattering length a according to eq. (2.11) in dependence of the wavevector k_0, latter being obtained from the potential depth V_0 as $k_0 = \sqrt{2\mu V_0}/\hbar$. The wavefunctions for the three highlighted points are shown in figure 2.3. Schematically shown is also the energy of the universal bound state (black line) emerging for $a > 0$.*

In the following we want to show how we can understand the underlying scattering physics from the parameter η_0.

As a first easy example, we choose $V_0 = -\infty$, which is the so-called hard-sphere potential, meaning that the two atoms scatter like classical billiard balls. As wavefunction, we get

$$\chi_0(r) = \begin{cases} 0 & \text{for} \quad 0 \leq r \leq r_0 \\ c \cdot \sin\left(k(r - r_0)\right) & \text{for} \quad r > r_0 \end{cases} \tag{2.9}$$

We note that $\eta_0 = -k \cdot r_0$ to make the wavefunction continuous at $r = r_0$. By defining $a = \lim_{k \to 0} -\eta_0/k$, we introduce the scattering length a, which is one of the most important parameters to characterize the strength of interactions in ultracold quantum gases, as we will see later. In this simple case of the hard-sphere potential, we see that a exactly coincides with r_0, the range of our potential, i. e. the scattering length reduces the complex quantum scattering processes to one parameter used to describe classical scattering.

In the following, we will consider the case of a potential well with finite depth $V_0 = \frac{\hbar^2 k_0^2}{2\mu} > 0$. As the wavefunction is now allowed to penetrate into the range of the potential, it reads

$$\chi_0(r) = \begin{cases} c_1 \sin\left(k_+ r\right) & \text{for} \quad 0 \leq r \leq r_0 \\ c_2 \sin\left(kr + \eta_0\right) & \text{for} \quad r > r_0 \end{cases} \tag{2.10}$$

with $k_+^2 = k_0^2 + k^2$. Here we already set the phase of the wavefunction inside the potential to zero, as $\chi_l(0) = 0$ is required due to the regularity of $R_l(0)$. Moreover, the wavefunction has to be continuously differentiable at $r = r_0$ and thus we get for the scattering length

$$a = r_0 - \frac{\tan k_0 r_0}{k_0} \tag{2.11}$$

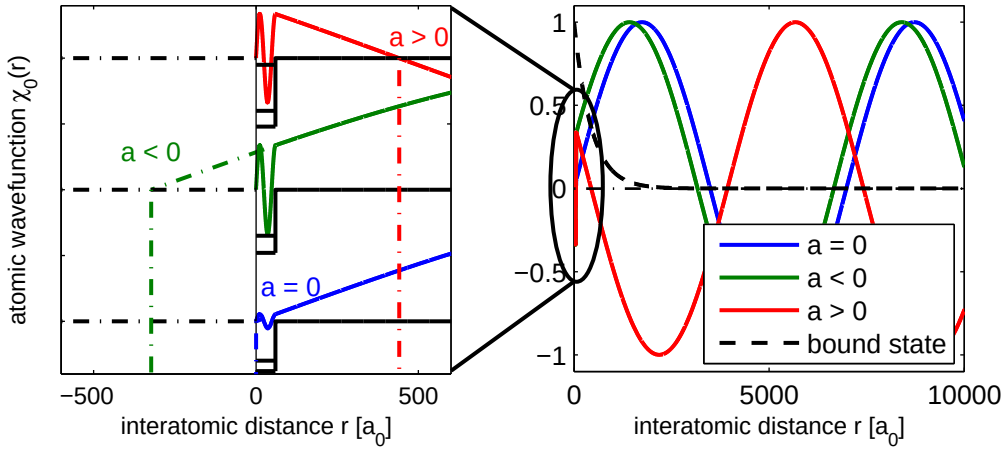

Figure 2.3.: *Wavefunctions $\chi_0(r)$ for the points highlighted in figure 2.2, the left graph being a zoom-in for small interatomic distances r. We see that for attractive/repulsive interactions $a \lessgtr 0$, the wavefunction is being dragged into/out of the origin (green/red line), whereas for $a = 0$ (blue line) the wavefunction looks almost as there is no interatomic potential present. Furthermore, the weakly bound universal halo dimer (black dashed line) is shown. The graphs have been obtained using typical experimental parameters for collision energy corresponding to $T \sim 1\,\mu$K and potential range $r_0 = 60a_0$.*

which is visualized in figure 2.2 with the corresponding wavefunctions shown in figure 2.3.

We see that the points where $k_0 r_0 = \pi/2 + n\pi$ are of special interest, as a is diverging there. To get more detailed insight into that special configuration, we consider a bound state of the square well under consideration, i. e. a state with $\varepsilon_b = -\frac{\hbar^2 k^2}{2\mu} < 0$. The solution of the one-dimensional Schrödinger equation (2.7) now reads

$$\chi_0(r) = \begin{cases} c_1 \sin(k_- r) & \text{for} \quad 0 \leq r \leq r_0 \\ c_2 e^{-kr} & \text{for} \quad r > r_0 \end{cases} \tag{2.12}$$

where $k_-^2 = k_0^2 - k^2$. The requirement of continuous differentiability now yields $k_- \cot(k_- r_0) = -k$, which in the limit of weakly bound states $k/k_0 \to 0$ is readily solved by $k_0 r_0 = \pi/2 + n\pi$, which we identify as being coincident with the values of diverging a. Calculating the binding energy for $a \gg r_0$, we get using eq. (2.11)

$$\varepsilon_b = -\frac{\hbar^2}{2\mu a^2}\,. \tag{2.13}$$

The range of validity of eq. (2.13) is called the *universal regime*, as the state and thus the physics can be described by one parameter, the scattering length a, only. This can also be understood intuitively by considering the wavefunction of this weakly bound state for large r,

$$\chi_0(r) = \sqrt{\frac{2}{a}} e^{-r/a}\,, \tag{2.14}$$

which describes a weakly bound halo dimer [5]. In figure 2.3 we see that in this state the probability to find the atoms is mostly located beyond the classical turning point r_0 of the potential, and in this range a is the only parameter needed to describe the wavefunction. Furthermore, the meaning of the scattering length is highlighted: At temperatures around $1\,\mu$K as achieved in our experiment, the atomic wavefunction is not able to resolve the structure of the potential, but its effect can be captured by the phase shift η_0 which the atoms aquire during a collision. Note that although a diverges, η_0 stays finite due to the finite temperatures and resulting finite k we deal with.

2.3. Mean-Field Energy

With a potential being attractive for all r_0 and V_0, it is not obvious how to get repulsive interactions between the atoms. As shown in introductory books to ultracold atom theory [31], the full potential $V(\vec{r})$ can be replaced by a contact interaction

$$V(\vec{r}) = \frac{4\pi\hbar^2 a}{m}\delta(\vec{r})\,, \tag{2.15}$$

which gives rise to an interaction energy $E_{\text{int}} \propto a$. One sees how the sign of the scattering length a connects to an energy change due to collisions and thus gives rise to repulsive or attractive interactions.

In the following, we want to develop a picture how this result, which is rigorously derived by means of quantum field theory, can be understood in an intuitive picture. For that purpose, we consider the two particles being trapped in an external, infinitely high box potential of size R, where their wavefunction according to eq. (2.10) reads for $r \gg r_0$

$$R_0(r) = \frac{c}{kr}\sin\left(k(r-a)\right). \tag{2.16}$$

With the boundary condition of $R_0(R) = 0$, we get for the energies in the interacting and noninteracting case

$$E = \frac{\hbar^2}{2\mu}\left(\frac{\tilde{n}\pi}{R-a}\right)^2 \tag{2.17}$$

and

$$E = \frac{\hbar^2}{2\mu}\left(\frac{\tilde{n}\pi}{R}\right)^2, \tag{2.18}$$

respectively, with $\tilde{n} \in \mathbb{N}$. From a Taylor expansion of the difference of eqs. (2.17) and (2.18), we get an energy shift by interactions of

$$\delta E = \frac{\hbar^2}{\mu}\frac{(\tilde{n}\pi)^2}{R^3}a. \tag{2.19}$$

Now, we want to relate this energy shift in the two-body problem with the corresponding many-body-system containing N atoms. From the normalization condition of the wavefunction,

$$\rho_0 \underbrace{\int \frac{\rho(r)}{\rho_0} d^3r}_{V_{\text{eff}}} = 1, \tag{2.20}$$

we get by using eq. (2.16) and $\rho(r) = |R_0^2(r)|$ for the effective volume occupied by the two particles $V_{\text{eff}} = \frac{2}{\pi\tilde{n}^2} R^3$. Inserting this into the result for the energy shift eq. (2.19) and noting that for identical particles with mass $m = 2\mu$ there are $N^2/2$ pairs of atoms in our system, we end up with a total energy increase due to interactions of

$$\Delta E = \frac{2\pi\hbar^2}{m} \frac{N^2}{V} a, \tag{2.21}$$

which translates into a chemical potential of

$$\mu = \frac{\partial E}{\partial N} = \frac{4\pi\hbar^2}{m} na. \tag{2.22}$$

We see that at positive scattering lengths a, it costs energy to add a particle to the system of density n, which corresponds to a repulsive interaction. From figure 2.3 we see that this is the case when there is a bound state just below threshold, i. e. the incoming atom can be considered as being pushed out of the origin.

We note that in the case of mixtures of distinguishable particles, e. g. fermions n_F in a bath of bosons n_B, eq. (2.22) reads

$$\mu_F = \frac{\partial E}{\partial N_F} = \frac{2\pi\hbar^2}{\mu_{BF}} n_B a_{BF}. \tag{2.23}$$

Here, $\mu_{BF} = m_B m_F/(m_B + m_F)$ denotes the effective mass and the subscripts B and F denote bosons and fermions, respectively. The approximation made in deriving the chemical potential due to interactions is the so-called mean-field approximation: Instead of considering the whole many-body problem, one considers only the one-body problem of a single atom in the external mean field of the others. This approximation breaks down if e. g. interactions become strong, i. e. not only two-, but also three-body processes gain importance.

2.4. Simple Model of a Feshbach Resonance

To lead over to an experimentally more realistic situation, we have to go from a single- to a two-channel description of the problem. As sketched in figure 2.4 a), the incoming atoms in a certain spin state called entrance or open channel interact via the corresponding background potential $V_{\text{bg}}(r)$. If there is a closed channel which the entrance channel couples to and

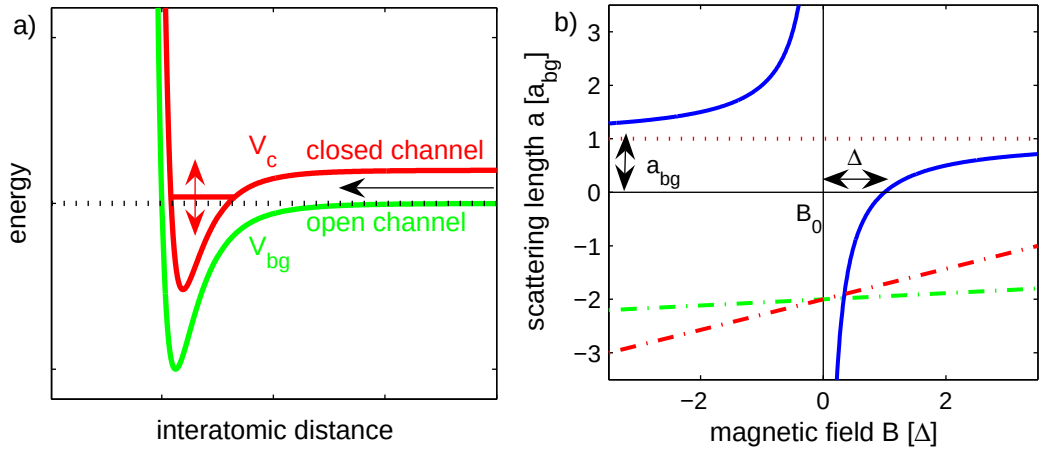

Figure 2.4.: ***a)*** *During a collision, two atoms in the open channel (green) can be coupled to a closed channel (red). The coupling can be resonantly enhanced by tuning the bound state energy of the closed channel appropriately.* ***b)*** *Scattering length a as described by eq. (2.24) in dependence of the magnetic field. Additionally shown are the energies of open (green) and closed (red) channel having different magnetic moments.*

the associated potential $V_c(r)$ has a bound state, this can give rise to a Fano-Feshbach resonance [32, 33] if the bound state's energy is tuned near the collision energy of the incoming atoms. The tuning can e. g. be done by an external magnetic field, if open and closed channel have a difference in magnetic moments $\delta\mu \neq 0$. To develop an intuition for the magnetic tuneability with the simplest possible model, we reduce the two-channel problem to a one channel model with a potential of width r_0 depth $V_0 = \delta\mu \cdot B$. This way, we get a potential of magnetically tuneable depth an can thus refer to the previously derived results. Denoting B_0 as the field at which the bound state is tuned in resonance, we can expand eq. (2.11) around that value and get

$$a = a_{\mathrm{bg}} \left(1 - \frac{\Delta}{B - B_0}\right) . \tag{2.24}$$

Here, we introduced the background scattering length $a_{\mathrm{bg}} = r_0$ and the width of the resonance $\Delta = -\hbar^2/(2\mu r_0^2 \delta\mu)$. Although here it has formally only been derived for the case of a box potential, eq. (2.24) provides the general form of a so-called magnetically tuneable Feshbach Resonance [5], which is visualized in figure 2.4b). Note that eq. (2.24) has been derived using $k_0^2 \propto B$ resulting in the resonance width Δ being independent of the potential depth $V_0 \propto k_0^2$, although in figure 2.2 the widths of the different resonances are obviously not all the same, which is due to the x-axis being given there in units of k_0 and not in dependence of the magnetic field B as in figure 2.4.

In chapter 4 and 5 we will learn more about Feshbach resonances by means of the exam-

ples sodium and sodium-lithium. The knowledge about the characteristics of the scattering lenght a will prove important to analyze density profiles as well as scattering dynamics of trapped ultracold samples.

3. Experimental Setup to Measure Feshbach Resonances

Unlike the title of this chapter might suggest, we will not give an introduction to the technical details of our machine, which can be found in previous diploma and PhD theses [34, 35, 36, 37, 38]. We will rather explain the different experimental techniques, which will be used later to adress fundamental physical questions. Especially for a deep understanding of the Feshbach resonance spectra, profound knowledge of the atoms' nature is crucial: The characteristics of their different spin states in an external magnetic field will be studied by means of a derivation of the Breit Rabi formula. Furthermore, we will show how we can transfer between those states and check the results afterwards using a Stern-Gerlach technique, both being of crucial importance for recording the Feshbach spectrum in chapter 5.

Important for our experiments is also a deep understanding of loss processes, which we will first analyze in detail theoretically in different regimes. To understand the experimentally measured loss curves, we then give an overview of atomic density distributions in traps, which we apply to the homonuclear sample. Using the theory derived before, we are able to extract information about the sodium-lithium scattering lenght from loss measurements of heteronuclear samples.

3.1. Alkali atoms in magnetic fields

As known from basic atomic physics [39], the state of an atom can be characterized by its quantum numbers, which read for the alkalis having one electron in the outer shell:

- n: The main quantum number characterizes the electron's energy state.
- l: The orbital angular momentum of the electron
- s: The electron spin, $s = 1/2$ for the alkalis
- j: The total electron angular momentum $j = |l - s|, ..., |l + s|$
- i: The nuclear spin
- f: The atoms' total spin $f = |i - j|, ..., |i + j|$

Moreover, each of the angular momentum quantum numbers $k \in \{l, s, j, i, f\}$ can be assigned another quantum number m_k being the projection of the angular momentum on the quantization axis, where latter can e. g. be given by an external magnetic field B. Most generally, the state of the alkali atom can be written as $|n, l, s, j, i, f, m_F\rangle$, but as we are dealing with alkali atoms ($s = 1/2$) in the ground state[1] ($n = 2(3)$ for Li(Na), $l = 0$), it is sufficient to characterize the state of the atom with fixed i by $|f, m_f\rangle$ in the limit of small B or $|m_s, m_i\rangle$ in the limit of large B, respectively. One should keep in mind that $m_f = m_s + m_i$ is a conserved quantity for almost all Hamiltonians we deal with in the following.

With the assumptions made, the Hamiltonian relevant for the description of an alkali atom in a magnetic field consisting of the hyperfine Hamiltonian H_{hfs} and the Zeeman Splitting H_{Zeeman} reads [39]

$$H_{\text{hfs}} + H_{\text{Zeeman}} = \frac{a_{\text{hfs}}}{\hbar^2} \vec{s} \cdot \vec{i} + (g_s m_s + g_i m_i) \frac{\mu_B B}{\hbar} \,. \tag{3.1}$$

Here, a_{hfs} denotes the hyperfine constant, g_s and g_i the gyromagnetic ratio of electron and nucleus, respectively. In the following, we want to diagonalize this Hamiltonian and discuss the resulting energy eigenstates from an experimental point of view.

For the socalled stretched states $|f = i + 1/2, m_f = \pm f\rangle$, the Hamiltonian is already diagonal with the eigenvalues $E = a_{\text{hfs}} \frac{i}{2} \pm (g_s/2 + i g_i) \mu_B B$. For all other states, the analysis is more involved. First, we rewrite the term $\vec{s} \cdot \vec{i}$ as

$$\vec{s} \cdot \vec{i} = s_z \cdot i_z + \frac{1}{2} \left(s_+ i_- + s_- i_+ \right) \tag{3.2}$$

with the spin lowering and raising operators $s_\pm = s_x \pm \mathtt{i} s_y$ and $i_\pm = i_x \pm \mathtt{i} i_y$. Considering the properties of these operators [40],

$$j_\pm \left| j, m_j \right\rangle = \hbar \sqrt{(j \mp m_j)(j \pm m_j + 1)} \left| j, m_j \pm 1 \right\rangle \tag{3.3}$$

with $j = i, s$, we see that Hamiltonian eq.(3.1) only interconnects the states $|m_s, m_i\rangle = |1/2, m_f - 1/2\rangle$ and $|m_s, m_i\rangle = |-1/2, m_f + 1/2\rangle$. Thus, determining the eigenenergies reduces to the diagonalization of

$$\begin{pmatrix} \frac{a_{\text{hfs}}}{2}(m_f - \frac{1}{2}) + \left(\frac{g_s}{2} + g_i(m_f - \frac{1}{2})\right) \mu_B B & \frac{1}{2}\sqrt{(i + \frac{1}{2})^2 - m_f^2} \\ \frac{1}{2}\sqrt{(i + \frac{1}{2})^2 - m_f^2} & \frac{-a_{\text{hfs}}}{2}(m_f + \frac{1}{2}) + \left(-\frac{g_s}{2} + g_i(m_f + \frac{1}{2})\right) \mu_B B \end{pmatrix} \tag{3.4}$$

[1] During the MOT cooling stage and the final absorption imaging, of course the atoms will also be in their excited state, as described in [37]. But for the physics of interest in this thesis treating the atoms in their ground state is sufficient.

With $x = \frac{(g_s - g_i)}{a_{\mathrm{hfs}}(i+1/2)}\mu_B B$, the resulting eigenenergies read

$$E(B) = -\frac{a_{\mathrm{hfs}}}{2} + g_i m_f \mu_B B \pm \frac{a_{\mathrm{hfs}}(i+1/2)}{2}\sqrt{1 + 2x\frac{m_f}{i+1/2} + x^2}. \tag{3.5}$$

This is the celebrated Breit-Rabi-Formula [41] giving the magnetic field dependence of the energy of an atom in state $|s, i, f, m_f\rangle$ or $|s, i, m_s, m_i\rangle$, where the appropriate choice of quantum numbers depends on the strength of the magnetic field B applied. For the atoms of interest for this thesis, sodium and lithium with hyperfine constants $a_{\mathrm{hfs}}^{\mathrm{Na}} = 885.8130644\,\mathrm{MHz}$ and $a_{\mathrm{hfs}}^{\mathrm{Li}} = 152.1368407\,\mathrm{MHz}$, the Breit-Rabi-Diagrams are plotted in figure 3.1. Especially for the understanding of magnetic trapping, microwave (MW), radiofrequency (RF) transfers and Feshbach resonances a profound knowledge of those energy diagrams is essential. As it is obvious that each state $|m_s, m_i\rangle$ at high fields (Paschen-Back regime) adiabatically connects to a certain $|f, m_f\rangle$ at low fields (Zeeman regime), we will for the sake of simplicity in the following denote the states according to their low-field nomenclature.

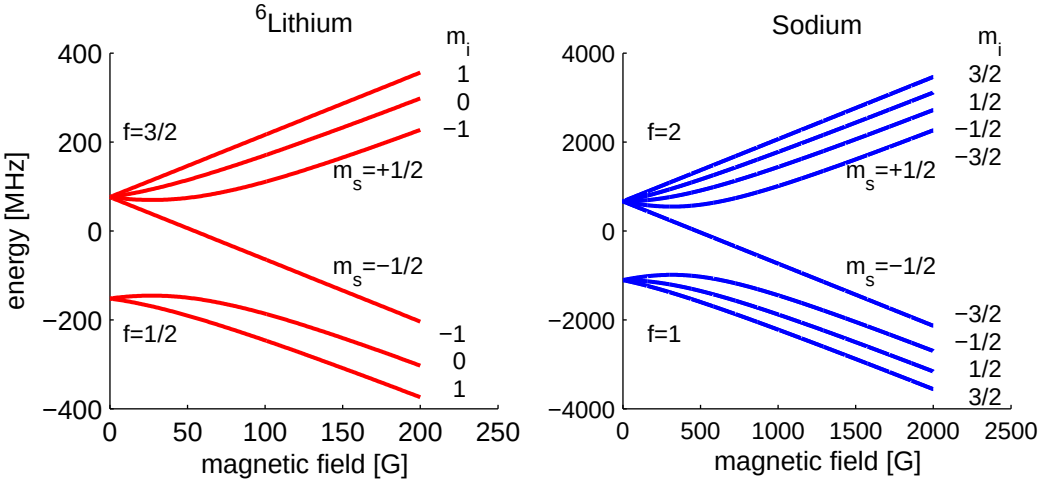

Figure 3.1.: *Breit-Rabi-diagrams of lithium and sodium according to eq.(3.5). At low fields (Zeeman regime), where $|f, m_f\rangle$ are good quantum numbers, the different hyperfine manifolds are split by $a_{\mathrm{hfs}}(i + 1/2)$, which is 228 MHz and 1.7 GHz for lithium and sodium, respectively. At high fields (Paschen-Back regime), $|m_s, m_i\rangle$ are the quantum numbers which characterize the atoms best: We see that the two main branches with slope $\pm 1.4\,\mathrm{MHz/G}$ are given by the electron spin orientation $m_s = \pm 1/2$ and the substructure reveals the different m_i states, which are offset by $a_{\mathrm{hfs}}/2$ from each other.*

3.2. Preparation of Different Spin Channels

3.2.1. Ultracold Atoms in the Optical Dipole Trap

As the preparation of an ultracold sodium-lithium mixture in an optical dipole trap (ODT) has already been described in detail elsewhere [38], we will in the following only shortly summarize the most important steps here and focus on the new items being of direct relevance for this thesis.

In the magnetic trap (MT), sodium and lithium are both trapped in their respective stretched states $\mathrm{Na}|2,2\rangle$ and $\mathrm{Li}|3/2,3/2\rangle$ as in this combination spin-changing collisions (see section 3.3.2) are not possible and thus sympathetic cooling works most efficiently [42, 43]. When the atoms are cold enough, both species are loaded into a crossed beam optical dipole trap (ODT), which has been realized in two different ways during the course of this thesis:

- For all measurements presented in our paper on sodium intraspecies Feshbach Resonances [26], we used optical fibers to guide the light to our experimental setup. Due to the limited power capability [44], we had to use high trapping frequencies of $\omega^{\mathrm{Na}}/2\pi = (310, 130, 310)\,\mathrm{Hz}$ to provide sufficient trap depth of $\sim 10\,\mu\mathrm{K}$ to hold the atoms.

- As our old ODT was both limited in trap depth due to power issues as well as in sodium atom number due to density-induced three-body losses (see section 3.4.2), we decided to change our setup and send the infrared beams forming the ODT potential free space to the experiment. The resulting trapping frequencies are $\omega^{\mathrm{Na}}/2\pi = (74, 78, 145)\,\mathrm{Hz}$ at similar trap depths as before, i. e. three-body losses are not limiting any more, resulting in $4 \cdot 10^6$ thermal Na atoms after loading from the MT into the ODT or an almost pure condensate of $1 \cdot 10^6$ atoms after an additional stage of evaporative cooling, respectively.

- Due to imperfections in the alignment of the ODT and a residual curvature in our magnetic field, we had to change the power balancing in the ODT beams for some of the resonances at high fields (see chapter 5 and appendix B), resulting in $\bar{\omega}^{\mathrm{Na}}/2\pi = 102\,\mathrm{Hz}$.

Throughout this thesis, the coordinate system will be oriented as follows: The x-axis points in the direction of the optical lattice (chapter 6), the external magnetic field is applied in y-direction and the camera takes pictures in the $x-y$ plane (for visualization, see figure 6.1). Gravity acts along the z-axis, thus our trap frequencies in this direction are chosen highest in order to counteract the gravitational sag and thus maximize the overlap between the two atomic clouds.

In both ODT configurations, the trapping frequencies for lithium are given by $\omega^{\mathrm{Li}} = 2.11\omega^{\mathrm{Na}}$, as can be easily seen by the formulas given in section 6.1.2, where optical dipole potentials are treated in detail. The oscillation measurements presented in figure 5.1 of section 5.2 confirm the theory: From the respective fits, we get $\omega_y^{\mathrm{Li}}/2\pi = (154.2 \pm 1.4)\,\mathrm{Hz}$ and $\omega_y^{\mathrm{Na}}/2\pi = (74.9 \pm 0.4)\,\mathrm{Hz}$, which yields a trapping frequency ratio of 2.06 ± 0.02. Considering

the large amplitude oscillation used for that measurement, which makes the atoms also probe the anharmonic regime of the trap, the agreement between theory and experiment is good.

3.2.2. Rapid Adiabatic Passage

Sodium atoms in the $|2,2\rangle$ state are not a good starting point for making a BEC as this state heavily suffers from three-body losses [45]. Thus we want to drive the transition $|2,2\rangle \rightarrow |1,1\rangle$, as the three-body loss coefficient L_3 of the final state is an order of magnitude lower than the one of the initial state (see measurements section 3.4.2). A robust way to achieve this transfer is using a rapid adiabatic passage (RAP) [46], which we will explain in the following.

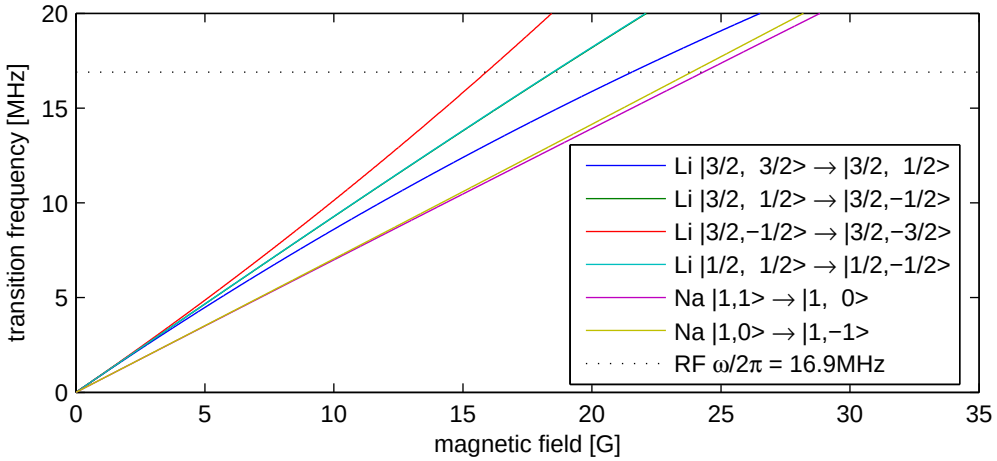

Figure 3.2.: *RF-transitions between different spin states in lithium and sodium as used in our experiment. The antenna resonance frequency ω is shown as dotted black line. Note that the transitions* $\mathrm{Li}\,|3/2,1/2\rangle \rightarrow \mathrm{Li}\,|3/2,-1/2\rangle$ *and* $\mathrm{Li}\,|1/2,1/2\rangle \rightarrow \mathrm{Li}\,|1/2,-1/2\rangle$ *almost lie exactly on top of each other and are not resolved in this graphical representation.*

In short, the RAP is based on the dressed states of a two-level system with resonance frequency ω_0 in an electric field oscillating with ω. The idea is to adiabatically keep the atom in the dressed state when sweeping the detuning $\Delta = \omega - \omega_0$ over resonance, thereby transfering the atom between the two bare states, which resemble the dressed states in the limit of large detuning. On resonance, where the detuning $\Delta = 0$, the Rabi frequency is denoted as Ω. If one sweeps the oscillation frequency[2] over the two-level system's resonance at a constant sweep rate such that $\Delta(t) = \alpha t$, according to the celebrated Landau-Zener formula [47] the probability P for a diabatic transition is

$$P = e^{-2\pi \frac{\Omega^2}{|\alpha|}}. \tag{3.6}$$

[2]Equivalently, one can also sweep the resonance frequency ω_0 instead of ω, which can be easily done e. g. by applying a small external magnetic field which shifts the levels and thus ω_0 due to the Zeeman effect.

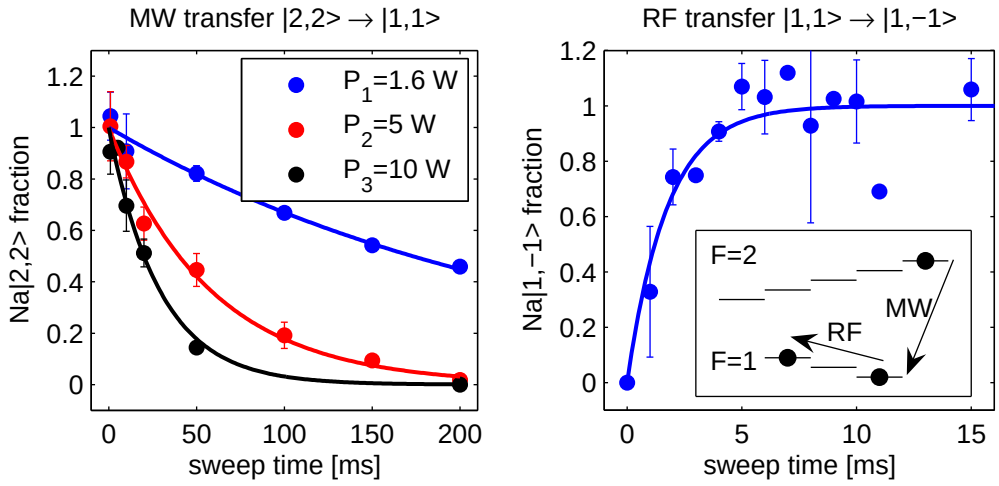

Figure 3.3.: *Landau-Zener sweeps of the sodium* $|2,2\rangle \rightarrow |1,1\rangle$ *and* $|1,1\rangle \rightarrow |1,-1\rangle$ *transitions, for three different MW power settings* P_i*. The experimental data are fitted using eq. (3.6), yielding the Rabi frequencies of* $\Omega_1/2\pi = (228 \pm 9)\,\mathrm{Hz}$*,* $\Omega_2/2\pi = (473 \pm 21)\,\mathrm{Hz}$*,* $\Omega_3/2\pi = (668 \pm 44)\,\mathrm{Hz}$ *for the MW- and* $\Omega_{\mathrm{RF}}/2\pi = (12.8 \pm 1.5)\,\mathrm{kHz}$ *for the RF-transition. The inset shows a schematic of the transfers between and within the different hyperfine manifolds.*

We see that $|\alpha| \ll \Omega^2$ must be fulfilled in order to make the passage *adiabatic*, i. e. a high Rabi frequency is advantageous. The word *rapid* refers to the passage not only being used in the case of RF- and MW-, but also optical transitions. There, the passage has to be done rapidly in comparison to the timescale given by spontaneous decay processes. For a more detailed description the reader may be referred to [48], where a comprehensive overview of RAPs using a Bloch Sphere picture is given.

Experimentally, the RAP on the $\mathrm{Na}\,|2,2\rangle \rightarrow \mathrm{Na}\,|1,1\rangle$ transition is realized by sweeping an offset magnetic field around 1 G at fixed MW frequency $\omega/2\pi = 1775.3\,\mathrm{MHz}$. Simultaneously, we do the transfer $\mathrm{Li}\,|3/2,3/2\rangle \rightarrow \mathrm{Li}\,|1/2,1/2\rangle$ by irradiating $\omega/2\pi \approx 231.6\,\mathrm{MHz}$, such that the resulting final state of the mixture does not suffer from spin-changing collisions. Note that this transfer has to take place *after* loading the atoms into the ODT, as the final states are high-field seekers and thus not magnetically trappable.

After some optional additional evaporative cooling in the ODT, we prepare the atoms in the spin channel we want to do the experiments, e. g. Feshbach spectroscopy, in. For this purpose, we built an antenna being impedance matched at 16.9 MHz.[3] Depending on the magnetic field sweep range, we can drive the transitions shown in figure 3.2.

Figure 3.3 shows the results of the MW- and RF-transfer of $\mathrm{Na}\,|2,2\rangle \rightarrow \mathrm{Na}\,|1,1\rangle$ and $\mathrm{Na}\,|1,1\rangle \rightarrow \mathrm{Na}\,|1,-1\rangle$, respectively. With the frequency sweep ranges of 511 kHz and

[3] This frequency is mostly determined by the geometric constraints for the antenna: It has been designed such that it does not diminuish the optical access when being placed near the atoms, i. e. on the glass cell.

11.21 MHz corresonding to the respective ramps in magnetic field, we get a Rabi frequency of $\Omega_{\mathrm{MW}}/2\pi = (668 \pm 44)\,\mathrm{Hz}$ and $\Omega_{\mathrm{RF}}/2\pi = (12.8 \pm 1.4)\,\mathrm{kHz}$, respectively.[4] It has to be stressed that in the current configuration the antenna, which is also being used for evaporation in the magnetic trap, is not impedance matched, which severely limits the Rabi frequency Ω_{MW}. Thus we can currently not exceed a Rabi frequency of $\Omega_{\mathrm{MW}} = 0.67\,\mathrm{kHz}$ on the $\mathrm{Na}\,|2,2\rangle \rightarrow \mathrm{Na}\,|1,1\rangle$ transition without major changes of the MW setup.

Recently, MW induced Feshbach resonances have been proposed for sodium [49]. Their width depends on the strength of the applied radiation and can be estimated as follows: With $\hbar\Omega \propto \Delta\mu B_{\mathrm{MW}}$, where $\Delta\mu$ is the magnetic moment of the transition and B_{MW} the magnetic field strength of the microwave radiation, we see that this strongly limits $B_{\mathrm{MW}} \lesssim 0.4\,\mathrm{mG}$. The corresponding width of the microwave induced Feshbach resonance is $\sim 1\,\mathrm{mHz}$ [49], which would require a magnetic field stability on the order of $\sim 0.5\,\mathrm{nG}$ for tuning, a value being experimentally not feasible. Thus, at least an impedance matching circuit and the resulting increase in Ω would be essential to observe MW induced Feshbach resonances.

3.2.3. Stern-Gerlach

Having applied the RAP on the atoms, we have to check whether the transfer has been succesful. For that purpose, we use a Stern-Gerlach type experiment: The common way to image our atoms is absorption imaging [27], usually after a time-of-flight (TOF) expansion in order to reduce the high optical densities. If we consider the expansion of a thermal cloud at temperature T, the $1/e^2$ radius of the cloud $\sigma(t_{\mathrm{TOF}})$ reads after a time t_{TOF} of TOF

$$\sigma^2(t_{TOF}) = \sigma^2(0) + \frac{k_B T}{m} t_{TOF}^2 \tag{3.7}$$

where m denotes the mass of the atoms and $\sigma(0)$ is the in-situ width of the trapped atomic cloud (for a derivation, see section 3.4.1). We see that the normal TOF expansion does not differ between different spin states. This changes if we apply a magnetic field gradient $B' = \partial B/\partial y$ during a time $t_{\mathrm{TOF}} - t_{\mathrm{D}}$ of the expansion. If we denote μ as the atoms' magnetic moment in their respective spin state, the shift of the cloud center reads

$$\Delta x = \frac{\mu B'}{2m}\left(t_{\mathrm{TOF}}^2 - t_{\mathrm{D}}^2\right). \tag{3.8}$$

We see that $\Delta x \propto t_{\mathrm{TOF}}^2$, while $\sigma \propto t_{\mathrm{TOF}}$, i. e. by choosing long TOFs we are able to seperate the different spin components. The external magnetic field is not applied during the whole expansion time t_{TOF}, but only during $t_{\mathrm{TOF}} - t_{\mathrm{D}}$, as the fintune coil used to create the gradient produces a magnetic field $B(y) = B_0 + B'y$ with $B_0 = 10.4\,\mathrm{G}$ and $B' = 3.9\,\mathrm{G/cm}$. Thus the offset field B_0 results in a transition shift for sodium of 27 MHz= 2.7Γ, where $\Gamma = 10\,\mathrm{MHz}$

[4] Note that the transition $\mathrm{Na}\,|1,1\rangle \rightarrow \mathrm{Na}\,|1,-1\rangle$ is a two-photon transition via the $\mathrm{Na}\,|1,0\rangle$ state, so the single transition Rabi frequency for $\mathrm{Na}\,|1,1\rangle \rightarrow \mathrm{Na}\,|1,0\rangle$ or $\mathrm{Na}\,|1,0\rangle \rightarrow \mathrm{Na}\,|1,-1\rangle$ is expected to be higher.

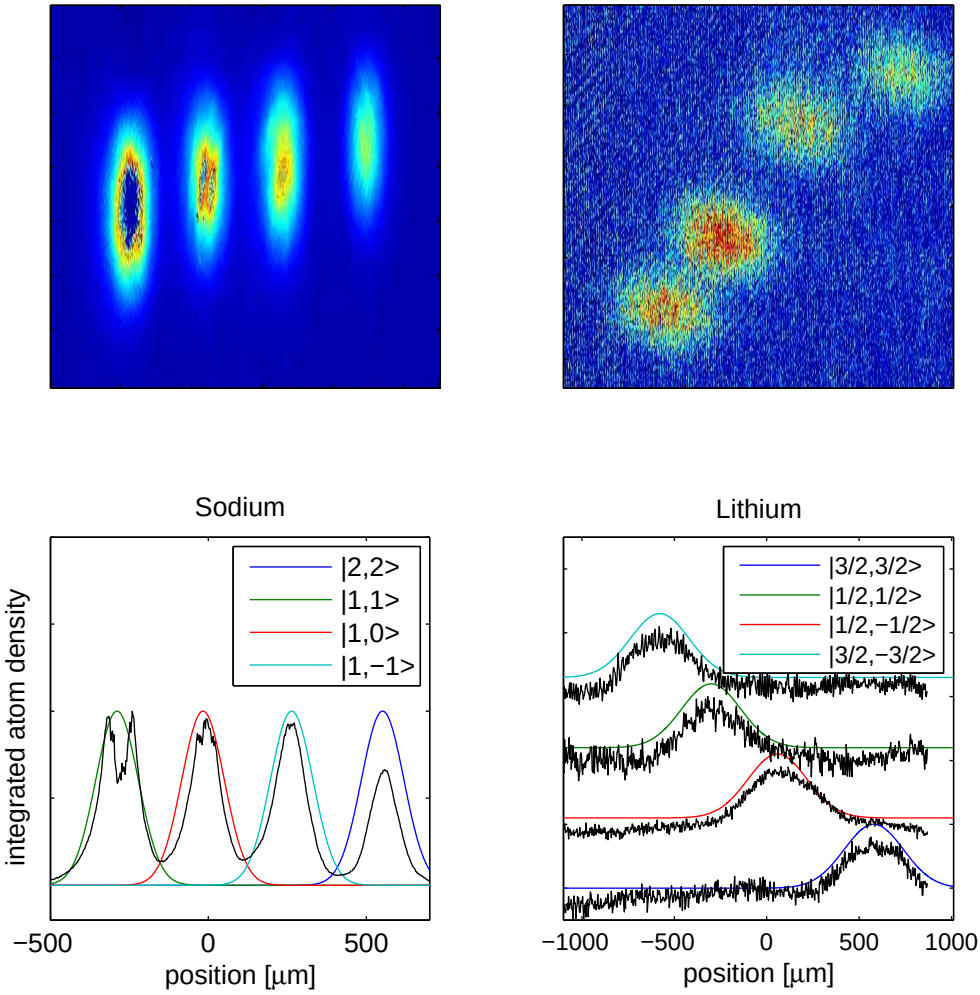

Figure 3.4.: *Stern-Gerlach expansion of sodium (left) and lithium (right), showing pictures of different experimental preparations superimposed. The respective spin states of the condensed sodium atoms are nicely seperated due to their low expansion energy, whereas the different lithium spin states overlap and are thus offset for reasons of clarity. The calculated profiles have been obtained using eqs. (3.7) and (3.8) with* $t_{\mathrm{TOF}}^{\mathrm{Na}} = 11\,\mathrm{ms}$, $t_{\mathrm{TOF}}^{\mathrm{Li}} = 6\,\mathrm{ms}$, $T_{\mathrm{Li}} = 500\,\mathrm{nK}$ *and* $T_{\mathrm{Na}} = 100\,\mathrm{nK}$, *latter chosen to yield a good guide to the eye. Due to the short time-of-flight, the sodium clouds of the* $F = 1$ *hyperfine manifold are optically dense.*

is the linewidth of the transition used for imaging. Thus, if we would not turn off the finetune coil before imaging, the sodium atoms would scatter about a factor of thirty less imaging light than at vanishing magnetic field $B = 0$. Experimentally we choose a delay time of $t_{\mathrm{D}} = 2\,\mathrm{ms}$ to ensure all fields to have reached a sufficiently low value, which yields the displacements given in table 3.1 by means of eq. (3.8).

Na spin state	$\|2,2\rangle$	$\|1,1\rangle$	$\|1,0\rangle$	$\|1,-1\rangle$
theor. displ. $\Delta x[\mu\mathrm{m}]$	551	-289	-17	264
exp. displ. $\Delta x[\mu\mathrm{m}]$	603(4)	-341(6)	-33(3)	270(2)

Li spin state	$\|3/2,3/2\rangle$	$\|1/2,1/2\rangle$	$\|1/2,-1/2\rangle$	$\|3/2,-3/2\rangle$
theor. displ. $\Delta x[\mu\mathrm{m}]$	579	-300	58	-579
exp. displ. $\Delta x[\mu\mathrm{m}]$	530(10)	-280(12)	64(10)	-553(3)

Table 3.1.: *Theoretically calculated and measured displacements of different spin states after Stern-Gerlach separation. The TOF-durations chosen are* $t_{\mathrm{TOF}}^{\mathrm{Na}} = 11\,\mathrm{ms}$ *and* $t_{\mathrm{TOF}}^{\mathrm{Li}} = 6\,\mathrm{ms}$. *The values were obtained without using any free parameters. Considering the high sensitivity on the order of about* $100\,\mu\mathrm{m/ms}$ *on the TOF-duration* t_{TOF} *and especially on the delay time* t_{D}, *the agreement of theory and experiment is good.*

In order to visualize the effect of the Stern Gerlach-expansion, in figure 3.4 we show absorption images of sodium and lithium in different spin states. The preparation of the condensed sodium atoms can be checked by eye, whereas determining quality of the lithium preparation requires a fit to the data.

3.3. Loss Mechanisms in Trapped Ultracold Atom Samples

Having prepared a atoms in a certain spin state, one can map out a loss curve of the sample to determine its lifetime, e. g. in dependence of an external magnetic field applied. In the following, we will explain which useful information about the scattering length can be concluded from such measurements.

3.3.1. One-Body Losses

Loss processes, which only involve a single trapped atom, are called one-body losses. There are mainly two mechanisms leading to such a process: As the vacuum of an experimental apparatus is never perfect, there is always the probability that an atom at room temperature scatters with a trapped cold atom, which makes latter immediately leave the trap.[5]

Another process which can lead to the loss of atoms are uncontrolled changes in the trap frequency: If the trapping potential features noise at multiples of the trap frequency, this can cause excitations of the atom to a higher harmonic oscillator state, which finally results in loss. As we will show in detail in chapter 8, using this kind of excitation process can also be used in a controlled way to study relaxation of the resulting excited state.

[5]This is actually how vacuum problems in our experimental setup show up: We observe strongly reduced atom lifetimes if e. g. the atomic beam shutter is broken and thus the hot atom beam scatters with the trapped atoms.

Typically, the atoms in the MT feature a lifetime of $\sim 30\,\mathrm{s}$ and in the ODT $\sim 30\,\mathrm{s}$ as well. Together with a calculated photon scattering rate of $\Gamma_{\mathrm{sc}} \sim 0.01\,1/\mathrm{s}$ from the IR-beams, this sets an upper bound of $\Gamma_{\mathrm{bg}} < 0.03\,1/\mathrm{s}$ on the one-body loss rate induced by collisions with the background gas.

3.3.2. Two-Body Losses

Spin-Exchange Processes

The interaction potential of two alkali atoms $U(r)$ can to a good approximation be assumed to be spherically symmetric. During the collision, the two valence electrons of the colliding atoms can either be in a singlet $S = 0$ or triplet $S = 1$ state. As explained in chapter 2, the associated potentials $U_t(r)$ and $U_s(r)$ are similar for large, while differing substantially for small interatomic distances. Thus, we can write the interaction potential as

$$U = U_s P_s + U_t P_t = \frac{U_s + 3U_t}{4} + (U_s - U_t)\vec{s_1} \cdot \vec{s_2} \tag{3.9}$$

with P_s and P_t being the singlet and triplet projection operators, respectively. Writing

$$\vec{s_1} \cdot \vec{s_2} = s_{1,z} \cdot s_{2,z} + \frac{1}{2}(s_{1,+} \cdot s_{2,-} + s_{1,-} \cdot s_{2,+}) \tag{3.10}$$

we see that the interaction described by eq. (3.9) conserves the total spin S and its z-component M_S, but can exchange the spin of the atoms by flipping one from up to down and the other vice versa. Therefore, this interaction is also called *spin-exchange interaction*.

In the following, we want to investigate the characteristics of the spin-exchange interaction on the example of a sodium-lithium mixture. The most trivial case is the one of a mixture of atoms in their respective stretched states, i. e. $\mathrm{Na}|2, \pm 2\rangle + \mathrm{Li}|3/2, \pm 3/2\rangle$. Here, there are simply no states for an electron spin exchange available, or more mathematically speaking, the atoms are in a pure triplet state, so these mixtures are stable against spin exchange.

For other spin mixtures, as already shown in the derivation of the Breit-Rabi-Formula, we can decompose the atoms' state as

$$|f, m_f\rangle = \alpha\,|m_s = 1/2, m_i = m_f - 1/2\rangle + \beta\,|m_s = -1/2, m_i = m_f + 1/2\rangle\,, \tag{3.11}$$

where i and s, which are fixed for a given atom, have been omitted in this notation for simplicity. If no external field B is applied, α and β are simply given by the well-known Clebsch-Gordan coefficients, and in the case of high magnetic fields we end up in a state where electron and nuclear spin are completely decoupled, i. e. either $\alpha = 1$ or $\beta = 1$, depending on the state (see figure 3.1). In the intermediate regime, one can get α and β by diagonalizing the Breit-Rabi Hamiltonian matrix and thus determining its eigenvectors.

In figure 3.5, we plot the energy of some selected spin mixtures with different $M_F = m_f^{\mathrm{Na}} + m_f^{\mathrm{Li}}$. As already pointed out, the spin exchange interaction can not change M_F, which strongly limits the transitions allowed between different spin states.

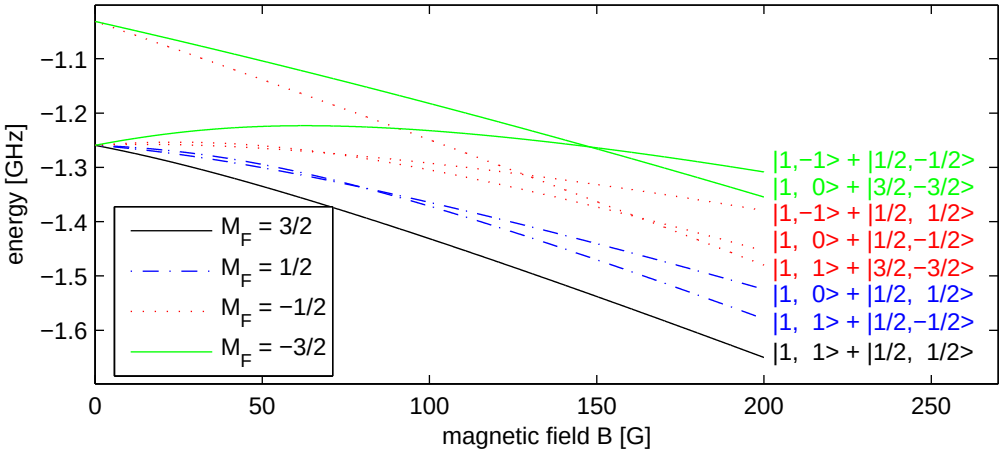

Figure 3.5.: *Energies of spin state combinations with different M_F. Spin exchange transitions are only possible within states of the same M_F manifold.*

In terms of losses, the $\mathrm{Na}|1,1\rangle + \mathrm{Li}|1/2,1/2\rangle$ state is obviously the best choice, as it does not cross with any other state having $M_F = 3/2$ and is additionally the energetically lowest of all.

More interesting is the $M_F = 1/2$ state decomposed analog to eq. (3.11)

$$\begin{aligned} |i\rangle \equiv |1,1\rangle_{\mathrm{Na}} + |1/2,-1/2\rangle_{\mathrm{Li}} = \alpha_i^{\mathrm{Na}} |1/2,1/2\rangle_{\mathrm{Na}} + \beta_i^{\mathrm{Na}} |-1/2,3/2\rangle_{\mathrm{Na}} \\ + \alpha_i^{\mathrm{Li}} |1/2,-1\rangle_{\mathrm{Li}} + \beta_i^{\mathrm{Li}} |-1/2,0\rangle_{\mathrm{Li}} \end{aligned} \tag{3.12}$$

From figure 3.5 we can see that there exists a state with equal $M_F = 1/2$ but being composed as

$$\begin{aligned} |f\rangle \equiv |1,0\rangle_{\mathrm{Na}} + |1/2,1/2\rangle_{\mathrm{Li}} = \alpha_f^{\mathrm{Na}} |1/2,-1/2\rangle_{\mathrm{Na}} + \beta_f^{\mathrm{Na}} |-1/2,1/2\rangle_{\mathrm{Na}} \\ + \alpha_f^{\mathrm{Li}} |1/2,0\rangle_{\mathrm{Li}} + \beta_f^{\mathrm{Li}} |-1/2,1\rangle_{\mathrm{Li}} \,. \end{aligned} \tag{3.13}$$

We see that the two states are connected via $\vec{s}_{\mathrm{Na}} \cdot \vec{s}_{\mathrm{Li}}$ yielding

$$\langle f | \vec{s}_{\mathrm{Na}} \cdot \vec{s}_{\mathrm{Li}} | i \rangle = \frac{1}{2} \beta_f^{*\mathrm{Na}} \alpha_f^{*\mathrm{Li}} \alpha_i^{\mathrm{Na}} \beta_i^{\mathrm{Li}} \equiv \eta_{\mathrm{spin}} \tag{3.14}$$

Of course transitions from $|i\rangle$ to $|f\rangle$ can only take place if they are energetically allowed, i. e. in the magnetic field range up to $B = 80\,\mathrm{G}$. In the following, we will derive a quantitative formula of the associated transition rate.

Motivated[6] by the derivation of eq. (2.22) in chapter 2, we replace $U_s - U_t$ in eq. (3.9) by $2\pi\hbar^2(a_s - a_t)/\mu$, where a_s and a_t refer to the scattering lengths for singlet and triplet

[6]This is of course not a strict derivation. The interested reader may find the rigorous proof in [50], yielding the same result.

potential, respectively. Recalling Fermis golden rule

$$P_{i\to f} = \frac{2\pi}{\hbar} \left|\langle f|U|i\rangle\right|^2 \rho \tag{3.15}$$

giving the transition rate from an initial state i to the final state f when interacting via a potential U, we get by noting that the density of states for free particles[7] reads $\rho = \frac{\mu}{2\pi^2\hbar^3}\sqrt{2\mu E}$ with E being the energy difference between initial and final state

$$P_{i\to f} = 4\pi\sqrt{2E/\mu}(a_s - a_t)^2 \left|\eta_{spin}\right|^2 . \tag{3.16}$$

For typical parameters of cold atom experiments, we can estimate $P_{i\to f} \sim 10^{-12}\mathrm{cm}^3/\mathrm{s}$. Due to the high energy gain in a spin-exchange collision $E \sim \mathcal{O}(\mathrm{MHz})$, which can be seen in figure 3.5 as the vertical distance between two lines of equal M_F, both participating atoms will be lost from the trap. Therefore, we can relate the spin exchange rate $P_{i\to f}$ to experimentally observable trap loss

$$\dot{n}_{\mathrm{Li}} = \dot{n}_{\mathrm{Na}} = P_{i\to f} n_{\mathrm{Li}} n_{\mathrm{Na}} \tag{3.17}$$

with n_{Li} and n_{Na} being the densities of lithium and sodium, respectively. We see that the measurement of spin-exchange losses should reveal information about the scattering lengths' difference, as we will further investigate quantitatively by means of experimental data below.

Dipolar Processes

The assumption of the electrons interacting only via a spherically symmetric potential $U(r)$ is not completely correct. As we will see later in chapter 4, the magnetic dipole-dipole interaction U_{dd} between the electron's spins can despite of its small energy be of crucial importance for understanding the experimental observations. The associated potential can be written as [50]

$$U_{\mathrm{dd}} = \frac{\mu_0(2\mu_B)^2}{4\pi r^3}\left[\vec{s}_1\cdot\vec{s}_2 - 3(\vec{s}_1\cdot\vec{r})(\vec{s}_2\cdot\vec{r})\right] , \tag{3.18}$$

where $\vec{r}$ denotes the spatial vector between the two electrons. We can see from an expansion in spherical harmonics [51] that this interaction drives transitions with $\Delta l = \pm 2, 0$ (except $l = 0 \to l = 0$), taking the required angular momentum from the spins such that $M_S + m_l = m_s^{\mathrm{Na}} + m_s^{\mathrm{Li}} + m_l$, is conserved[8].

In order to estimate the importance of the dipole interactions for two-body losses, we want to compare it to the previously considered spin-exchange collisions. Normalizing eq. (3.18)

[7] Although experimentally the atoms are placed in a trap, after a spin exchange collision they will have gained so much energy $E \gg U_{\mathrm{trap}}$ that they can be treated as free particles.

[8] Including also the nuclear spin in the treatment, one can more generally say that $M_I + M_S + m_l$ is conserved. Compared to the dipole-dipole interaction of the spins, the one of the nuclei is by a factor of μ_i/μ_s smaller and thus negligible.

for a finite volume and comparing it with eq. (3.9), where we again replace the potentials by the appropriate scattering lengths, we get

$$\frac{U_{\mathrm{dd}}}{U_{\mathrm{ex}}} \approx \frac{\mu_0 \mu_B^2 \mu}{\hbar^2 (a_s - a_t)}. \tag{3.19}$$

For this rough estimate, we neglected constants and the spin dependencies, which yield factors on the order of 1. With typical scattering lengths on the order of several $10a_0$, we get as an estimate for $U_{dd}/U_{ex} \sim 10^{-2}$, or for the associated transition rate $P^{dd}_{i\to f} \approx 10^{-4} P^{ex}_{i\to f}$ $\sim 10^{-16}\,\mathrm{cm}^3/\mathrm{s}$. We thus see that being in a spin channel where spin-exchange takes place, we do not need to take losses due to the dipole interaction into account; these might only be of interest e. g. in the stretched states, where spin exchange is not possible.

3.3.3. Three-Body Losses

Another very important loss mechanism in ultracold atom samples are the three-body-losses, e. g. they make the transfer $\mathrm{Na}|2,2\rangle \to \mathrm{Na}|1,1\rangle$ necessary as already pointed out in section 3.2. In the energetically lowest spin state $\mathrm{Na}|1,1\rangle\mathrm{Li}|1/2,1/2\rangle$, which does not suffer from two-body losses, loss mechanisms involving more than one atom are described by three-body processes. To be able to understand them better, we will explain the underlying mechanisms in the following.

When two alkali atoms collide, they interact via a combination of singlet and triplet potential, each of which gives rise to bound molecular states. Therefore, with a finite probability the two atoms can be scattered into one of those bound states, thereby gaining the associated binding energy $|\varepsilon_b|$. For forming a molecule, two atoms do not have enough degrees of freedom to fulfil momentum and energy conservation (which is trivially fulfilled in the two-body processes described above in section 3.3.2). Thus they need a third atom which carries away a certain fraction of the bound state energy $\eta|\varepsilon_b|$ in form of kinetic energy. To further proceed, we have to distinguish two cases:

1. Away from any resonance, the binding energy ε_b is way larger than the typical trap depth of $U_0 = \mathcal{O}(10\mu\mathrm{K})$. Thus, all three involved atoms are immediately lost from the trap.

2. Near a resonance, for the sake of simplicity we assume the universal formula for the bound state energy eq. (2.13) $\varepsilon_b = -\frac{\hbar^2}{2\mu a^2}$ to be valid.[9] The typical trap can hold the atom and the molecule for scattering lengths a on the order of $500a_0$ and more, as only then the resulting dimer is so weakly bound that the energy release is small enough. But as this molecule is in a vibrationally highly excited state, the next collision with an atom will result in a relaxation to lower lying states and thus again, three atoms

[9] In section 3.3.4 we will see to what extent this assumption is justified for different types of resonances.

will be lost from the trap, but in contrast to the first case one atom having gained the recombination energy $-\eta\varepsilon_b$ will stay trapped and thus effectively heat the sample.

So we see that in both scenarios three atoms will be lost from the trap. Moreover, besides the recombination heat, inherent to the three- and two-body loss processes there is the socalled anti-evaporation: As the losses in an atom sample of density n scale as $\dot{n} = -L_m n^m$ with m being 2 for the two- and 3 for the three-body loss, atoms are preferably lost in the middle of the trap, where the density is biggest. The atoms there have an energy lower than the sample average and thus the process is just the contrary of evaporative cooling: There we spill the most energetic atoms, while two- and three-body losses remove the coldest atoms and thus effectively heat the sample.

A dimensional analysis shows that the three-body loss coefficient L_3 scales near a Feshbach resonance as a^4 [52], which is fundamental for doing Feshbach spectroscopy: Experimentally, we are sensitive to the enhanced losses and identify the position of maximum loss as the resonance position.[10]

3.3.4. Broad and Narrow Resonances

In our simplified treatment, we have so far considered the effects of two-body interactions, which are elastic scattering and losses, as independent processes. As to be read in detail in [5], one can incorporate the two-body losses into the imaginary part of the scattering length a, which then reads

$$a = a_{\mathrm{bg}} \left(1 + \frac{\Delta\delta\mu}{-E_0 + i(\gamma/2)} \right) \tag{3.20}$$

where E_0 is the threshold resonance position, most commonly tuned by a magnetic field, $\delta\mu$ is the difference in magnetic moments of open and closed channel and γ the decay rate for the bound state into all available loss channels. In figure 3.6, eq. (3.20) is visualized: The difference of loss maxima between two-and three-body losses are an interesting feature, which we will revisit in chapter 5. The plot of imaginary vs. real part of a shows the advantage of using 'broad' resonances, i. e. experimentally speaking such with a large width Δ.[11] Noting that the functional form shown here is a circle with center $(x, y) = (a_{\mathrm{bg}}, a_{\mathrm{bg}}\Delta\delta\mu/\gamma)$ and radius $a_{\mathrm{bg}}\Delta\delta\mu/\gamma$, we see that not only for large widths Δ, but also for large background scattering lengths a_{bg}, the tuneability of a at the same loss rate b is higher.

Motivated by the discussion about the tuneability, one can define the resonance strength parameter

$$s_{\mathrm{res}} = \frac{a_{\mathrm{bg}}}{R_{\mathrm{vdW}}} \frac{\delta\mu\Delta}{E_{\mathrm{vdW}}}, \tag{3.21}$$

[10] Of course, physics is not that easy, but a detailed treatment of three-body losses being a field of ultracold atom research on its own [53] is far beyond the scope of this thesis.

[11] A more rigorous definition of the term 'broad' will be given at the end of this chapter.

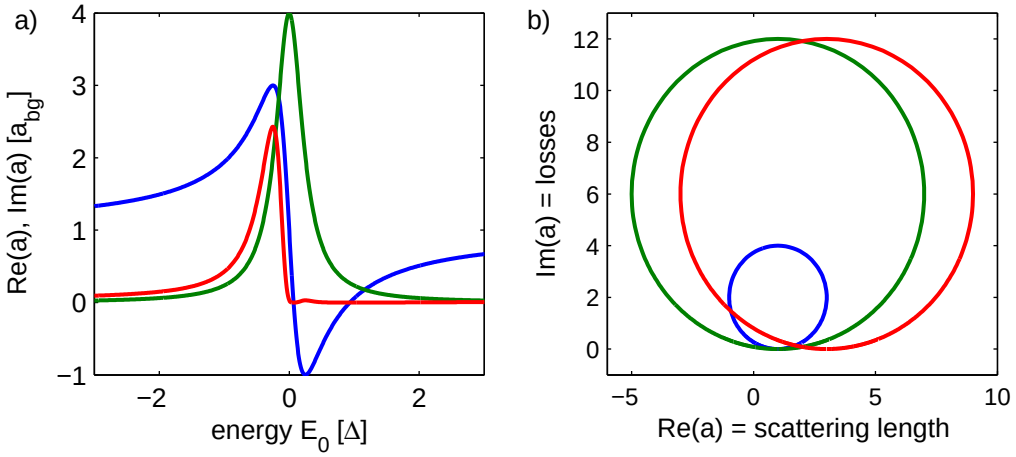

Figure 3.6.: ***a)*** *Real (blue) and imaginary (green) part of the scattering length a according to eq. (3.20). The parameters chosen are* $(a_{\mathrm{bg}}, \Delta\delta\mu, \gamma) = (1, 1, 0.5)$. *Shown in red is the scaling of the three-body losses* $\propto a^4$. ***b)*** *Tuning of the losses* $\propto \mathrm{Im(a)}$ *with the real part of the scattering length* Re(a). *Shown are the curves with* $(a_{\mathrm{bg}}, \Delta\delta\mu, \gamma)$ *= (1,1,0.5) (blue), (1,3,0.5) (green) and (3,1,0.5) (red). One sees that for a given loss* Im(a), *resonances with larger* Δ *and* a_{bg} *are advantageous for tuning.*

where R_{vdW} and $E_{\mathrm{vdW}} = \hbar^2/(2\mu R_{\mathrm{vdW}}^2)$ are the van der Waals radius and energy, respectively. If $s_{\mathrm{res}} \gg 1$, we call the resonance *broad*. Intuitively, one can see that in this case the microscopic details of the potential do not matter, as the defining length and energy scales are given by a_{bg} and $\delta\mu\Delta$, respectively. Molecules being formed in the range of $\pm\Delta$ around such a resonance have a very small closed channel admixture in their wavefunction [5] and thus their binding energy can be described by the universal expression eq. (2.13) having the scattering length a as only parameter. In contrast, narrow resonances show universal physics only around a very small fraction of their (already narrow) width Δ, but nevertheless they have recently found an application in the experimental investigation of the Fermi Polaron [18].

3.4. Interpretation of Loss Curves

In the following, we will extract information from experimentally recorded loss curves, starting from a short overview about atom density distributions in traps.

3.4.1. Atom Density Distributions in Traps

In order to quantitatively understand loss processes occuring in ultracold atom systems, we have to analyze their density distributions. For N distinguishable particles with mass m at temperature T in a trap with frequency ω, the Maxwell-Boltzmann distribution reads

$$n(\vec{x},\vec{p}) = N\mathcal{N}_x \exp\left(-\frac{m\omega^2\vec{x}^{\,2}}{2k_BT}\right)\mathcal{N}_p \exp\left(-\frac{\vec{p}^{\,2}}{2mk_BT}\right). \tag{3.22}$$

The normalization factors read $\mathcal{N}_x = (\frac{m\omega^2}{2\pi k_BT})^{3/2}$ and $\mathcal{N}_p = (\frac{1}{2m\pi k_BT})^{3/2}$. Integrating out the momentum part, we are left with the in-situ density distribution, which we can obtain via absorption imaging [27]. For thermal atoms at a temperature of $T = 1\,\mu$K in our optical dipole trap with frequencies[12] $(\omega_x^{\mathrm{Na}}, \omega_y^{\mathrm{Na}}, \omega_z^{\mathrm{Na}})/2\pi = (74, 78, 145)\,$Hz and $(\omega_x^{\mathrm{Li}}, \omega_y^{\mathrm{Li}}, \omega_z^{\mathrm{Li}})/2\pi = (157, 154, 305)\,$Hz, the in-situ widths of the profiles are $(\sigma_{0,x}^{\mathrm{Na}}, \sigma_{0,y}^{\mathrm{Na}}) = (41, 39)\,\mu$m and $(\sigma_{0,x}^{\mathrm{Li}}, \sigma_{0,y}^{\mathrm{Li}}) = (38, 38)\,\mu$m. As this result is very sensitive on the precise knowledge of the trap frequencies and an easy determination of σ is complicated by the high optical density of the trapped clouds, it is more senseful to image the atom distribution a time t_{TOF} after the turn-off of the confining potential. The new distribution then reads

$$\begin{aligned} n(\vec{x}) &= \int \mathrm{d}^3r_0\mathrm{d}^3p_0 n(\vec{r}_0,\vec{p}_0)\delta^3(\vec{r}_0 + \vec{p}_0 t_{\mathrm{TOF}} - \vec{x}) \\ &= N\mathcal{N}_x(t_{\mathrm{TOF}}) \exp\left(-\frac{\vec{x}^{\,2}}{2\sigma^2(t_{TOF})}\right) \end{aligned} \tag{3.23}$$

with

$$\sigma^2(t_{\mathrm{TOF}}) = \frac{k_BT}{m\omega^2} + \frac{t_{\mathrm{TOF}}^2 k_BT}{m} = \sigma^2(0)(1+\omega^2 t_{\mathrm{TOF}}^2). \tag{3.24}$$

and the new normalization $\mathcal{N}_x(t_{\mathrm{TOF}}) = 1/(2\pi\sigma(t_{\mathrm{TOF}}))^{3/2}$. From eq. (3.24) we see the advantage of time-of flight compared to in-situ images: To deduce temperature, the in-situ measurement requires precise knowledge of the trapping frequency ω. Moreover, high optical densities and trap anharmonicities can be problematic for the in-situ image analysis. In contrast, as long as $t_{\mathrm{TOF}} \gg 1/\omega$, the TOF-picture only requires precise knowledge of the experimentally well determined t_{TOF} to deduce the temperature T.

So far, our treatment has only considered classical particles, but when dealing with ultracold quantum gases, naturally also the statistics come into play. Weakly interacting bosons at low temperatures can be described by the famous Gross-Pitaevskii equation [54, 55], which is basically a Schrödinger equation with the nonlinear term eq. (2.22) motivated in section 2 and reads

$$-\frac{\hbar^2}{2m}\nabla^2\psi(r) + V(r)\psi(r) + U_0|\psi(r)|^2\psi(r) = \mu\psi(r). \tag{3.25}$$

Here, $V(r)$ denotes the external confining potential, $U_0 = 4\pi\hbar^2 a/m$ the interaction energy and $\mu = \partial E/\partial N$ the chemical potential. The wavefunction $\psi(r)$ is normalized such that $\int \mathrm{d}^3\mathrm{r}|\psi(\mathrm{r})|^2 = \mathrm{N}$ with N being the total number of condensed atoms. The exact solution of the Gross-Pitaevskii equation (GPE) requires numerics, but in the experimentally often

[12] In the course of this thesis, these values have not been constant, but adapted to the respective experimental requirements. The value given here has been used to obtain the optical lattice data presented in chapter 8.

relevant case of a kinetic energy being small in comparison to potential and interaction energy, we obtain the density of trapped atoms as

$$n(r) = |\psi(r)|^2 = \max\left(\frac{\mu - V(r)}{U_0}, 0\right). \tag{3.26}$$

In this socalled Thomas-Fermi approximation, the radii R_i of the cloud in a harmonic confining potential $V(r) = m\omega_i^2 x_i^2/2$ read

$$R_i = \sqrt{\frac{2\mu}{m\omega_i^2}}\,. \tag{3.27}$$

To express the density distribution in terms of experimentally accessible parameters, we take into account the normalization condition $\int \mathrm{d}V\, n(r) = N$ and thus get for the chemical potential

$$\mu = \frac{15^{2/5}}{2}\left(\frac{Na}{\bar{a}}\right)^{2/5}\hbar\bar{\omega}\,, \tag{3.28}$$

where we introduced the mean trap frequency $\bar{\omega} = \sqrt[3]{\omega_x\omega_y\omega_z}$ and the associated harmonic oscillator length $\bar{a} = \sqrt{\hbar/(m\bar{\omega})}$. Equation (3.28) shows some important characteristics of the trapped interacting Bose gas: In comparison to the density distribution of a classical gas (3.22) we see that its peak density does not simply scale with N, but with $N^{2/5}$, i. e. it is only weakly dependent on the atom number, a dependency which will be important later when investigating loss processes. The parameter $Na/\bar{a}$ is a measure of the ratio of interaction and kinetic energy and can thus be used to check the overall validity of the Thomas-Fermi approximation. At the surface of the condensed cloud, the Thomas-Fermi approximation is not giving a correct description (see figure 3.7), as due to the low density the kinetic energy term gains importance and thus one can not neglect it any more. The whole Gross-Pitaevskii equation (3.25) loses its validity in the regime of strong interactions, where a mean field description of the atoms' wavefunction is not justified any more.

In a time-of-flight picture, the Bose condensate simply rescales its charateristic shape of the inverted parabola (3.26), which has in the first experiments been used as a signature for a macroscopic occupation of the ground state [1]. While the exact mathematical description of the BEC expansion process is rather complex [56], for analyzing a TOF-picture of a partly condensed Bose gas we simply fit it with a bimodal distribution, i. e. a Maxwell-Boltzmann distribution (3.23) with a superimposed inverted parabola. The width of the gaussian gives us the temperature T and by integrating over the two distributions, we can also determine the condensate fraction η. Knowing the critical temperature for the BEC transition in a harmonic trap [50],

$$k_B T_c = 0.94\hbar\bar{\omega}N^{1/3} \tag{3.29}$$

we get via the relation for a harmonically trapped bose gas

$$\eta = \frac{N_c}{N} = 1 - \left(\frac{T}{T_c}\right)^3 \tag{3.30}$$

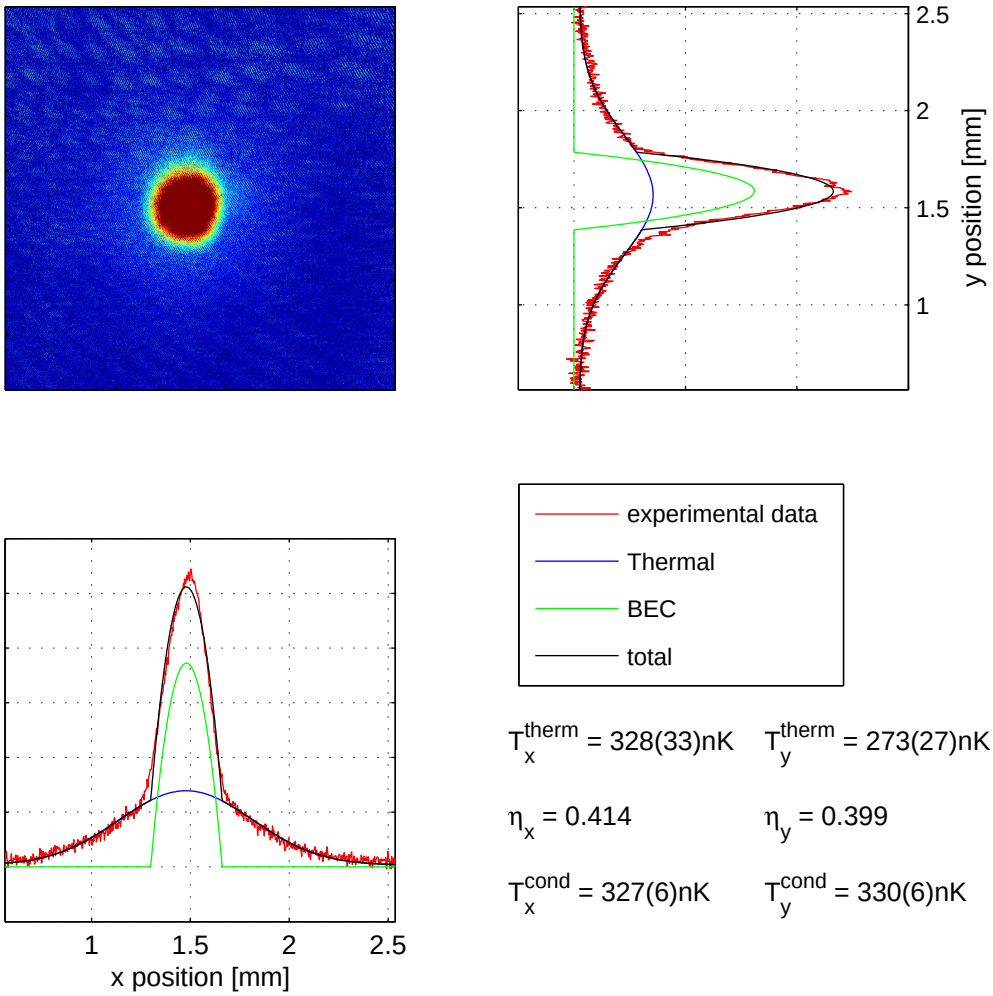

Figure 3.7.: *Time-of flight picture of a partly condensed Bose gas. The temperature can be either determined from the size of the thermal cloud ($T_{x,y}^{\mathrm{therm}}$) or from the condensate fraction ($T_{x,y}^{\mathrm{cond}}$). The results for the two different axes agree within their error bars, as expected for a thermalized gas. An interesting feature of the fit is the edge of the BEC, where the fit (black line) and the experimental data (red) disagree due to the Thomas-Fermi approximation losing its validity there.*

a complementary measure of the temperature.

In figure 3.7, we see a typical picture of a partly bose-condensed cloud after a time of flight of $t_{\mathrm{TOF}} = 31\,\mathrm{ms}$. With the fitting procedure described above, we get a condensate fraction of 40.6(1.5)% (as error, we take the difference between the results of x- and y-axis). Knowing the trap frequencies and the total atom number, we can derive the temperature using eqs. (3.29, 3.30) and get $T_x^{\mathrm{cond}} = 327(6)\mathrm{nK}$ and $T_y^{\mathrm{cond}} = 330(6)\mathrm{nK}$, where the error is mainly given by the uncertainties in the trap frequencies. A different method to get the

temperature is to extract it from the size of the thermal cloud using eq. (3.24), which in our case results in $T_x^{\mathrm{therm}} = 328(33)\mathrm{nK}$ and $T_y^{\mathrm{therm}} = 273(27)\mathrm{nK}$. The big errors can be explained by considering the quadratic dependence of T on σ, which itself has a fit uncertainty of typically 3%. Moreover, the magnification of our imaging system is not known to an accuracy of better than 4%, which in combination makes this temperature determination less precise than the method making use of the intrinsic BEC properties. But e. g. for small condensate fraction, temperature determination via the size of the thermal cloud is advantageous.

3.4.2. Loss Analysis of Trapped Homonuclear Atom Samples

The kind of losses most easy to understand and analyze are one-body losses obeying the equation $\dot{n} = -\gamma n$, which can be easily solved by $N(t) = N_0 \exp(-\gamma t)$, with $N(t)$ and N_0 being the total particle number after time t and at $t = 0$, respectively. This solution is independent of the distribution $n(r)$ of the trapped atoms.

For loss processes involving more than one trapped atom, deriving the loss equation is not as straightforward. In general, m-body losses obey $\dot{n} = -L_m n^m$ for thermal and $\dot{n} = -L_m n^m/m!$ for condensed bosonic atoms, where the factor $m!$ stems from the indistinguishability of particles in the BEC. As we usually measure the total particle number $N = \int \mathrm{d}V\, n(r)$, we first have to integrate the whole differential equation in space, yielding in the case of $\dot{T} = 0$

$$\dot{N} = -\alpha N^{\lambda+1} \tag{3.31}$$

which can be solved by

$$N(t) = \frac{N_0}{\left(1 + \alpha\lambda N_0^{\lambda} t\right)^{1/\lambda}}\,. \tag{3.32}$$

process	thermal cloud	BEC
2-body	$N(t) = \frac{N_0}{1+B_2 N_0 t}$ $B_2 = L_2 \left(\frac{m\omega^2}{4\pi k_B T}\right)^{3/2}$	$N(t) = \frac{N_0}{(1+\frac{2}{5}A_2 N_0^{2/5} t)^{5/2}}$ $A_2 = L_2 \frac{1}{420\pi^2 a^2 a_{ho}} \left(\frac{15a}{a_{ho}}\right)^{7/5}$
3-body	$N(t) = \frac{N_0}{(1+(\zeta+2)B_3 N_0^2 t)^{1/(\zeta+2)}}$ $B_3 = L_3 \left(\frac{m\omega^2}{2\sqrt{3}\pi k_B T_0}\right)^3$	$N(t) = \frac{N_0}{(1+\frac{4}{5}A_3 N_0^{4/5} t)^{5/4}}$ $A_3 = L_3 \frac{1}{15120\pi^2 (a a_{ho})^3} \left(\frac{15a}{a_{ho}}\right)^{9/5}$

Table 3.2.: *Scaling of different loss processes in homonuclear systems of thermal and condensed atoms. Note that for the case of three-body losses in a thermal cloud, the model takes into account a temperature increase of $\zeta k_B T$ with $\zeta \approx 1$ per lost atom due to recombination heating [57].*

The peak density of a thermal cloud scales linearly with N, whereas according to eq. (3.28) for a BEC it only grows with $N^{2/5}$ yielding different λ. The results of the integration for the different cases can be found in table 3.2.

In figure 3.8, we show typical loss curves of trapped sodium clouds. Experimentally, we prepare thermal atoms in the $|2,2\rangle$ or $|1,1\rangle$ state in the ODT, which we can bose-condense by forced evaporative cooling. The trap loss is recorded in dependence of the hold time t as shown for a $|2,2\rangle$ BEC and a $|1,1\rangle$ thermal cloud.

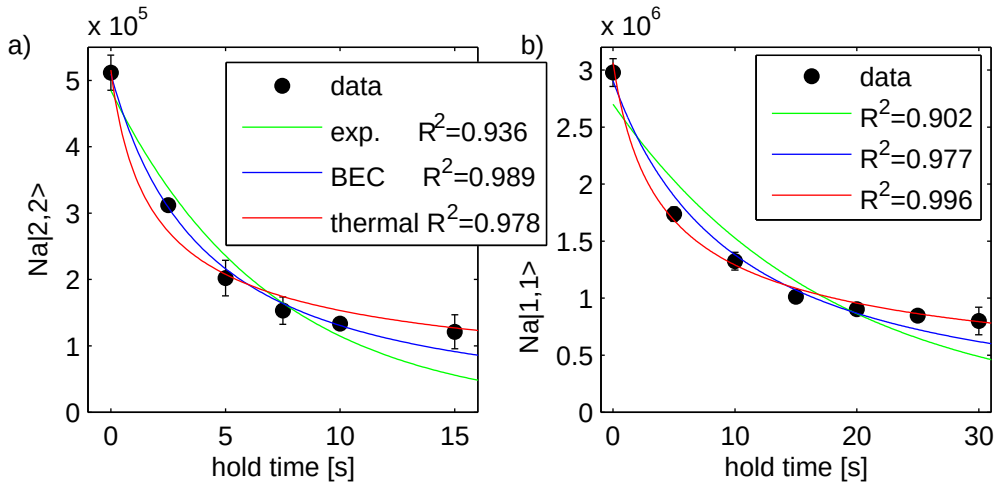

Figure 3.8.: *Loss curves for a $|2,2\rangle$ BEC* ***(a)*** *and a $|1,1\rangle$ thermal cloud* ***(b)****. Note the different time scales on the t-axes. Each dataset is fitted with an exponential, a BEC and a thermal cloud loss curve (see table 3.2). One can see by eye that the exponential fit is not the correct description, but to get a quantitative handle on the fit quality one can consider the R^2 value, which for good fits is supposed to take a value $\to 1$. For the loss curves above, R^2 indicates that the BEC fit is superior compared to the thermal fit when the atoms are condensed and vice versa.*

From the loss curves, we can extract the 3-body loss coefficient L_3. From the respective fits to sodium BECs in $|2,2\rangle$ and $|1,1\rangle$, we get $L_3^{|2,2\rangle} = 3.3 \cdot 10^{-28} \frac{\mathrm{cm}^6}{\mathrm{s}}$ and $L_3^{|1,1\rangle} = 2.1 \cdot 10^{-29} \frac{\mathrm{cm}^6}{\mathrm{s}}$. The two loss coefficients differ by one order of magnitude, in agreement with Ref. [45], but the absolute values are off. A possible reason is that for long hold times the cloud is partly condensed and partly thermal, as described in detail below. This complexity could be circumvented by extracting L_3 from loss measurements of a thermal cloud. But that is also not straightforward, as the L_3 determined this way strongly scales with the temperature T^3, whereas the BEC loss curve has only ω and a as parameters, which are both known with high precision.

A useful observation is that the BEC data shows a constant temperature T determined from the thermal cloud size. The heating effect, which we would expect due to losses of the coldest atoms as discussed in section 3.3.3 is counteracted by the finite trap depth and

thermalization of the high density atom sample, i. e. by plain evaporation. Having this in mind, an interesting feature which can be observed when recording the losses from a condensed cloud is the temporally decreasing condensate fraction η as shown in figure 3.9.

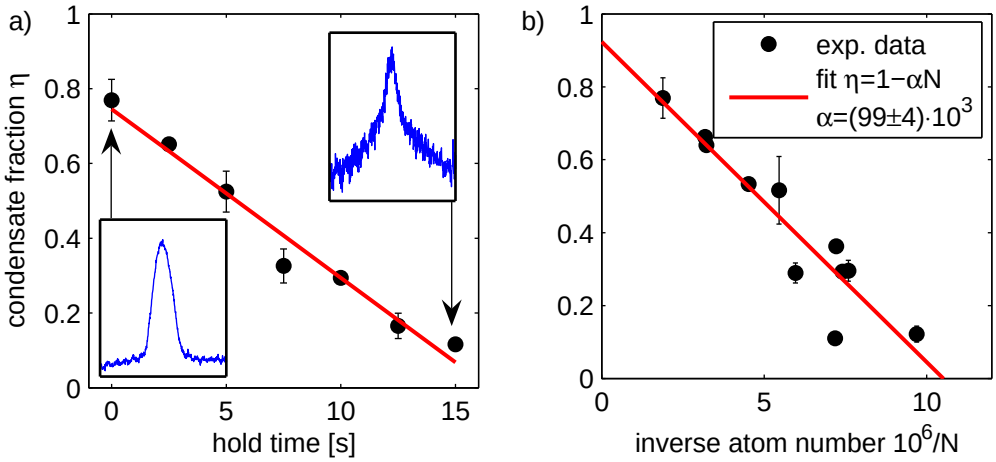

Figure 3.9.: *Decrease of the condensate fraction η of a sodium $|2,2\rangle$ BEC vs. time t* ***(a)*** *and inverse atom number $10^6/N$* ***(b)****. The insets in a) shows the sodium density profiles for high and low condensate fraction η. The errorbars in a) are obtained averaging over the datapoints of two runs, whereas in b) they originate from taking the mean of the fits in the two directions x and y.*

But rather than plotting the condensate fraction versus the time t, it is physically more meaningful to choose for the x-axis the inverse atom number $1/N$, as according to eqs. (3.29) and (3.30) we expect the scaling

$$\eta = 1 - \left(\frac{k_B T}{0.94\hbar\bar{\omega}}\right)^3 \frac{1}{N}\,. \tag{3.33}$$

Plotting and fitting the data accordingly, we get $\left(\frac{k_B T}{0.94\hbar\bar{\omega}}\right)^3 = (99\pm4)\cdot10^3$, which translates to a temperature of $T^{\mathrm{cond}} = (197\pm11)\,\mathrm{nK}$, with the error mainly determined by the uncertainties in the trapping frequencies. This result is in excellent agreement with the value we get from the fit to the thermal cloud $T^{\mathrm{therm}} = (180\pm93)\,\mathrm{nK}$, but has a way higher precision.

To conclude the subsection investigating the loss features of homonuclear samples, we want to stress that the value obtained for L_3 can not be attributed a high accuracy: As we have seen in the last paragraph, the condensate fraction is strongly decreasing over time, which makes our model, which for simplicity assumes a pure condensate, inaccurate. For a more precise determination of L_3, one could either measure with a pure thermal cloud or start with bigger condensates and just take the initial atom loss for fitting into account, where η changes only slightly. From the theoretical side, one could also implement a numerical

model taking both the BEC and the thermal cloud into account, but this is far beyond the scope of this thesis.

Important for all further measurements are the long timescales $\mathcal{O}(30\,\mathrm{s})$ of losses in a $|1,1\rangle$ BEC, which makes it possible to observe interspecies effects in the lifetimes of heteronuclear samples, as we will see in the following.

3.4.3. Loss Analysis of Trapped Heteronuclear Atom Samples

Having understood the loss spectra of sodium in different hyperfine states, we will in the following investigate what happens if we add lithium. The fermion is non-interacting due to Pauli blocking and the freezing out of p-wave scattering at ultracold temperatures. Nevertheless, lithium can show homonuclear losses due to p-wave resonances at certain magnetic fields [58, 59], which are however not interfering with our measurements presented in the following.

In general, the loss equation for lithium in the mixture reads

$$\dot{n}_{\mathrm{Li}} = -\Gamma n_{\mathrm{Li}} - L_2^{\mathrm{NaLi}} n_{\mathrm{Li}} n_{\mathrm{Na}} - L_3^{\mathrm{NaLi}} n_{\mathrm{Li}} n_{\mathrm{Na}}^2. \tag{3.34}$$

Due to the fermionic statistics of lithium, a three-body loss event always involves two sodium and one lithium atom, as mathematically described in eq. (3.34). Experimentally, we usually have $n_{\mathrm{Na}} \gg n_{\mathrm{Li}}$ and thus we will in the following make the assumptions that during the loss

- no sodium is lost, i. e. $n_{\mathrm{Na}} = \mathrm{const.}$
- the temperature of the sample is constant, which means that we can write $n_{\mathrm{Li}} = N_{\mathrm{Li}} f(x,T)$ with $f(x,T)$ being the distribution of thermal atoms in the trap (we neglect small effects due to a possible slight lithium degeneracy)

A constant temperature is ensured by the trap depth of our ODT in combination with a good interspecies thermalization rate, but the assumption of constant sodium number gives rise to systematic errors in our evaluation, which will be taken into account where necessary. Integrating eq. (3.34) over space and solving the differential equation, we get for the lithium atom number

$$N_{\mathrm{Li}}(t) = N_{\mathrm{Li}}(0) \cdot e^{-(\Gamma+\Gamma_2+\Gamma_3)t} \tag{3.35}$$

with $\Gamma_n = L_n \int \mathrm{d}V\, f(x,T) n_{\mathrm{Na}}^{(n-1)}$. We see that the lithium loss is – under the simplifying assumptions made – purely exponential.

As most simple case we prepare both species in their respective ground state, $\mathrm{Na}|1,1\rangle$ and $\mathrm{Li}|1/2,1/2\rangle$. As shown before in section 3.3.2, there can be no inelastic two-body loss from that state and so $\Gamma_2 = 0$. Thus the lithium loss shown in figure 3.10 is only given by background $\Gamma_1 > 0$ and three-body losses $\Gamma_3 > 0$ with the sodium. To account for the three-body losses with lithium, we plot the sodium numbers as $N_{\mathrm{Na}} - 2N_{\mathrm{Li}}$ and fit the data with the three-body loss curve of a BEC. In comparison with a pure $\mathrm{Na}|1,1\rangle$ sample shown

in figure 3.8 b), we see qualitative agreement of the loss curves, which decrease with similar time constants.

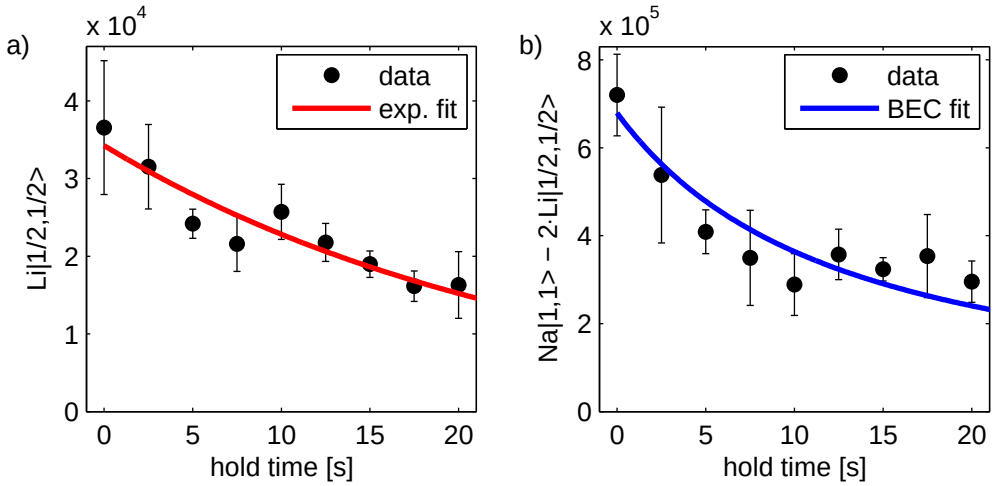

Figure 3.10.: *Losses in a* $\mathrm{Li}\,|1/2,1/2\rangle\,\mathrm{Na}\,|1,1\rangle$ *mixture. The lithium* **(a)** *is fitted with a purely exponential loss yielding a time constant of* $\tau = (24.6 \pm 3.5)\,\mathrm{s}$*. The sodium atom number* **(b)** *is first rescaled to account for the three-body loss and then fitted with the condensate loss formula from table 3.2.*

More interesting is the case of $\mathrm{Na}|1,1\rangle\mathrm{Li}|1/2,-1/2\rangle$. As we already saw in figure 3.5, this is the energetically lowest spin state with $M_F = 1/2$ for $B > 80\,\mathrm{G}$, i. e. $L_2(B > 80\,\mathrm{G}) = 0$, but in the low field range $\mathrm{Na}|1,0\rangle\mathrm{Li}|1/2,1/2\rangle$ is a possible spin exchange loss channel. Recalling the formula for the spin exchange loss rate eq. (3.16)

$$L_2 = P_{i\to f} = 4\pi\sqrt{2E/\mu}(a_s - a_t)^2\,|\eta_{\mathrm{spin}}|^2 \tag{3.36}$$

we see that we roughly expect maximal loss where the energy between the two states is maximized ($B \approx 40\,\mathrm{G}$). A more precise calculation also taking the energy dependence of η_{spin} into account yields, that $P_{i\to f}$ is maximized for $B \approx 34\,\mathrm{G}$.

Figure 3.11 a) shows lithium loss curves recorded while applying an external magnetic field $B = 0\,\mathrm{G}$ and $B = 40\,\mathrm{G}$, respectively. The effect of spin-exchange losses is lower than naively expected, as also reflected in the fit results, which agree within their error bars. Therefore, instead of measuring single loss curves, we map out the remaining number of atoms after a fixed time $t = 20\,\mathrm{s}$ in dependence of the applied magnetic field B. We clearly see in figure 3.11 that for fields below $80\,\mathrm{G}$ there are less atoms left than for higher fields, which we can quantify using as fitfunction $N(B) = N_0\exp(-c\sqrt{E(B)}\eta^2_{\mathrm{spin}}(B))$ with N_0 and c being free parameters. Assuming Γ and Γ_3 of eq. (3.35) as independent of the magnetic field, we get

$$N_{\mathrm{Li}}(B = 34\,\mathrm{G}) = N_{\mathrm{Li}}(B > 80\,\mathrm{G}) \cdot e^{-\Gamma_2(B=34\,\mathrm{G})t} \tag{3.37}$$

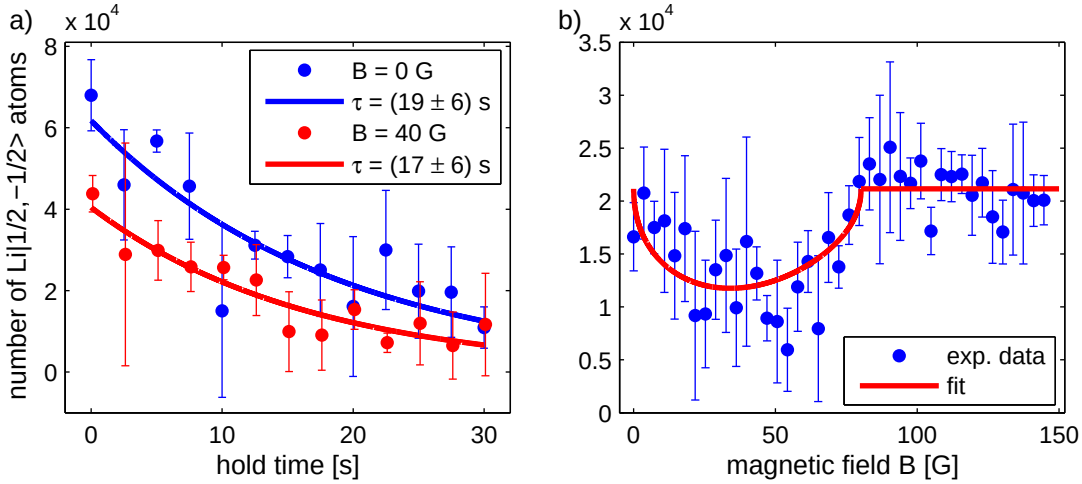

Figure 3.11.: ***a)*** *Loss curves of* $\mathrm{Li}\,|1/2,-1/2\rangle$ *for* $B = 0\,G$ *(blue) and* $B = 40\,G$ *(red) with a* $\mathrm{Na}\,|1,1\rangle$ *background. Each point is an average of three experimental runs. The solid lines are exponential fits to the data, yielding the same time constant within the error bars.* ***b)*** *Remaining number of lithium atoms after a fixed hold time of* $t = 20\,\mathrm{s}$*. Each point is an average of four to five experimental runs. The red solid line is a fit to the data taking the magnetic field dependence of* E *and* η_{spin} *for the spin exchange process* $\mathrm{Li}\,|1/2,-1/2\rangle\,\mathrm{Na}\,|1,1\rangle \rightarrow \mathrm{Li}\,|1/2,1/2\rangle\,\mathrm{Na}\,|1,0\rangle$ *into account as detailed in the text. Note that a) and b) have been obtained with different sodium background densities.*

with $N_{\mathrm{Li}}(B > 80\,\mathrm{G}) = (2.1 \pm 0.1) \cdot 10^4$ and $N_{\mathrm{Li}}(B = 34\,\mathrm{G}) = (12 \pm 2) \cdot 10^3$ from our fit. After integrating the density distribution $\Gamma_2 = L_2 \int \mathrm{d}^3x f(x,T) n_{\mathrm{Na}}$, we get

$$L_2 = (7.8 \pm 4.6) \cdot 10^{-15} \frac{\mathrm{cm}^3}{\mathrm{s}}\,. \tag{3.38}$$

The large uncertainty stems from the systematics in sodium number and condensate fraction, which decrease during $t = 20\,\mathrm{s}$ by a factor of ~ 2.3 (see figure 3.10) or from 50% to 20%, respectively. Moreover, the uncertainty in temperature determination contributes to the statistical error. Note that in the calculation of L_2, we had to take the gravitational sag $\Delta z = g \cdot ((1/\omega_z^{\mathrm{Li}})^2 - (1/\omega_z^{\mathrm{Na}})^2) \approx 9\,\mu\mathrm{m}$ into account, which reduces the value of the overlap integral of lithium with the condensate to $\sim 70\%$ and with the thermal cloud to $\sim 80\%$, thus leading to an overall overlap decrease of $\sim 75\%$. With the energy difference $E = 6.03\,\mathrm{MHz}$ from the Breit-Rabi formula and the spin factor

$$\eta_{\mathrm{spin}}(B = 34\,\mathrm{G}) = \frac{1}{2}\beta_{\mathrm{f}}^{*\mathrm{Na}}\alpha_{\mathrm{f}}^{*\mathrm{Li}}\alpha_{\mathrm{i}}^{\mathrm{Na}}\beta_{\mathrm{i}}^{\mathrm{Li}} = \frac{1}{2} \cdot 0.7259 \cdot 0.4339 \cdot 0.4802 \cdot 0.7382 \tag{3.39}$$

which we obtain from diagonalization of the Breit-Rabi-Matrix eq. (3.4), we obtain the important result

$$|a_s - a_t| = (5.9 \pm 1.7)\,a_0 \tag{3.40}$$

for the difference between triplet and singlet scattering length. This small value explains why it was not easy to recognize the effect of two-body loss in the loss curves directly and why our result for L_2 is so untypically small.

In this chapter, we have developed an understanding of the behaviour of different atomic spin states in magnetic fields and shown how to manipulate and analyze them. The timescales obtained by measuring loss curves for different atomic samples were shown to be so long that e. g. thermalization measurements could be easily done without the detrimental effects of substantial losses. In chapter 5 we will see how our experimental findings about the scattering length can contribute to the understanding of the NaLi Feshbach resonance spectrum.

4. Sodium Intraspecies Feshbach Resonances

To develop an understanding of Feshbach resonances, we will first treat the homonuclear case, which could be used to tune α due to its dependence on the condensate intraspecies scattering length. To interpret the spectrum of s-waves obtained in our experiment, we first introduce the Moerdijk model, which will turn out not to be sufficient to explain all resonances. Therefore, the asymptotic bound-state model (ABM) as an extension is introduced and a complete understanding of the s-wave resonance spectrum is developed and an analysis of the higher partial wave resonances together with the results of a coupled-channels calculation are given. Finally, we show how to obtain the scattering length for an arbitrary spin channel from the triplet and singlet scattering lengths a_s and a_t.

4.1. s-wave Resonance Spectrum

Summing up what we introduced in the last chapters, we see that the Hamiltonian for two atoms interacting with an external magnetic field applied can be written as

$$H = T + H_{\mathrm{hf}} + H_{\mathrm{Z}}(B) + U(r) \tag{4.1}$$

with $T = -\hbar^2\nabla^2/(2\mu)$ being the particles' relative kinetic energy,

$$H_{\mathrm{hf}} = \frac{a_\alpha}{\hbar^2}\vec{s}_\alpha \cdot \vec{i}_\alpha + \frac{a_\beta}{\hbar^2}\vec{s}_\beta \cdot \vec{i}_\beta \tag{4.2}$$

the hyperfine interaction and

$$H_{\mathrm{Z}} = \left[(g_{s\alpha}s_{z\alpha} + g_{i\alpha}i_{z\alpha}) + (g_{s\beta}s_{z\beta} + g_{i\beta}i_{z\beta})\right]\frac{\mu_B B}{\hbar} \tag{4.3}$$

the Zeeman term. The interatomic potential can be projected onto its singlet and triplet part by the operators[1] P_X and P_a yielding

$$U(r) = U_X(r)P_X + U_a(r)P_a. \tag{4.4}$$

[1]Note that in comparison to the previous chapter we changed the indices indicating the total spin from s to X for the singlet and t to a for the triplet to be consistent with the notation of molecular physics and our paper [26].

Using that Hamiltonian, we want to investigate the characteristics of Feshbach resonances in a certain atomic system, starting with determining their position. From chapter 2, we know that a Feshbach Resonance occurs[2] when a molecular state crosses the free atom threshold. Thus, we have to calculate the eigenstates of eq. (4.1) and determine the crossings of their respective energy with the free atom threshold, latter simply being given by the Breit-Rabi formula eq. (3.5).

For the diagonalization of eq. (4.1), we first have to choose a suitable basis set. Denoting the total molecular spin as $\vec{f} = \vec{f_\alpha} + \vec{f_\beta}$ and the total molecular angular momentum as $\vec{F} = \vec{f} + \vec{l}$ with $\vec{l}$ being the orbital angular momentum of the atoms' relative motion, we see that these quantities are only conserved for $B = 0$. Their respective projection $m_f = M_S + M_I = m_{s,\alpha} + m_{s,\beta} + m_{i,\alpha} + m_{i,\beta}$ and $M_F = m_f + m_l$ are conserved for all magnetic fields B, and furthermore M_S is a good quantum number for high magnetic fields B which yield $H_{\mathrm{Z}}(B) \gg H_{\mathrm{hf}}$. Thus the choice of $|l, m_l\rangle\,|S, M_S, I, M_I\rangle$ as basis set is appropriate.[3]

As an ansatz, we choose to diagonalize Hamiltonian eq. (4.1) starting from the molecular levels, a method related to deperturbation theory commonly used in the context of molecular spectra [60]. We can write the molecular wave function $|\nu l, \sigma\rangle = |\Psi_\nu^{S,l}\rangle\,|\sigma\rangle$ as a product of spin part $|\sigma\rangle$ and spatial part $|\Psi_\nu^{S,l}\rangle$ being dependent on the spin $S = 0, 1$, vibrational quantum number ν and the atoms' relative angular momentum l.

The matrix elements of the Hamiltonian of our homonuclear system, i. e. $\alpha = \beta$ in the previous equations, read

$$\begin{aligned} H_{\nu' l' \sigma', \nu l \sigma} = \varepsilon_\nu^{S,l} \delta_{\nu,\nu'} \delta_{l,l'} \delta_{\sigma,\sigma'} + \mu_B B (g_s M_S + g_i M_I) \delta_{\nu,\nu'} \delta_{l,l'} \delta_{\sigma,\sigma'} \\ + a_{hf} \delta_{l,l'} \eta_{\nu,\nu'}^{SS'}(l)\, \langle \sigma' | \vec{s}_1 \vec{i}_1 + \vec{s}_2 \vec{i}_2 | \sigma \rangle \,/\hbar^2. \end{aligned} \tag{4.5}$$

Here, δ_{ij} denotes the Kronecker δ, $\varepsilon_\nu^{S,l}$ the binding energy of the rovibrational level (ν, l) of the singlet $S = 0$ or triplet $S = 1$ potential. The last term is responsible for coupling of singlet and triplet levels, as we will further elucidate by means of a complete explanation of the sodium intraspecies Feshbach resonance spectrum. From the orthogonality of the molecular wavefunctions within the singlet and triplet manifold, respectively, it is clear that the Franck-Condon factor $\eta_{\nu,\nu'}^{S,S}(l) = \langle \Psi_\nu^{S,l} | \Psi_{\nu'}^{S,l} \rangle = \delta_{\nu,\nu'}$, i. e. different vibrational molecular states having the same electron spin S can not be coupled directly.

To gather some first insight into the working mechanisms of our model, we restrict ourselves to the simple case of just one rovibrational molecular level of each spin state involved, described by the quantum numbers $|\nu_a, l = 0, S = 1\rangle$ and $|\nu_X, l = 0, S = 0\rangle$. Motivated by our experiments, we choose as atomic states sodium atoms in the $|1, 1\rangle$ state, which thus defines the basis states the Hamiltonian has to be diagonalized in. Recalling that $M_F = m_l + M_S + M_I = 2$ has to be conserved, we get with $i_{\mathrm{Na}} = 3/2$ the possible states listed in

[2] Of course this is just an approximation, but in the frame of our work, which almost exclusively deals with narrow resonances, this describes the situation very well.

[3] At this point, we could as well have chosen $|S, M_S, m_{i,1}, m_{i,2}\rangle$, which we will use later in the treatment of Feshbach resonances of distinguishable particles.

l	m_l	S	M_S	I	M_I	$(SI)f$	M_F
0	0	0	0	2	2	(02)2	2
0	0	1	-1	3	3	(13)2	2
			0	3	2	(13)3	2
			1	3	1	(13)4	2
			1	1	1	(11)2	2

Table 4.1.: *List of $l = 0$ states for each vibrational singlet (S=0) and triplet (S=1) state with $M_F = m_l + M_S + M_I = 2$ due to the choice of the atomic spin state. The last two colums show the quantum numbers $|f, M_F\rangle$ of the coupled basis, which adiabatically connects to the corresponding states $|M_S, M_I\rangle$ at high fields.*

table 4.1 by means of combinatorics. A further restriction for all states is that $l + S + I$ must be even to yield a symmetric bosonic wavefunction. In the specific case of s-wave scattering, where $l = 0$ and thus the spatial wavefunction is symmetric, this means that the spin wavefunction needs to be symmetric as well, i. e. $S + I$ must be even.

The first part of eq. (4.5) can be easily evaluated, but the hyperfine structure term needs some more effort. To get a handle on it, we can rewrite its spin part as

$$\begin{aligned} \vec{s}_1\vec{i}_1 + \vec{s}_2\vec{i}_2 &= \frac{1}{2}\left[(\vec{s}_1 + \vec{s}_2)(\vec{i}_1 + \vec{i}_2) + (\vec{s}_1 - \vec{s}_2)(\vec{i}_1 - \vec{i}_2)\right] \\ &= \frac{1}{2}\left(\vec{S}\cdot\vec{I} + \vec{S}'\cdot\vec{I}'\right) \end{aligned} \tag{4.6}$$

where we have defined $\vec{S}' \equiv \vec{s}_1 - \vec{s}_2$ and $\vec{I}' \equiv \vec{i}_1 - \vec{i}_2$.

4.1.1. Moerdijk Model

The term $\vec{S}' \cdot \vec{I}'$ induces a coupling of singlet and triplet states. In order to simplify the problem for a first understanding we will neglect it, i. e. only consider the problem of decoupled singlet an triplet states. This approximation is known as Moerdijk model [61] and is valid for small singlet-triplet coupling, which can be assumed in our case as we will see later. Noting that we can write

$$\vec{S}\cdot\vec{I} = I_z S_z + \frac{1}{2}\left(I_+ S_- + I_- S_+\right) \tag{4.7}$$

with the spin raising and lowering operators eqs. (3.3) introduced in the previous chapter, we can write the Hamilton matrix using the states of table 4.1 as basis and get

$$H_{\text{Moerdijk}} = \begin{pmatrix} H_{S=0}^{I=2} & 0 & 0 \\ 0 & H_{S=1}^{I=3} & 0 \\ 0 & 0 & H_{S=1}^{I=1} \end{pmatrix}. \tag{4.8}$$

Here, $H^{I=2}_{S=0} = \varepsilon^X_\nu + 2\mu_B B g_i$ and $H^{I=1}_{S=1} = \varepsilon^a_\nu + \mu_B B(g_s + g_i) + \frac{a_{\mathrm{hf}}}{2\hbar^2}$ are single matrix elements, whereas $H^{I=3}_{S=1}$ contains off-diagonal elements and can be written as

$$H^{I=3}_{S=1} = \begin{pmatrix} \varepsilon^a_\nu + \mu_B B(-g_s + 3g_i) - \frac{3a_{\mathrm{hf}}}{2\hbar^2} & \frac{\sqrt{3}a_{\mathrm{hf}}}{2\hbar^2} & 0 \\ \frac{\sqrt{3}a_{\mathrm{hf}}}{2\hbar^2} & \varepsilon^a_\nu + 2\mu_B B g_i & \frac{\sqrt{5}a_{\mathrm{hf}}}{2\hbar^2} \\ 0 & \frac{\sqrt{5}a_{\mathrm{hf}}}{2\hbar^2} & \varepsilon^a_\nu + \mu_B B(g_s + g_i) + \frac{a_{\mathrm{hf}}}{2\hbar^2} \end{pmatrix} . \quad (4.9)$$

Matrix (4.8) can be diagonalized for every magnetic field B yielding the result graphically presented in figure 4.2. It is indicated that by a change of the singlet and triplet binding energies ε^X_ν and ε^a_ν, one can shift the molecular spectrum and thus its crossings with the free atom threshold, which determine the position of Feshbach resonances.

Connection to Open and Closed Channel

Before we proceed, we want to discuss how the states retrieved by the diagonalization of eq. (4.8) are connected to the so-called open and closed channel introduced in chapter 2 and often found in literature. Therefore, we want to recall that we work in the basis $|S, M_S, I, M_I\rangle$, i. e. the matrix (4.8) is

$$H_{\mathrm{Moerdijk}} = \langle S, M_S, I, M_I | H | S, M_S, I, M_I \rangle . \quad (4.10)$$

Each of the scattering atoms is prepared in an atomic hyperfine state $|j\rangle = |f_1, m_{f,1}\rangle\,|f_2, m_{f,2}\rangle$. In the case of $|f_1, m_{f,1}\rangle = |f_2, m_{f,2}\rangle = |1, 1\rangle$, we have $M_F = 2$ and thus the appropriate basis set to determine open and closed channel reads

$$\begin{aligned} |f_1, m_{f,1}\rangle\,|f_2, m_{f,2}\rangle = |1,1\rangle\,|1,1\rangle\ , \\ |2,1\rangle\,|1,1\rangle\ , \\ |2,1\rangle\,|2,1\rangle\ , \\ |2,2\rangle\,|1,0\rangle\ , \\ |2,2\rangle\,|2,0\rangle\ . \end{aligned} \quad (4.11)$$

Via Clebsch-Gordan coefficients, those five states can be connected to the $|f, M_f\rangle$ states in table 4.1, which can then be written as functions of our basis states $|S, M_S, I, M_I\rangle$ as shown at the end of this chapter[4]. Expanding $\mathbb{1} = \sum_j |j\rangle\langle j|$, we can rewrite the Hamiltonian Matrix:

$$\begin{aligned} H_{\mathrm{Moerdijk}} &= \langle S, M_S, I, M_I | \mathbb{1} | H | \mathbb{1} | S, M_S, I, M_I \rangle \\ &= \langle S, M_S, I, M_I | \left(\sum_j |j\rangle\langle j| \right) | H | \left(\sum_{j'} |j'\rangle\langle j'| \right) | S, M_S, I, M_I \rangle \\ &= \sum_{j,j'} \langle S, M_S, I, M_I | j\rangle\langle j | H | j'\rangle\langle j' | S, M_S, I, M_I \rangle = U H U^\dagger \end{aligned} \quad (4.12)$$

[4]Note that this last transformation is dependent on the actual value of the magnetic field.

We see that for $|j\rangle = |j'\rangle = |1,1\rangle\,|1,1\rangle$, $H_{PP} \equiv \langle j|H|j\rangle$ defines the open channel. Noting the closed channel as Q, H can thus be written as

$$H = \begin{pmatrix} H_{PP} & H_{PQ} \\ H_{QP} & H_{QQ} \end{pmatrix}, \tag{4.13}$$

where the part H_{QQ} can be diagonalized leaving H_{PP} unaffected. This representation is particularly helpful to determine the widths of resonances [62]. Moreover, we get insight into the character of the open channel: Unlike for simplicity often stated, the open and closed channel are never pure singlet or triplet states[5]. As to be seen by eq. (4.12), open and closed channel are always a magnetic field dependent linear combination of singlet and triplet and can be retrieved by the appropriate unitary transformation of H_{Moerdijk}.

Application of the Moerdijk Model

As a first application of the Moerdijk model, we choose the $|1,1\rangle$ channel with resonances at 851.0 G and 905.1 G, which have already been known for a long time [4]. Additionally, due to our capability to apply external fields of up to 2.2 kG [38], we were able to measure a resonance at 2054.2 G. In the $|1,-1\rangle$ channel, we obtained a resonance at 1500.1 G. When extending the Breit-Rabi formula eq. (3.5) to negative magnetic fields, we see that e. g. $B < 0$ in the $|1,1\rangle$ channel corresponds to $B > 0$ in the $|1,-1\rangle$ channel. Thus the resonance at 1500.1 G in $|1,-1\rangle$ can be conveniently expressed as -1500.1 G resonance in $|1,1\rangle$. The loss curves presented in figure 4.1 show the number of atoms left after holding them for a certain time t_h at a magnetic field B. As we will see later, the hold time t_h strongly correlates to the resonance width.

By means of our data we will test the accuracy of the Moerdijk model. As an additional input we take data from magnetic field dependent molecular spectroscopy [63] telling us that the binding energy of the last singlet bound state is $\varepsilon_\nu^X = -10738$GHz. Plugging this number in and doing a least-squares fit with the triplet energy ε_ν^a as free parameter, we get the fit results listed in table 4.2 and graphically represented in figure 4.2. The overall resonance structure is well reproduced, but the numerical predictions deviate by ~ 3 G from the experimentally obtained values.

So far, the existence of the singlet state has no influence on the calculated resonance positions, as we are describing them using a pure triplet state which does not couple to a singlet state, a restriction which we will release in the following.

[5] Obviously if both atoms are in their respective stretched state $|f = i + s, m_f = f\rangle$, the open channel does have pure triplet character. But this case can be left out of the discussion as atoms in this state do not show magnetically tuneable Feshbach resonances.

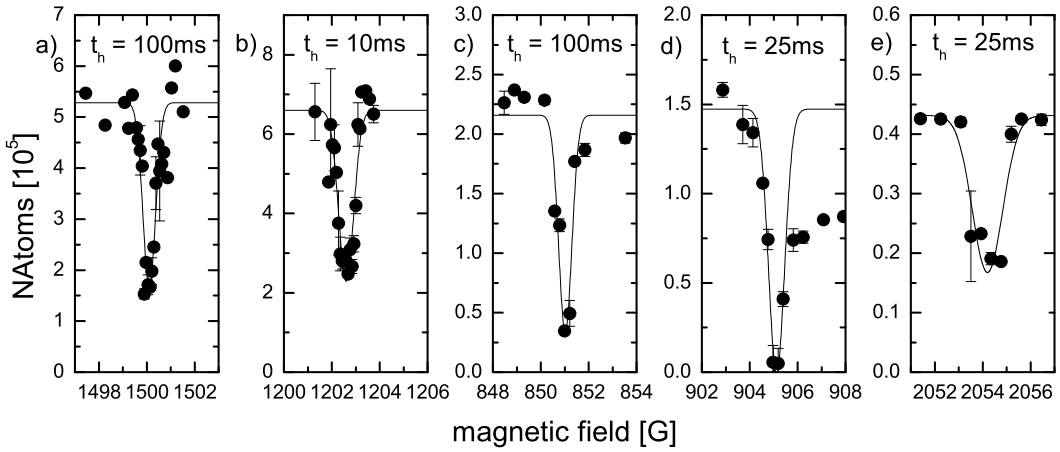

Figure 4.1.: *Feshbach spectroscopy of* $\mathrm{Na}\,|1,-1\rangle$ ***(a-b)*** *and* $\mathrm{Na}\,|1,1\rangle$ ***(c-e)*** *showing the number of atoms left after holding them for a certain time* t_h *at a magnetic field* B*. Each data point is an average over one to four experimental runs with the error bar representing the* 1σ *statistical uncertainty. The solid lines are Gaussian fits to determine the resonance positions. Due to the loss feature asymmetry caused by the relatively large width of resonance d), only the datapoints below the position of maximal loss have been taken into account for the fit.*

4.1.2. Asymptotic Bound-State Model

To include singlet-triplet coupling, we have to take the term $\propto \vec{S}' \cdot \vec{I}'$ of eq. (4.6), which we have neglected so far, into account. As already done for the term $\vec{S} \cdot \vec{I}$, we can write

$$\vec{S}' \cdot \vec{I}' = I'_z S'_z + \frac{1}{2}\left(I'_+ S'_- + I'_- S'_+\right) . \tag{4.14}$$

With the help of the common expansion of triplet and singlet states $|S, M_S\rangle$ in $|m_{s,1}, m_{s,2}\rangle$,

$$\begin{aligned} |1,1\rangle &= |1/2, 1/2\rangle \\ |1,0\rangle &= 1/\sqrt{2}(|1/2,-1/2\rangle + |-1/2,1/2\rangle) \\ |1,-1\rangle &= |-1/2,-1/2\rangle \\ |0,0\rangle &= 1/\sqrt{2}(|1/2,-1/2\rangle - |-1/2,1/2\rangle) \end{aligned} \tag{4.15}$$

we can easily verify the relations

$$\begin{aligned} S'_z &= s_{z,1} - s_{z,2} = |1,0\rangle\langle 0,0| + |0,0\rangle\langle 1,0| \\ S'_+ &= s_{+,1} - s_{+,2} = 1/\sqrt{2}(|0,0\rangle\langle 1,-1| - |1,1\rangle\langle 0,0|) \\ S'_- &= s_{-,1} - s_{-,2} = 1/\sqrt{2}(-|0,0\rangle\langle 1,1| + |1,-1\rangle\langle 0,0|) \end{aligned} \tag{4.16}$$

As already anticipated, we see that the $\vec{S}'$ operators act like the normal $\vec{S}$ operators with the difference that they couple between singlet and triplet states. The decomposition of the $\vec{I}'$ operators is more involved, as it is a priori not obvious how they act on our basis states $|I, M_I\rangle$. By writing

$$|I, M_I, i_1, i_2\rangle = \sum_{m_{i,1}+m_{i,2}=M_I} |i_1, m_{i,1}, i_2, m_{i,2}\rangle \langle i_1, m_{i,1}, i_2, m_{i,2}|I, M_I, i_1, i_2\rangle \tag{4.17}$$

with $\langle i_1, m_{i,1}, i_2, m_{i,2}|I, M_I, i_1, i_2\rangle$ being the well known Clebsch-Gordan coefficients, we expand $|I, M_I\rangle$ in the new basis $|i_1, m_{i,1}, i_2, m_{i,2}\rangle$ that our operators

$$\begin{aligned} I'_z &= i_{z,1} - i_{z,2} \\ I'_\pm &= i_{\pm,1} - i_{\pm,2} \end{aligned} \tag{4.18}$$

can act on[6]. With the hyperfine part of the Hamiltonian written as

$$\begin{aligned} H_{\rm hf} &= a_{\rm hf}\delta_{l,l'}\eta^{SS'}_{\nu,\nu'}(l)\,\langle\sigma'|\vec{s}_1\vec{i}_1 + \vec{s}_2\vec{i}_2|\sigma\rangle\,/\hbar^2 \\ &= a_{\rm hf}\delta_{l,l'}\eta^{SS'}_{\nu,\nu'}(l)\,\langle\sigma'|\frac{1}{2}\left(\vec{S}\cdot\vec{I} + \vec{S}'\cdot\vec{I}'\right)|\sigma\rangle\,/\hbar^2 \equiv V^+_{\rm hf} + V^-_{\rm hf} \end{aligned} \tag{4.19}$$

the matrix of Hamiltonian eq. (4.5) denotes

$$H_{\rm ABM} = \begin{pmatrix} H_{S=0} & V^-_{\rm hf} \\ V^-_{\rm hf} & H_{S=1} \end{pmatrix} \tag{4.20}$$

with

$$H_{S=1}\begin{pmatrix} H^{I=3}_{S=1} & 0 \\ 0 & H^{I=1}_{S=1} \end{pmatrix}, \tag{4.21}$$

where latter incorporates already $V^+_{\rm hf}$ as offdiagonal terms (see eq. (4.9)).

The term $V^-_{\rm hf}$ is coupling singlet and triplet with a coupling strength proportional to the overlap parameter $\eta^{S,S'}_{\nu,\nu'}(l) = \langle\Psi^{S,l}_\nu|\Psi^{S',l}_{\nu'}\rangle$. It can be evaluated analytically if the state's binding energy is so small that the classical turning point r_c lies beyond the van-der-Waals

[6]The same expansion could already have been done for $\vec{S}'$, but there the number of states involved is still manageable such that one can as well do it by hand. Moreover, the expansion of $\vec{S}'$ is applicable to all alkali atom mixtures, as they all have one outer electron each.

radius R_{vdW}. Then, we have a halo state, which has only a very small fraction of its total probability density inside the classically allowed region, and thus η can be calculated using eq. (2.10) yielding a value close to 1. More generally, the van-der-Waals shape $-C_6/r^6$ can be used to describe the potential as long as $r \gg r_X$, where the exchange radius r_X is defined by the distance where the magnitude of the exchange interaction eq. (3.9) equals the one of the van der Waals interaction. States having an $r_c \gg r_X$ are called *asymptotic bound states* and their Franck-Condon factors are calculable by integrating the radial Schrödinger equation using the aymptotic shape $-C_6/r^6$ of the potential only [62, 64].

In our case of sodium, the triplet state with a binding energy of 5 GHz has its classical turning point for $r_c = 22a_0$, which has to be compared to typical[7] values of the exchange radius $r_X \approx 15a_0$ [65]. So we are certainly not in the regime where $r_c \gg r_X$ and therefore it is difficult to obtain the Franck-Condon factors η via calculations, thus they will serve as free parameters in the following, unless there is other sources to determine their values from.

ABM with one Singlet and one Triplet State

The width of the avoided crossing between the triplet $\nu_a = 14$ and singlet $\nu_X = 64$ states [63] gives an overlap $\eta^{0,1}_{64,14} \approx 0.85$. With this additional information at hand, one can diagonalize matrix eq. (4.20) and do a least-squares fit with the triplet energy ε^a_ν as free parameter, yielding the fit results listed in table 4.2 and graphically represented in figure 4.2.

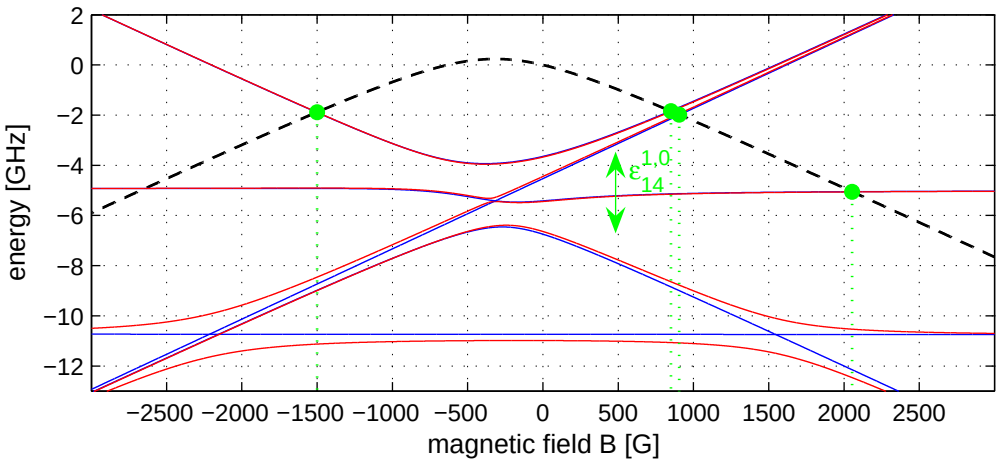

Figure 4.2.: *Different theoretical descriptions of measured resonance spectrum (green dots). The resonance positions can be adjusted by varying the triplet binding energy $\varepsilon^{1,0}_{14}$ to determine the crossing of the molecular states (blue: Moerdijk, red: ABM) with the atomic threshold (black dashed). The difference between the two models, i. e. the singlet-triplet coupling, is evident at the avoided crossings.*

[7] In our paper [26], we define an outer radius $R_{\mathrm{out}} = 21a_0$, which can as well serve as a measure of the exchange radius $r_X \approx R_{\mathrm{out}}$.

We see that the more realistic ABM model has not improved our fit with respect to the Moerdijk model, even made it worse. Besides the rms deviation from the fit result, one can exemplarily as in indicator also take distance in magnetic field between the two resonances around 900 G, $\Delta_{\text{exp}} = 54.1\,\text{G}$. Comparing that to the results of the Moerdijk and the ABM model, $\Delta_{\text{Moerdijk}} = 59.9\,\text{G}$ and $\Delta_{\text{ABM}} = 45.2\,\text{G}$, one can see that so far the theoretical description does not fit our experimental findings which have an uncertainty of not more than $\delta B = 0.5\,\text{G}$[8].

ABM with Virtual States

Our model so far lacks also the explanation of the resonance at $-1202.6\,\text{G}$, which has been first observed in Ref. [66]. To explain this resonace and improve on the overall fit, again motivated by [63] we take a so-called *virtual* singlet and triplet state, i. e. states with positive binding energies ε_ν^X and ε_ν^a, into account. As also to be seen in figure 4.3 a), despite they are continuum states for $B = 0$, for $B \neq 0$ they can become bound and are thus essential to describe both number and positions of the Feshbach resonances observed.

parameter	$\varepsilon_{64}^{0,0}$[MHz]	$\varepsilon_{14}^{1,0}$[MHz]	$\eta_{64,14}^{0,1}$	$\varepsilon_{65}^{0,0}$[MHz]	$\varepsilon_{15}^{1,0}$[MHz]	$\eta_{64,15}^{0,1}$	$\eta_{65,14}^{0,1}$	$\eta_{65,15}^{0,1}$
Moerdijk	-10738	**-4974.1**	—	—	—	—	—	—
ABM1	-10738	**-5000.7**	0.85	—	—	—	—	—
ABM2	-10738	**-4990.5**	0.85	1347	**1999.9**	**0.758**	**0.467**	**0.990**

exp. values	-1500.1 G	-1202.6 G	851.0 G	905.1 G	2054.2 G	rms deviation
Moerdijk	-1502.2 G	—	847.7 G	907.6 G	2053.6 G	4.7 G
ABM1	-1500.8 G	—	852.8 G	898.0 G	2056.5 G	7.7 G
ABM2	-1500.1 G	-1202.6 G	850.9 G	905.1 G	2054.2 G	0.13 G

Table 4.2.: *Results of the least-square fitting procedures using the Moerdijk model and the ABM with one singlet and triplet state (ABM1) and two (ABM2), respectively. The parameters varied for fitting are printed bold. The results are visualized in figures 4.2 and 4.3.*

With only five resonances at hand, a fit varying all eight free parameters is not meaningful. Moreover, e. g. the energy of the $\nu_X = 64, 65$ singlet states and their overlap parameters with the triplet states cannot be determined independently, as there is no measured resonance directly connected to the singlets. Thus, we take as additional information the data given in [63, 67] to get the values of $\varepsilon_{64}^{0,0}$, $\varepsilon_{65}^{0,0}$ and $\eta_{64,14}^{0,1}$. The optimization procedure only runs on the triplet bound state energies $\varepsilon_{14}^{1,0}$ and $\varepsilon_{15}^{1,0}$ as well as the Franck-Condon overlaps $\eta_{\nu,\nu'}^{S,S'}$. With all five measured resonances included, the least squares fit with two singlet and triplet states

[8] Depending on the exact magnetic field values and the coils used to apply it, our rf spectroscopy shows widths of 80 mG to 300 mG. The central value B_0 around which the field fluctuates can be determined with a much higher precision though, i. e. the value of $\delta B = 0.5\,\text{G}$ should only be considered as an upper bound.

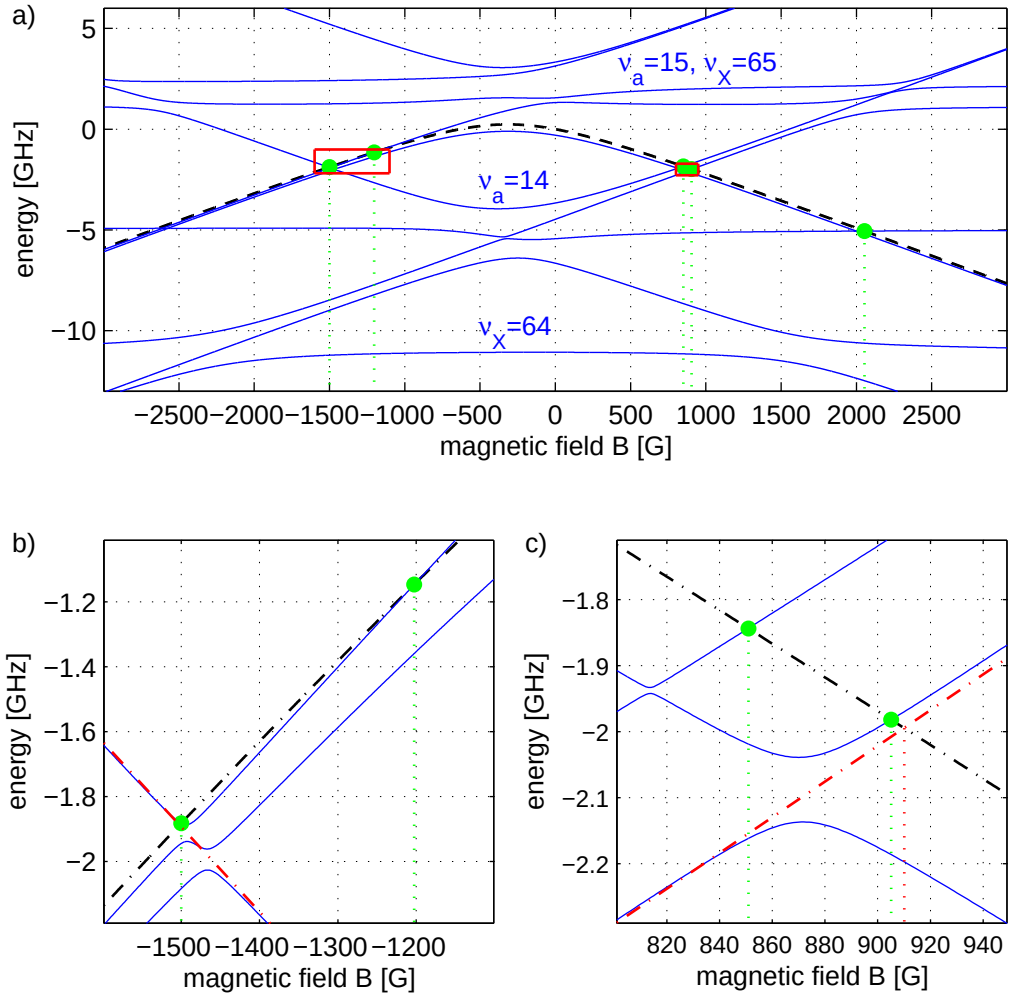

Figure 4.3.: ***a)*** *Description of the entire s-wave resonance spectrum using two molecular singlet and triplet states.* ***b)*** *The additional singlet is essential to explain the resonance at* $-1202.6\,\mathrm{G}$. ***c)*** *By the avoided crossing, the unperturbed resonance, which would show up at 910.1* G *(red dashed-dotted line), shifts by -5* G *to the experimentally observed value of 905.1* G.

and their respective overlap parameters $\eta_{\nu,\nu'}^{S,S'}$ yields the results listed in table 4.2. We see a drastic improvement in the rms error of the fit and an astonishing agreement of experimental data and theoretical explanation with deviation $\leq 0.1\,\mathrm{G}$. Zoom b) of figure 4.3 shows how the the $M_S = 1$ level of the virtual triplet state gives rise to the observed $-1202.6\,\mathrm{G}$ resonance, which can thus be used to pin down the energy of the virtual state $\varepsilon_{15}^{0,0}$. Moreover, especially zoom c) nicely illustrates how the indirect coupling between the triplet states $\nu_a = 14$ and $\nu_a = 15$ mediated via the $\nu_X = 65$ singlet shifts the position of the 905.1 G resonance from

the uncoupled position 910.1 G by −5 G to the observed experimental value. Thus, the theoretically calculated difference in magnetic field between the two $M_S = +1$ resonances now matches the experimentally obtained one.

To finish the chapter dealing with sodium s-waves, we finally want to discuss the resonance in state $|1,-1\rangle$ at 1202.6 G, which is special in several ways. It is the only s-wave resonance requiring a virtual triplet state to be explained. As to be seen in figure 4.3 b), this also leads to a very small difference in magnetic moments of the atomic threshold and the molecular state, i. e. there is a very nice tuning with the magnetic field according to eq. (2.24) where we have seen that $\Delta \propto 1/\delta\mu$. A more involved theoretical calculation [5] confirms this result.

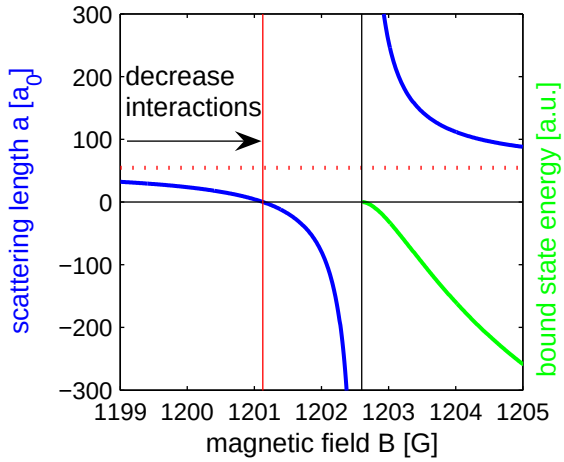

Figure 4.4.: *Sodium $|1,-1\rangle$ intraspecies resonance at 1202.6 G. Due to the negative width $\Delta < 0$, interactions are first decreased when increasing the magnetic field B. Thus $a = 0$ (vertical red line) can be achieved without the detrimental effects of three-body losses and molecule formation, latter being enabled by the appearance of a bound state (schematically shown as green line).*

Moreover, we can also see that the sign of $\delta\mu$ and thus Δ must be different for the 1202.6 G resonance compared to all others, which is also depicted in figure 4.4 depicting the results of the coupled-channels calculation [68] yielding $\Delta = -1.473$ G. We can see that in this case of a negative width an increase in magnetic field first leads to a decrease in interactions and one can even tune to $a = 0$, i. e. realize the textbook example of a non-interacting Bose gas without having to cross a resonance.[9] For even higher fields, the strongly interacting regime is entered with scattering lengths $a < 0$. A resonance with $\Delta < 0$ thus has the advantage that we can tune to weak interactions without having to cross the resonance. In the reverse case of $\Delta > 0$, tuning to $a = 0$ requires a ramp over the resonance, which leads

[9] Experimentally, being confronted with magnetic field instabilities $\delta B = \mathcal{O}(30\,\mathrm{mG})$, one can still tune to $a = a_{\mathrm{bg}}\delta B/|\Delta| \approx 1a_0$.

to three-body losses and – during the ramp back to zero field, where the atoms are imaged – molecule formation.

4.2. Higher Partial Waves

To explain the wealth of sodium intraspecies resonances measured [26], just including s-waves is not sufficient. Therefore, we also have to take the higher partial waves $l \neq 0$ in eq. (4.5) into account. In our case of two identical bosons colliding, the spin wavefunction must be symmetric, which then requires the spatial wavefunction to be symmetric as well, i. e. $l = 0, 2, 4, ...$ One could think that the observation of higher partial wave resonances is highly supressed due to our temperature of $T \approx 1\,\mu$K and a rotational barrier of 6 mK as calculated in chapter 2. But as we have seen in chapter 3, the dipole-dipole interaction (3.18) couples $l = 0$ with $l = 2$ states. Evaluating eq. (3.18) for $r = R_{\mathrm{vdW}}$, we get an associated energy of 3.8 MHz, which translates into a shift of the Feshbach resonance positions on the order of 1 G. Thus we can justify not to include the dipole-dipole interaction in the Hamiltonian, as its effect does not alter the Feshbach spectrum by much. Nevertheless, in the following we will take advantage of it by including d- and g-wave resonances in our considerations, which are coupled to the atoms having collision energies that only give rise to s-wave scattering. The dipole-dipole interaction circumvents the very weak tunneling of the scattering atoms through the high centrifugal barrier and thus makes higher partial wave resonances observable.

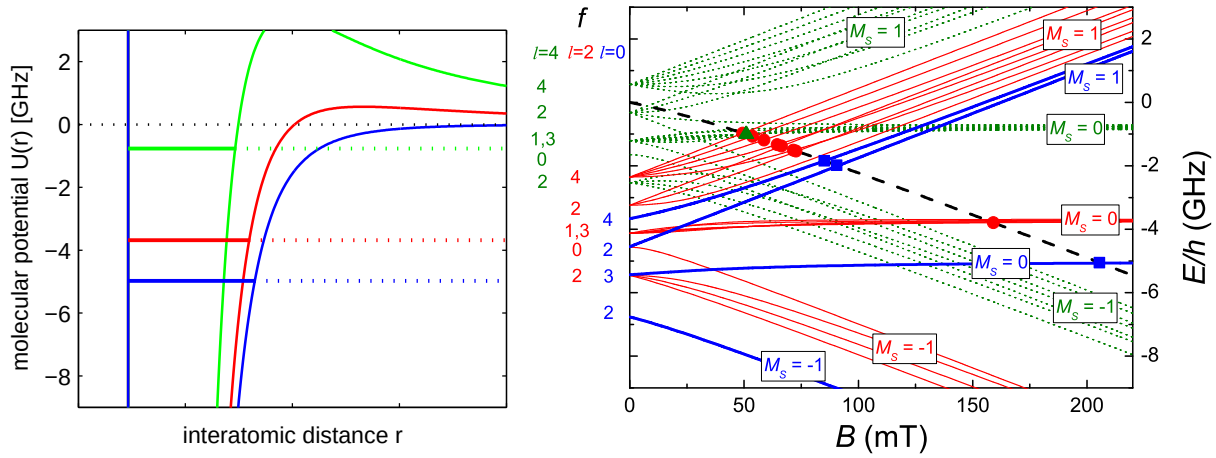

Figure 4.5.: *Moerdijk model of the $\nu_a = 14$ triplet state with $M_F = 2$ and $l = 0$ (thick blue lines), $l = 2$ (thin red lines) and $l = 4$ (dotted green lines). The energy of the atoms prepared in $|1,1\rangle + |1,1\rangle$ is shown as dashed black line. The experimentally measured Feshbach resonances are depicted by solid squares (s-waves), circles (d-waves) and triangles (g-waves). On the left, a sketch of the molecular triplet potential containing the $l = 0, 2, 4$ states indicates the molecular bound states which the Feshbach resonaces stem from.*

Binding energies and overlap parameters for s-waves:

$\varepsilon^{0,0}_{64}$	$\varepsilon^{1,0}_{14}$	$\eta^{0,1}_{64,14}(0)$	$\varepsilon^{0,0}_{65}$	$\varepsilon^{1,0}_{15}$	$\eta^{0,1}_{64,15}(0)$	$\eta^{0,1}_{65,14}(0)$	$\eta^{0,1}_{65,15}(0)$
-11000^{1}	-4991(1)	0.85^{1}	1400^{3}	2014(10)	0.79	0.47	1.0

Rotational splittings and overlap parameters for d-waves:

D^0_{64}	D^1_{14}	$\eta^{0,1}_{64,14}(2)$	D^0_{65}	D^1_{15}	$\eta^{0,1}_{64,15}(2)$	$\eta^{0,1}_{65,14}(2)$	$\eta^{0,1}_{65,15}(2)$
$1556(38)^2$	1309(2)	0.85^{1}	$504(38)^2$	$465(34)^2$	0.44	0.47	—

Rotational splittings for g-waves:

G^0_{64}	G^1_{14}	$\eta^{0,1}_{64,14}(4)$	G^0_{65}	G^1_{15}	$\eta^{0,1}_{64,15}(4)$	$\eta^{0,1}_{65,14}(4)$	$\eta^{0,1}_{65,15}(4)$
$5064(45)^2$	4214(2)	—	—	—	—	—	—

Table 4.3.: *Results of the ABM least-square fit including s-, d- and g-waves. All energies are given in* MHz*. Additionally to our measured resonances, we made use of molecular spectroscopy data, which are marked* ^{i}*, where* $i = 1, 2, 3$ *refers to publication [63],[69],[67].*

When $l = 2$ is allowed, the number of possible states $M_F = m_f + m_l$ increases from five shown in table 4.1 to 22+5, which are listed in [26]. Restricting ourselves to the Moerdijk model with the triplet $\nu_a = 14$ only, we see from eq. (4.5) that the only two new parameters are the binding energies $\varepsilon^{S,l}_\nu$ for $l = 2, 4$. Doing a least-squares fit with our experimental data[10], we get $\varepsilon^{1,0}_{14} = -4976\,\text{MHz}$, $\varepsilon^{1,2}_{14} = -3679\,\text{MHz}$ and $\varepsilon^{1,4}_{14} = -765\,\text{MHz}$. The resulting molecular spectrum shown in figure 4.5 together with the fit values in table 4.4 demonstrate that the Moerdijk model is sufficient to explain the resonance spectrum with deviations from the experimental values not exceeding 3 G.

As already done in the case of s-waves, we can include singlet-triplet coupling and use two singlets and triplets each to get a more precise description of our data. To reduce the large number of free parameters, we take the input of molecular spectroscopy experiments [69, 63, 67] and determine the rest of the parameters via a least-squares fit, whose results are shown in table 4.3. Here we defined the rotational splitting for d-waves as $D^S_\nu = \varepsilon^{S,2}_\nu - \varepsilon^{S,0}_\nu$ and analog for g-waves $G^S_\nu = \varepsilon^{S,4}_\nu - \varepsilon^{S,0}_\nu$. Interestingly, the shape of the potential is reflected in the rotational splittings: As the singlet potential is deeper and thus steeper as the triplet, its rotational splitting is bigger due to the lower centrifugal distortion and the resulting smaller moment of inertia.

Note that our fit is not unique, i. e. some of the parameters are strongly correlated such that they can not be varied independently. For instance, $\eta^{0,1}_{65,15}(l)$ and $\varepsilon^{0,l}_{65}$ are correlated, such that choosing a different $\eta^{0,1}_{65,15}(l)$ results in a different $\varepsilon^{0,l}_{65}$. Nevertheless, with the fit done here we can describe the experimental data with deviations of less than 0.5 mG as to be seen in table 4.4.

[10] At the time the paper was published, we had only measured resonances at fields $B > 0$, so this fit only takes those into account.

4.3. Results of the Coupled-Channels Calculation

In order to further improve on the fit results and to calculate resonance widths, a CC calculation based on Hamiltonian 4.5 with the full interaction potentials has been performed. In addition to our experimental data, also conventional spectroscopy data [70, 69, 63, 71, 67, 72, 73, 74] has been included in the analysis. As this work was done by our colleagues E. Tiesinga (NIST) and E. Tiemann (Universität Hannover), we will just summarize their methods and main results.

Modifications of the Hamiltonian

In eq. (4.2), we assumed a constant hyperfine constant $a_{\alpha,\mathrm{hf}}$. But for small interatomic distances, this will not hold any more due to the strong electronic distortions of one atom by the other. Thus, one makes the ansatz

$$a_\alpha(R) = a_{\alpha,\mathrm{hf}} \left(1 + \frac{c_f}{e^{(R-R_0)/\Delta R} + 1} \right), \tag{4.22}$$

where the CC calculation determines the constants as $c_f = -0.029$, $R_0 = 11.0a_0$ and $\Delta R = 1.0a_0$. Although just being a small correction, it shifts the resonances by up to 0.5G, more than our experimental uncertainty.

Moreover, we discussed the effects of spin-spin interaction, but did not take it into account in our Hamiltonian and just made use of the fact that it induces the coupling to observe higher partial waves in an ultracold atom sample. Doing some spin-algebra on eq. (3.18), we get the spin-spin interaction

$$V_{SS}(\vec{R}) = \frac{2}{3}\lambda(R)(3S_Z^2 - S^2)\,, \tag{4.23}$$

with

$$\lambda(R) = -\frac{3}{4}\alpha^2 \left(\frac{1}{R^3} + a_{\mathrm{SO}} e^{-b_{\mathrm{SO}}R} \right). \tag{4.24}$$

The first term in $\lambda(R)$ stems from the magnetic dipole-dipole interaction eq. (3.18), whereas the second is a second-order spin orbit contribution [67][11]. With $\lambda(R)$ and R given in atomic units, α is the fine structure constant.

Model potential, calculation and results

The modeling of the potential can be done by splitting it up in three parts: A short range repulsive interaction $U_{SR}(R)$, an intermediate region containing the potential minimum $U_{IR}(R)$, and a long range part $U_{LR}(R)$, which has in leading order the typical van-der-Waals shape $-C_6/R^6$. This potential inserted into the one-dimensional radial Schrödinger

[11] As the calculation shows, the value of a_{SO} has an estimated uncertainty of 100%.

			Exp.	Moerdijk	ABM	CC	
l	f	m_f	$B_0^{\exp}$(mT)	B_c(mT)	B_c(mT)	B_0(mT)	Δ(mT)
0	4	2	85.10(2)	84.82	85.10	85.114	9.7[-4]
0	2	2	90.51(4)	90.81	90.52	90.517	0.104
0	3	2	205.42(4)	205.45	205.44	205.501	0.012
2	4	4	49.36(2)	49.34	49.40	49.344	1.7[-4]
2	4	3	53.66(2)	53.57	53.63	53.650	3[-5]
2	4	2	58.63(2)	58.52	58.58	58.615	5[-6]
2	4	1	64.48(3)	64.41	64.47	64.477	3[-7]
2	2	2	66.28(3)	66.38	66.28	66.283	4[-7]
2	4	0	71.56(1)	71.54	71.60	71.556	2[-8]
2	2	1	72.71(1)	73.03	72.72	72.718	4[-7]
2	3	3	159.00(3)	159.02	159.13	159.011	2[-4]
4	3		50.80(2)	50.76	50.80	50.775	$< 5[-7]$
4	3		50.88(2)	50.89	50.89	50.859	$< 5[-7]$
4	3		51.09(2)	51.12	51.09	51.065	$< 5[-7]$

Table 4.4.: *Overview of the experimentally and theoretically obtained results on Feshbach resonances in Na prepared in the lowest hyperfine substate $|f, m_f\rangle = |1, 1\rangle$. Experimentally the position of maximum loss $B_0^{\exp}$ is given, which is determined by Gaussian fits to the loss features. The errors reflect the one standard deviation statistical uncertainty in the magnetic field calibration, determined by the FWHM of the RF calibration spectra and from the profile fit. The middle columns show the results for the Moerdijk and ABM models). The last two columns show the Feshbach resonance position B_0 and width Δ from the CC calculation. The brackets in the last column give the exponent to the power ten. To characterize the bound state, the quantum numbers l, f, m_f are used; note that for the l=4 states the m_f quantum numbers can not be assigned due to the strong mixing by the dipole-dipole interaction.*

equation 2.7 yields the wavefunction, which is used to determine the scattering length a in dependence of the applied magnetic field B. Analog to chapter 2, the Feshbach resonance positions are determined as the points where a diverges. With the help of additional photoassociation [71] and spectroscopic data [63, 72, 73, 74], one can adjust the potential parameters in an iterative way. As our resonances are caused by the least bound state, this procedure primarily improves the long-range shape of the potential, in particular we increase the precision of the least bound state energy by a factor of 50 from 15 MHz to 0.3 MHz.

4.3.1. Resonance Widths

Having calculated the wavefunctions, one can extract the scattering length $a(B)$ and thus get also the width Δ of each resonance, conveniently defined as the distance in magnetic

field between divergence and zero crossing of a. In order to get information about the width ratio of s- and d- wave resonances, one can for a very course estimate consider the associated energy scales: The dipole-dipole interaction evaluated at $r = R_{\mathrm{vdW}} = 45a_0$ yields 3.8 MHz representing the coupling of s- to d-states. The coupling giving rise to the s-wave resonances is connected to the hyperfine constant $a_{\mathrm{hfs}} = 886\,\mathrm{MHz}$, i. e. we would expect the width of s- and d-wave resonances to scale as the squared coupling ratio $(886/3.8)^2 \approx 5 \cdot 10^4$. Table 4.4 shows that this estimate gives some rough order of magnitude of the ratio of resonance widths.

Figure 4.6 depicts how the hold times used to map out a resonance scale with the respective calculated resonance widths. Although there was no systematics done concerning the hold time (we just chose it such that the resonance loss feature was not saturated), we see a clear connection of hold time and width in the double-logarithmic plot. This serves as an elegant experimental confirmation of the calculated resonance widths, most of which are too narrow to be resolved due to the technical noise of the magnetic field B [38].

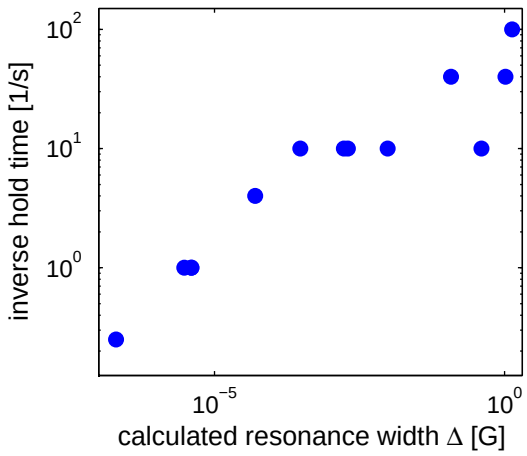

Figure 4.6.: *Relation of inverse hold time and calculated resonance width Δ. Although the values were not corrected for e. g. different densities, there is still a clear correlation.*

With the resonances measured at magnetic fields $B > 0$, it was also possible to predict resonances at negative fields, in particular the position of the $-1202.6\,\mathrm{G}$ resonance measured after publication was predicted to be at $-1207.5(5.0)\,\mathrm{G}$. The agreement between prediction and measurement is astonishing, as the resonances used to fit the spectrum in our paper [26] are only shifted weakly by the influence of the virtual triplet state, which gives rise to the described resonance at negative fields. The high predictive power of the model potential shows the great applicability of Feshbach resonances to map out the long-range shape of the potential in combination with molecular spectroscopy data.

4.3.2. Scattering Length for Different Spin Channels

Singlet and triplet potential can be each assigned a scattering length a_s and a_t, respectively. From the coupled channels calculations, one gets $a_s = 18.81(80)a_0$ and $a_s = 64.30(40)a_0$. When prepared in a certain spin state, the atoms have (unless they are in the stretched state) both singlet and triplet character. In order to get the background scattering length a for a certain spin channel, one thus has to figure out its singlet and triplet fraction. We thus write

$$|f_1, f_2, m_{f,1}, m_{f,2}\rangle = \sum_{f, m_f = m_{f,1}+m_{f,2}} \langle f_1, f_2, f, m_f | f_1, f_2, m_{f,1}, m_{f,2}\rangle \, |f_1, f_2, f, m_f\rangle \qquad (4.25)$$

with $\langle f_1, f_2, f, m_f | f_1, f_2, m_{f,1}, m_{f,2}\rangle$ being the well-known Clebsch-Gordan coefficients. In order to describe the overlap between the state $|f_1, f_2, f, m_f\rangle$ and the molecular state being characterized by $|S, I, M_S, M_I\rangle$ (see table 4.1), one has to decompose

$$|f_1, f_2, f, m_f\rangle = \sum_{S, I, m_f = M_S + M_I} \langle S, I, M_S, M_I | f_1, f_2, f, m_f\rangle \, |S, I, M_S, M_I\rangle \qquad (4.26)$$

The factor $\langle S, I, M_S, M_I | f_1, f_2, f, m_f\rangle$ describes the coupling of four spins and can be written as

$$\langle S, I, M_S, M_I | f_1, f_2, f, m_f\rangle = \sqrt{(2S+1)(2I+1)(2f_1+1)(2f_2+1)} \begin{Bmatrix} s_1 & i_1 & f_1 \\ s_2 & i_2 & f_2 \\ S & I & f \end{Bmatrix} \qquad (4.27)$$

with the last factor being a Wigner 9j symbol, which can either be expressed in terms of 6j symbols or directly be calculated.[12] Table 4.5 shows the results of applying the procedure presented above exemplarily on different spin channels of sodium, with the experimentally most relevant result

$$a_{|1,1\rangle} = \frac{3}{16} a_s + \frac{13}{16} a_t \,. \qquad (4.28)$$

spin state	$\|1,1\rangle + \|1,1\rangle$	$\|1,0\rangle + \|1,0\rangle$	$\|1,1\rangle + \|1,-1\rangle$
decomposition	$55.77(36)a_0$	$52.03(36)a_0$	$50.08(37)a_0$
CC calculation	$54.54(20)a_0$	$52.66(40)a_0$	$50.78(40)a_0$

Table 4.5.: *Background scattering values for different spin channels obtained with a simple decomposition as described in the text and with the CC calculation.*

We see good, but not perfect agreement between our method and the full coupled channels calculation. The differences stem from our simplified description using either the atomic

[12] Care has to be taken with http://www.svengato.com/ninej.html, which does not give the analytical result correctly. Only numerical, but correct results are given by http://plasma-gate.weizmann.ac.il/369j.html.

$|f_1, f_2, f, m_f\rangle$ or molecular $|S, I, M_S, M_I\rangle$ basis, which is not applicable in general, as scattering occurs at distances where neither of them provides the appropriate physical description. Thus, in order to get the correct background scattering length, the full CC calculation is needed.

In this chapter, we have introduced the ABM model and shown how it can be used to analyze Feshbach spectra. With this knowledge at hand, we will explain the NaLi Feshbach spectrum in the next chapter.

5. Sodium-Lithium Interspecies Feshbach Resonances

As explained in the introduction, one of the main goals of our experiment is to investigate polarons, whose nature is determined by the parameter $\alpha = \frac{a_{IB}^2}{a_{BB}\xi}$. In the last chapter we learned about the tuning properties of a_{BB}, but due to the quadratic dependence one would rather like to have a handle on a_{IB}. Therefore, in the following we will investigate the Feshbach spectrum of the NaLi mixture, starting from the experimental and theoretical knowledge at the time when our experiment started [75, 76]. Our measurements of sign and magnitude of the scattering length provide important input for the following analysis of the Feshbach spectrum, which turns out to differ completely from the expectations. Using the ABM, we identify 23 of the 26 measured Feshbach resonances as d-waves, which is confirmed by a coupled-channels calculation yielding scattering lengths in excellent agreement with the experimentally obtained values. Important features in the resonance spectrum are discussed by means of the atomic and molecular structure.

5.1. Previous Knowledge about NaLi Scattering Properties

From the sucess of sympathetic cooling in the early NaLi experiments [42, 43], one can already infer that the triplet scattering length between sodium and lithium must be sufficiently high.[1] Moreover, there were also three experimentally known interspecies Feshbach resonances for this system [75]. Based on those, Gacesa *et al.* made predictions of further resonances including the widths [76], which are summarized in table 5.1. Naturally, the resonance at $B_0^{\text{th}} = 1186\,\text{G}$ having a width $\Delta = 8.7\,\text{G}$, seemed from the experimental point of view very appealing to us, such that we designed our antibias coils in a way they could create such high fields.

As minor results of that paper, also the singlet and triplet scattering lengths together with the respective vibrational level binding energies were published, as shown in table 5.1.

There are three issues about [76] which are not consistent:

- From the theoretical point of view, having similar triplet and singlet scattering lengths, but very different binding energies, is not possible, as C_6, which mainly determines

[1] By the use of the word 'sufficiently' it is implied that we can not make a quantitative statement, but in this case $|a| \gtrsim 10a_0$ might be a good estimate.

B_0^{exp} [G]	746.0 ± 0.4	759.6 ± 0.2	795.6 ± 0.2	—	—	—
$\mathrm{d}B/\mathrm{d}t$ [G/s]	15	0.3	10	—	—	—
B_0^{th} [G]	746.13	759.69	795.61	1096.68	1185.70	1766.13
Δ [G]	0.044	0.310	2.177	0.153	8.726	0.156

	scattering length a [a_0]	last bound state energy ε_ν^S [MHz]
singlet $S = 0$	15.9±0.3	-1.6±0.2
triplet $S = 1$	12.9±0.6	-5720±16

Table 5.1.: *Measured and predicted Feshbach resonance positions B_0^{exp}, B_0^{th} and widths Δ of* $\mathrm{Na}\,|1,1\rangle\,\mathrm{Li}\,|1/2,1/2\rangle$. *Singlet $S = 0$, triplet $S = 1$ scattering lengths and last bound state energies (from [76]). Ramp speed $\mathrm{d}B/\mathrm{d}t$ and B_0^{exp} have been taken from [75].*

a together with the binding energies, is the same for both singlet and triplet (the potentials show the same long-distance shape). Therefore, either one of the bound state energies ε_ν^S, the scattering lengths a or several of these parameters must be wrong.

- From our understanding of sodium intraspecies Feshbach resonances, the statement "We have also checked that there are no higher partial wave resonances" [76] is highly questionable. With s-wave resonances at similar fields as in the NaNa system and a similar rotational splitting, with the resonance assignment of Ref. [75] there *must* be higher partial wave resonances at magnetic fields below the already measured resonances.

- From the experimental point of view, we saw in chapter 4 that resonance widths Δ and inverse hold times to observe them stronly correlate (figure 4.6). Our inverse hold times are essentially the same as the ramp speeds $\mathrm{d}B/\mathrm{d}t$ in Ref. [75], so it is highly suspicious that these experimental values are in sharp contradiction to the width values of theory, as to be seen in table 5.1.

After all, more experimental measurements were needed to clear up those issues. In the following, we will therefore describe how we investigated the NaLi problem[2], starting from scattering length measurements, continuing with mapping out the Feshbach spectrum, which is finally explained using the ABM, while for the resonance widths a CC calculation completes the picture.

[2]We will not follow a historic order, but rather explain things such that they are presented in a logical, inductive way.

5.2. Scattering length determination

One result of the theoretical predictions which has to be experimentally confirmed is the value of the scattering length a. From the sucess of sympathetic cooling we know that $|a|$ should be sufficiently large, but using this kind of thermalization process to determine a quantitatively is not straightforward, both in experiment as in evaluation. Therefore, in the following we will analyze the damping of oscillations in the ODT to determine $|a|$ and get the sign of the scattering length from the comparison of suitable absorption images.

5.2.1. Absolute value of the scattering length

Let us first assume both the lithium and sodium sample as pointlike. When they are excited to oscillate in y-direction with their respective trap frequencies ω_y^{Li} and ω_y^{Na}, where $\omega_y^{\mathrm{Li}} > \omega_y^{\mathrm{Na}}$, a simple trigonometric argument shows that their ways cross with the rate $2\omega_y^{\mathrm{Li}}$. Next, want to determine the probability P of a scattering event in such a crossing of sodium and lithium. As sodium is in the majority, we consider the case of one lithium atom moving through a sodium background with density

$$n^{\mathrm{Na}}(x,y,z) = \eta \cdot n_c^{\mathrm{Na}}(x,y,z) + (1-\eta) \cdot n_{\mathrm{th}}^{\mathrm{Na}}(x,y,z) \tag{5.1}$$

composed of condensate n_c and thermal background n_{th}. The single lithium atom traveling along the y-direction can be described by a δ-distribution $n^{\mathrm{Li}}(x,y,z) = \delta(x-x_0)\delta(y)\delta(z-z_0)$. Thus the probability P that the lithium atom is scattered by the sodium cloud during one complete penetration along the y-direction reads

$$P = \sigma \int \mathrm{d}y \; n^{\mathrm{Na}}(x_0,y,z_0) = \sigma \int \mathrm{d}V \; n^{\mathrm{Na}}(x,y,z)\delta(x-x_0)\delta(z-z_0)\,, \tag{5.2}$$

where we introduced the interspecies scattering cross section $\sigma = 4\pi a^2$. Important for the scattering events with the condensed atoms to take place and thus our derivation to be valid is that the lithium atoms' velocity exceeds the superfluid critical velocity of the condensate $v_c \approx 1\,\mathrm{cm/s}$, which is well fulfilled for the following measurements.

To describe the experimental situation more accurately, we take into account the lithium atom cloud's spatial distribution, which we assume to be thermal[3]. Therefore it can be factorized as

$$n^{\mathrm{Li}}(x,y,z) = f(x)f(y)f(z). \tag{5.3}$$

Analog to eq. (5.2), the scattering probabilty can be written as

$$P = \sigma \int \mathrm{d}V \; n^{\mathrm{Na}}(x,y,z) \cdot f(x)f(z)\,. \tag{5.4}$$

[3]In reality, we have $T/T_F \lesssim 1$, but by comparing the density distributions we checked that at the temperatures of our experiment the difference between thermal and Fermi distribution is still negligible.

We see that eq. (5.4) is independent of the density distribution of lithium in y-direction $f(y)$, an approximation which is valid as long as the oscillation amplitudes are large enough such that after each crossing the clouds have completely penetrated each other. When a lithium atom scatters with a sodium atom, it does not oscillate in phase any more with the rest, i. e. it will on average end up at momentum $p = 0$ and does not contribute any more to the coherent oscillation signal. Thus, the lithium center of mass oscillation amplitude decreases with the time constant

$$1/\tau = 2\omega_y^{\mathrm{Li}} \cdot P = 2\omega_y^{\mathrm{Li}} \sigma \int \mathrm{d}V \; n^{\mathrm{Na}}(x, y, z) \cdot f(x) f(z) \,. \tag{5.5}$$

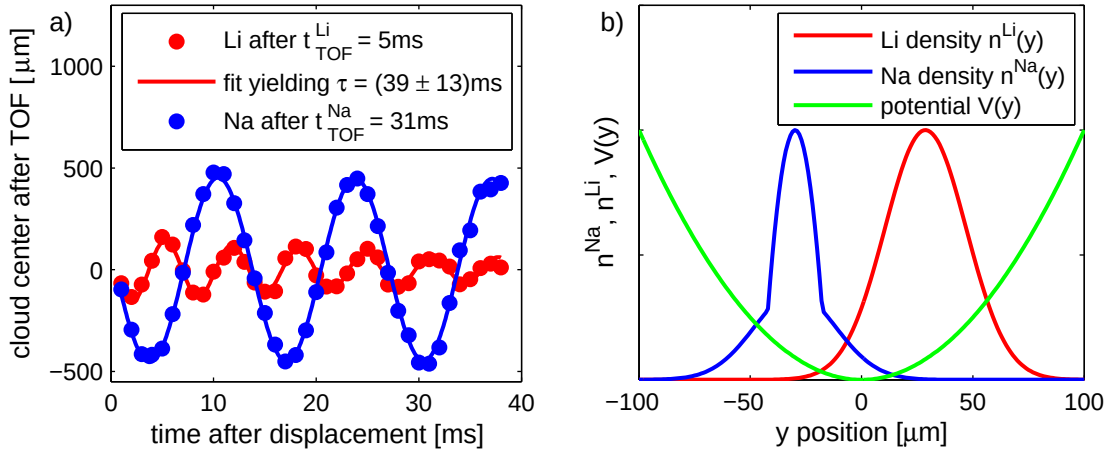

Figure 5.1.: ***a)*** *Simultaneous oscillation of* $\mathrm{Na}\,|2,2\rangle$ *(blue) and* $\mathrm{Li}\,|3/2,3/2\rangle$ *(red) along the y-direction of the ODT. The fits (solid lines) are exponentially decaying sine-functions yielding* $\omega_y^{\mathrm{Li}}/2\pi = (154.2 \pm 1.4)\,\mathrm{Hz}$ *and* $\omega_y^{\mathrm{Na}}/2\pi = (74.9 \pm 0.4)\,\mathrm{Hz}$. ***b)*** *Cut through the theoretically calculated cloud shapes for* $t \approx 7\,\mathrm{ms}$. *We see that the assumption of completely penetrating clouds is well justified for the high oscillation amplitudes reached by displacing the atoms with a magnetic gradient.*

Experimentally, we prepared sodium in $|2,2\rangle$ and lithium in $|3/2,3/2\rangle$, i. e. a pure triplet state, displaced them with the gradient of our finetune coils and let them oscillate. From the time-of flight pictures we can determine the damping of the lithium oscillation, which we get as $\tau = (39 \pm 13)\,\mathrm{ms}$ from the fit in figure 5.1. With the oscillation amplitudes in p-space, we can check if our picture of mutually penetrating clouds is correct. As to be seen in figure 5.1, where a cut through the theoretically calculated cloud shapes is plotted for $t \approx 7\,\mathrm{ms}$, our approximation is justified.

With $T = (225 \pm 15)\,\mathrm{nK}$, $N^{\mathrm{Na}} = (1.80 \pm 0.24) \cdot 10^5$ and a condensate fraction of $\eta = 0.4 \pm 0.1$, we get for the scattering probability per penetration $P = (7.9 \pm 0.7) 10^{13} \frac{\sigma}{\mathrm{m}^2}$. With $\omega_y^{\mathrm{Li}} = 2\pi \cdot 154\,\mathrm{Hz}$ from the fit, we finally get

$$|a_t| = (69 \pm 13) a_0 \,. \tag{5.6}$$

This result differs substantially from the one presented in [76], as will be further elucidated later. In chapter 8, we present a complementary measurement, yielding $|a_{BF}| = (70 \pm 12)a_0$ and thus confirming the value obtained here, but also giving us an absolute value only. Therefore, next we want to try and get a handle on the sign of the scattering length, which our oscillation damping measurement is not sensitive to.

5.2.2. Sign of the Scattering Length

As already discussed in section 3.4.1, the in situ distributions of trapped atoms can not be considered a reliable tool for quantitative data analysis, but nevertheless they can be used to extract information about the sign (though not the absolute value) of the scattering length. In chapter 2 we derived that a fermion immersed in a bath of bosons of density n_B experiences an additional mean-field-potential

$$\mu_F = \frac{\partial E}{\partial N_F} = \frac{2\pi\hbar^2}{\mu_{BF}} n_B a_{BF} \tag{5.7}$$

due to interactions. We see that for the case of repulsive (attractive) interspecies interactions $a_{BF} > 0$ ($a_{BF} < 0$), this potential is also repulsive (attractive). Thus when a lithium distribution with a sodium background is compared to a distribution of lithium without background, we expect the peak densities to be decreased (enhanced) by the mean-field potential of the condensate.

Experimentally, we prepare a bose-fermi mixture of sodium and lithium in our ODT and can – if required – remove the sodium selectively by a resonant light pulse provided by the same source which we use for absorption imaging. Before we can proceed with the image analysis, we have to check whether this removal has an unwanted effect on lithium, e. g. a heating of the cloud due to scattering with the expelled sodium atoms.

If exposed to resonant light, sodium atoms are excited at a rate of typically $\Gamma = 2\pi \cdot 10\,\mathrm{MHz}$. This means that their absorption process happens way faster than their photon-induced movement starts, a fact which is essential for absorption imaging to work properly: We usually image the atom density distribution such that the atoms do not have time to rearrange for the picture. The sodium atom has such a big recoil momentum from the absorbed photons that any collision with a lithium atom will lead to both atoms being lost from the trap due to momentum and energy conservation. With the numbers from the previous section, for a complete penetration of the two atomic clouds this happens with a probability $P = (7.9 \pm 0.7)10^{13}\frac{\sigma}{\mathrm{m}^2}$. Thus inserting the interaction cross section from eq. (5.6) we get $P \approx 1.4\%$. As we start from lithium and sodium being trapped in the same space, only about half a penetration takes place, i. e. the scattering probability per lithium atom is reduced to less than 1%. So we see that the sodium removal does not affect the lithium temperature, but only reduces its number by an amount which is way lower than our statistical uncertainty of $\sim 10\%$.

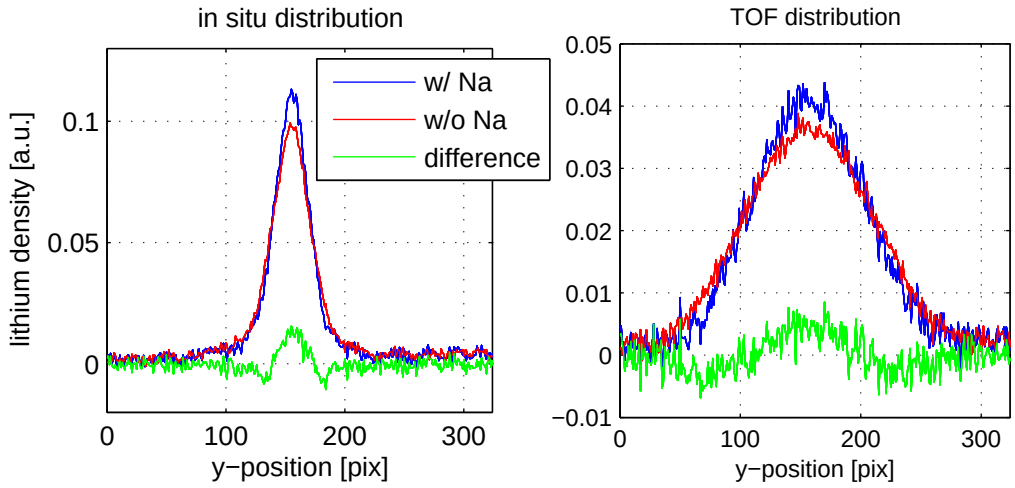

Figure 5.2.: *Lithium density distributions with (blue) and without (red) sodium background. Each distribution is an average over five shots, with every picture normalized to one. The lithium atom numbers* $N_{\mathrm{IS}}^{\mathrm{w/\ Na}} = (5.6 \pm 0.8) \cdot 10^4$ *and* $N_{\mathrm{IS}}^{\mathrm{w/o\ Na}} = (6.8 \pm 1.1) \cdot 10^4$ *for the in-situ profiles and* $N_{\mathrm{TOF}}^{\mathrm{w/\ Na}} = (7.0 \pm 1.6) \cdot 10^4$ *and* $N_{\mathrm{TOF}}^{\mathrm{w/o\ Na}} = (7.7 \pm 1.4) \cdot 10^4$ *for the time-of-flight measurements agree within their mutual error bars. The attractive interspecies interaction is obvious when the difference (green) is plotted. As the expansion is taking place with the sodium condensate still present, also in the respective TOF picture the lithium density distribution is more narrow than without background.*

In figure 5.2 we show lithium density distributions with and without sodium background, both for in situ and time-of-flight imaging. The mutual deviations are visible by eye and are getting even more pronounced when looking at the plotted difference of the distributions: The sodiums clearly drags atoms to the center, which are then missing in the wings. This clearly shows that $a_{BF} < 0$. In principle, one could also extract quantitative information from the TOF-pictures, but due to lithium having a temperature of $T/T_F < 1$ a correct description of the expansion is challenging as it is neither purely classical nor purely quantum and moreover the sodium background is also expanding during TOF in a non-trivial way. Therefore, we take the absolute value of a_t from the previous section to get

$$a_t = -(69 \pm 13) a_0 \,. \tag{5.8}$$

We thus see that a neither agrees with Ref. [76] in sign nor magnitude, which therefore raises high doubts about the – anyway partly incorrect – last bound state energy, which also determines the predicted Feshbach spectrum. To guide the further analysis, in particular of the Feshbach spectrum, an easy connection between a and the last bound state energy ε_ν^S is established in the following.

5.2.3. Last Bound State Energy from a

In the case of NaNa Feshbach resonances, where we only dealt with one hyperfine state, we had defined the bound state energy with respect to the free atom threshold, i. e. $\varepsilon_{\text{atoms}}(B = 0) \equiv 0$. In the following, we will use the ABM model to analyze Feshbach resonances measured in different hyperfine states which thus have different $\varepsilon_{\text{atoms}}(B = 0)$. Therefore, in the following the bound state energy ε_ν^S will be defined with respect to the atomic hyperfine multiplet barycenter, e. g. in $\text{Na}|1,1\rangle\text{Li}|1/2,1/2\rangle$ states with $\varepsilon_\nu^S > \varepsilon_{\text{atoms}}(B = 0) = -1.26\,\text{GHz}$ are not bound. This convention makes the different hyperfine state combinations easier comparable with each other.

With the values of a from the previous section and from chapter 6, the possible range of a covers $-82a_0$ to $-56a_0$. For the moment we do not make a difference between singlet and triplet scattering lengths a_s and a_t, as according to section 3.4.3 their values differ by less than the experimental uncertainty of a. With the additional knowledge of $C_6 = 1467(2)\text{a. u.}$ [77], one can calculate the last bound state energy $\varepsilon_\nu^S = -\hbar^2\kappa^2/(2\mu) + \varepsilon_{\text{atoms}}(B = 0)$, where μ denotes the reduced mass, as follows [78]. Introducing

$$\beta_6 = \sqrt[4]{\frac{2C_6\mu}{\hbar^2}} = 2R_{\text{vdW}} \tag{5.9}$$

as the characteristic length scale of the van-der-Waals potential, we can determine the scattering length a as

$$a = 0.480\beta_6\left(1 + \frac{1}{\tan(\pi F(\beta_6,\kappa))}\right), \tag{5.10}$$

where

$$F(\beta_6,\kappa) = \frac{\beta_6\kappa\left(0.443 - 0.0973\beta_6\kappa + 0.146(\beta_6\kappa)^{7/3} + (\beta_6\kappa)^3(-0.280 + 0.461(\beta_6\kappa)^{2/3})\right)}{2.91 + 2.24(\beta_6\kappa)^4}. \tag{5.11}$$

Our scattering length measurements thus set lower and upper limits of the bound state energy to -10.4 GHz< ε_ν^S <-9.7 GHz, respectively, differing completely from $\varepsilon_\nu^{S=1} = -5720\,\text{MHz}$ and $\varepsilon_\nu^{S=0} = -1.4\,\text{MHz}$ in Ref. [76]. Nevertheless, we will in the following first try to explain the measured Feshbach spectrum starting from latter values.

5.3. Feshbach Spectrum

In order to apply the ABM to describe the Feshbach spectrum of heteronuclear NaLi resonances, we proceed as already described in chapter 4. Instead of taking $|S, M_S, I, M_I\rangle$ as a base, we choose $|S, M_S, m_i^{\text{Na}}, m_i^{\text{Li}}\rangle$, which is more appropriate for distinguishable particles. Apart from that change, which makes calculations even slightly easier, all steps can be taken analog to the NaNa case.

S	1	1,0	1,0	1	1	1
M_S	-1	0	0	1	1	1
m_i^{Na}	3/2	3/2	1/2	3/2	1/2	-1/2
m_i^{Li}	1	0	1	-1	0	1

Table 5.2.: *List of $l = 0$ states for the vibrational singlet ($S = 0$) and triplet ($S = 1$) state with $M_F = m_f^{\mathrm{Na}} + m_f^{\mathrm{Li}} = 3/2$.*

To start with, we consider the channel $\mathrm{Na}|1,1\rangle\mathrm{Li}|1/2,1/2\rangle$, the only one for which NaLi Feshbach resonances had been known before our experiment started. To describe them within the framework of ABM, we first determine the spectrum of possible quantum numbers of molecular states $|S, M_S, m_i^{\mathrm{Na}}, m_i^{\mathrm{Li}}\rangle$ with $M_F = M_S + m_i^{\mathrm{Na}} + m_i^{\mathrm{Li}} = 3/2$, which can give rise to Feshbach resonances in that particular spin channel (table 5.2).

First, we try to reproduce the results of Ref. [76], a CC calculation, with the help of the ABM. Therefore, we do a least square fit to the theoretically predicted s-wave resonance positions, three of which had already been measured in experiment. This yields $\varepsilon_0^{S=0} = -4131.3\,\mathrm{MHz}$ and $\varepsilon_0^{S=1} = -5714.5\,\mathrm{MHz}$ for the singlet and triplet binding energies, respectively, latter being consistent with the result of Ref. [76]. The two new predicted res-

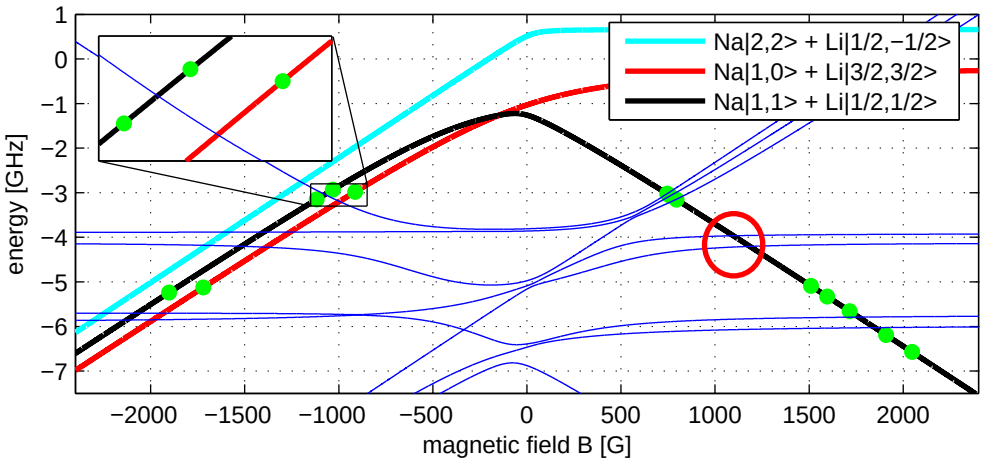

Figure 5.3.: *ABM representation of the Feshbach spectrum in the $M_F = 3/2$ channel, with the three measured resonances [75] (green circles) interpreted as s-waves [76]. The resulting binding energies are $\varepsilon_0^{S=0} = -4131.3\,MHz$ and $\varepsilon_0^{S=1} = -5714.5\,MHz$ for singlet and triplet, respectively. The free atom states are depicted as thick lines (see legend), the molecular $l = 0$ states as thin blue lines. In the region from $1\,kG$ to $1.3\,kG$, no resonances could be found (red circle). The inset shows the resonances in two different channels for $B = [-1150; -850]\,G$, the structure of which prevents an easy explanation of the Feshbach spectrum using s- and p-waves only.*

S	1	1	1	1	1	1	1,0	1,0	1,0	1,0	1,0	1,0	1,0
M_S	-1	-1	-1	-1	-1	-1	0	0	0	0	0	0	0
m_l	2	2	2	1	1	0	2	2	2	1	1	1	0
m_i^{Na}	3/2	1/2	-1/2	3/2	1/2	3/2	1/2	-1/2	-3/2	3/2	1/2	-1/2	3/2
m_i^{Li}	-1	0	1	0	1	1	-1	0	1	-1	0	1	0

S	1,0	1,0	1	1	1	1	1	1	1	1	1	1	1
M_S	0	0	1	1	1	1	1	1	1	1	1	1	1
m_l	0	-1	2	2	1	1	1	0	0	0	-1	-1	-2
m_i^{Na}	1/2	3/2	-1/2	-3/2	1/2	-1/2	-3/2	3/2	1/2	-1/2	3/2	1/2	3/2
m_i^{Li}	1	1	-1	0	-1	0	1	-1	0	1	0	1	1

Table 5.3.: *List of $l = 2$ states for the vibrational singlet (S=0) and triplet (S=1) state with $M_F = M_S + m_i^{\mathrm{Na}} + m_i^{\mathrm{Li}} + m_l = 3/2$.*

onances of singlet character, also depicted in figure 5.3, are predicted by ABM to be at 1097.3 G and 1185.3 G, respectively, also in excellent agreement with the CC predictions.

To locate the predicted resonances, we did Feshbach spectroscopy in a wide range around the predicted positions, but could not confirm any of them. On the contrary, we found a lot of unpredicted resonances depicted in figure 5.3. As to be seen in channel $\mathrm{Na}|1,1\rangle\mathrm{Li}|1/2,1/2\rangle$, their mere quantity already exceeds the number of possible s-waves. Taking additional p-waves into account is also not an option, as to be seen in the inset: This way, we could fit the two resonances in $\mathrm{Na}|1,1\rangle\mathrm{Li}|1/2,1/2\rangle$ with an s- and a p-wave, but this would leave the resonance in $\mathrm{Na}|1,0\rangle\mathrm{Li}|3/2,3/2\rangle$ unexplained. Taking additionally into account that the binding energies of $\sim -5\,\mathrm{GHz}$ assumed for such a scenario differ a lot from the $\sim -10\,\mathrm{GHz}$ obtained above from experimental data, we tried to do an assignment of the resonances using mostly d-waves.

Therefore, the number of possible states $|S, M_S, m_i^{\mathrm{Na}}, m_i^{\mathrm{Li}}\rangle$ is increased substantially, as the constraint now is $M_F = M_S + m_l + m_i^{\mathrm{Na}} + m_i^{\mathrm{Li}} = 3/2$ with $|m_l| \leq l = 2$. For $M_S = -1$, the number of possible states rises from one to six, and in total now we have 35 instead of 8 molecular states (see table 5.3).

5.4. Assignment and Fit of Resonances

The most important steps of the procedure to fit the measured Feshbach resonances, whose positions and experimental raw data are given in table 5.5 and Appendix B, can be summarized as follows:

- From the $l = 0$ state bound state energy estimate $-10.4\,\mathrm{GHz} < \varepsilon_0^S < -9.7\,\mathrm{GHz}$ we can exclude s-wave resonances at magnetic fields $B < 1.3\,\mathrm{kG}$. The only s-wave resonances

	$\varepsilon_0^{S=1}$ [GHz]	$\varepsilon_0^{S=0}$ [GHz]	$\varepsilon_2^{S=1}$ [GHz]	$\varepsilon_2^{S=0}$ [GHz]	η
ABM	-9.3521	-9.4505	-5.8509	-5.9493	0.9817
CC	-9.35335(50)	-9.3838(50)	-5.85180(30)	-5.95634(40)	—

Table 5.4.: *Triplet $S = 1$ and singlet $S = 0$ bound state energies obtained from ABM and CC. Note the excellent agreement in $\varepsilon_2^{S=1}$ and $\varepsilon_0^{S=1}$ as well as the good agreement in $\varepsilon_2^{S=0}$. Due to the positions of our Feshbach resonances not being sensitive on $\varepsilon_0^{S=0}$, this value differs most from the results obtained by the CC calculation.*

we can measure with our experimentally achievable magnetic fields have $M_S = \pm 1$, resonances from $M_S = 0$ molecular states could only appear around $B \approx 3\,\mathrm{kG}$.

- From the measurements of resonances in the $M_F = 5/2$ channel, which are not sensitive on the d-state singlet energy $\varepsilon_2^{S=0}$, we can deduce the d-state triplet energy $\varepsilon_2^{S=1}$. Here, the three resonances in the $M_F = -3/2$ channel already discussed above are helpful for an unambiguous assignment of the resonances, as figure 5.5 a) shows.

- Knowing that the singlet and triplet $l = 0$ bound state energies are roughly the same, we can also assume the same rotational splitting for both, as the related part of the potential is mainly given by C_6, which is the same for both singlet and triplet potential. Thus we can infer that with the s-wave bound state energies $\varepsilon_0^{S=1} \approx \varepsilon_0^{S=0}$, we also get for the d-wave energies $\varepsilon_2^{S=1} \approx \varepsilon_2^{S=0}$.

- With those assumptions, we first try and assign as many resonances as possible as d-waves and assume the rest, i. e. resonances which are more than $\sim$5 G off a crossing of molecular states and atomic threshold, as s-waves.

With our results almost not being sensitive on the singlet $l = 0$ bound state energy as pointed out above, instead of taking 3 fit parameters each for $l = 0$ and $l = 2$ states, we rather fit the d-state energies $\varepsilon_2^{S=0}$ and $\varepsilon_2^{S=1}$, a Franck-Condon factor η and the rotational splitting $\varepsilon_2^{S=1} - \varepsilon_0^{S=1}$. The results of our weighted least squares fit procedure are summarized and compared to the results of a CC calculation (see below) in tables 5.4 and 5.5. From our ABM analysis so far, the 3 resonances assigned s-waves could be p-waves as well, but the CC calculation using the full interaction potentials can determine the rotational splitting and thus confirms our assumption.

Figure 5.4 shows an overview of the resonance assignment for the different spin channels. Although they do not deliver information about the quality of the fit, these picture are important to get an impression of the overall molecular state and resonance structure. For $B = 0$, the molecular states show a splitting of 1.77 GHz, the sodium hyperfine splitting. If we zoom further in (see figure 5.5 b), we see that theses two branches show a splitting of 228 MHz, the lithium hyperfine splitting. By calculating the total molecular spin $\vec{f} = \vec{f}_{\mathrm{Na}} + \vec{f}_{\mathrm{Li}}$, we can also explain the substructure of the molecular levels visible in the zoom. Each state f

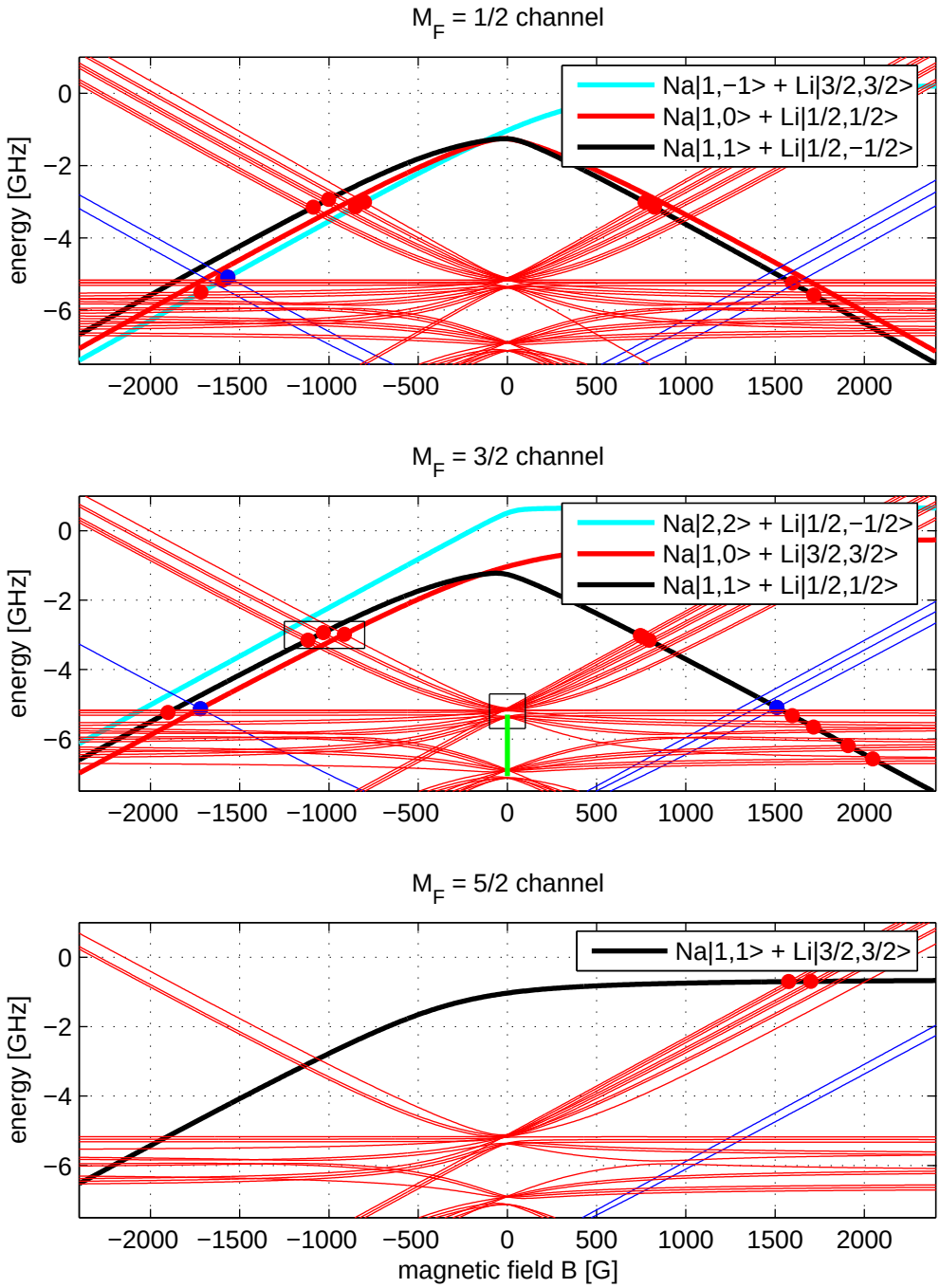

Figure 5.4.: *Near-threshold molecular spectra from ABM for different M_F, showing the molecular states $l = 0$ (blue) and $l = 2$ (red) states, and the observed s- and d-wave Feshbach resonances as blue and red dots, respectively. Atomic thresholds are depicted as thick lines and labeled in the legend. Zooms of the two boxes in the $M_F = 3/2$ figure are shown in figure 5.5. The horizontal green line depicts the sodium hyperfine splitting. A negative magnetic field corresponds to a sign change in M_F.*

has several Zeeman sublevels $|m_f| \leq f$, which are for a certain spin channel M_F only shown if $M_F = m_f + m_l$ can be fulfilled (see table 5.3).

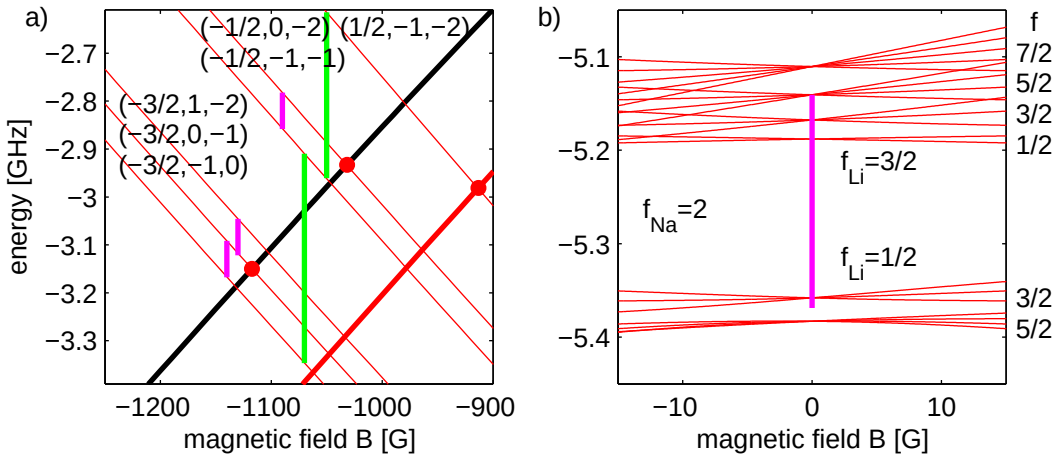

Figure 5.5.: *Zooms of the $M_F = 3/2$ state of figure 5.4.* **a)** *The molecular states (red lines), which all have $M_S = 1$, are labeled with their quantum numbers $(m_i^{\mathrm{Na}}, m_i^{\mathrm{Li}}, m_l)$. The green horizontal lines show the splitting due to different $m_{i,\mathrm{Na}}$ as obtained from the Breit-Rabi formula, the magenta horizontal lines have a length of $a_{\mathrm{hfs}}^{\mathrm{Li}}/2$.* **b)** *For small B, the molecular states can be characterized by their quantum numbers f and m_f. The horizontal magenta line depicts the lithium hyperfine splitting.*

5.4.1. Quantum Numbers

The zoom in figure 5.5 shows how the resonances in the $M_F = 3/2$ channel, which could not be explained in an s-wave scenario, naturally arise from the $l = 2$ molecular states. We can also extract important information about the structure of the resonances: As also to be seen in figure 5.4, the molecular states for a certain total electron spin projection M_S have a coarse structure given by states with a sodium nuclear spin $m_i^{\mathrm{Na}} \in \{-3/2, -1/2, 1/2, 3/2\}$. The offset between those states can be easily calculated by the Breit-Rabi formula. Each line bundle with a certain m_i^{Na} consists of up to three states with different lithium nuclear spin $m_i^{\mathrm{Li}} \in \{-1, 0, 1\}$, whose mutual offset is $a_{\mathrm{hfs}}^{\mathrm{Li}}/2$, as we are far in the Paschen-Back regime of the atomic hyperfine structure.

With this explanation in mind, it is straighforward to extract the quantum numbers of the molecular states with $M_S = \pm 1$ causing Feshbach resonances. For the $M_S = 0$ states, which can not be assigned $S = 0$ or $S = 1$ due to the strong mixing of singlet and triplet, more care has to be taken: By tracing back the molecular state from the resonance position B_0 to $B = 0$, we can determine the quantum numbers f and m_f and thus $m_l = M_F - m_f$ from a picture like figure 5.5. Being in an $M_S = 0$ state, we have $m_f = m_f^{\mathrm{Na}} + m_f^{\mathrm{Li}} = m_i^{\mathrm{Na}} + m_i^{\mathrm{Li}}$,

where m_i^{Na} and m_i^{Li} can be determined by tracing the molecular state in ABM representation to $B \to \infty$: There the different molecular states separate in bundles characterized by m_i^{Na}, as to be seen in figure 5.4.

5.4.2. Triple Features

When examining the resonance positions in table 5.5, one will notice that around 1596 G and 1717 G, there are three resonances at almost equal magnetic fields characterized by similar quantum numbers. More precisely, the resonances show up in the $M_F = 3/2$, $M_F = 1/2$ and $M_F = -1/2$ states when prepared in Na$|1,1\rangle$ and Li$|1/2,1/2\rangle$, $|1/2,-1/2\rangle$ and $|3/2,-3/2\rangle$, respectively. Figure 5.6, where also the three resonances around 1717 G are depicted in one graph, shows how such a triple feature arises: Three molecular lines characterized by their quantum numbers $M_S = 0$, m_i^{Na}, m_l and $m_i^{\mathrm{Li}} = 0, \pm 1$ each lead to a resonance when crossing the atomic threshold characterized by $m_i^{\mathrm{Li}} = 0, \pm 1$.

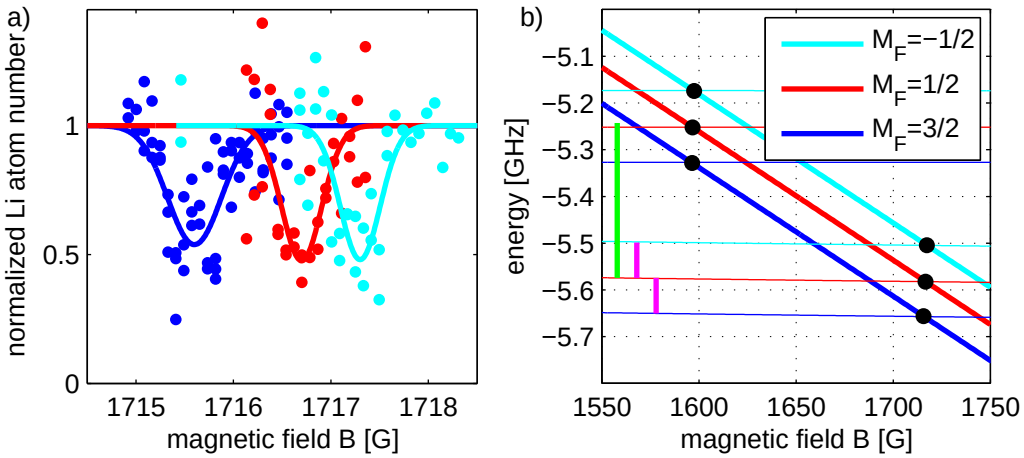

Figure 5.6.: *Triple feature in the NaLi resonance spectrum.* ***a)*** *The three 1717 G resonances in three different spin channels shown in one graph.* ***b)*** *The resonances (black dots) and the respective molecular and atomic states (thin horizontal and thick diagonal lines, respectively). The atomic spin states are* Na$|1,1\rangle$ *and* Li$|1/2,1/2\rangle$ *($M_F = 3/2$),* $|1/2,-1/2\rangle$ *($M_F = 1/2$) and* $|3/2,-3/2\rangle$ *($M_F = -1/2$). The green horizontal line shows the splitting due to different* $m_i^{\mathrm{Na}} = 3/2, 1/2$ *as obtained from the Breit-Rabi formula, the magenta horizontal lines have a length of* $a_{\mathrm{hfs}}^{\mathrm{Li}}/2$ *and show the splitting between* $m_i^{\mathrm{Li}} = 0, \pm 1$.

The energetic difference between the three different hyperfine states in the Paschen-Back regime is $a_{\mathrm{hfs}}^{\mathrm{Li}}/2$, as depicted in the figure, which is the explanation for each single triple feature. Even the difference in energy and thus magnetic field position of the resonances can be understood: By recognizing that the 1596 G triple has $m_i^{\mathrm{Na}} = 3/2$, whereas the 1717 G triple has $m_i^{\mathrm{Na}} = 1/2$, we can easily calculate the energy difference via the Breit-

Rabi formula and with the slope of the atomic threshold of $\sim 2.8\,\mathrm{MHz/G}$ the difference in resonance positions.

As one would suppose, due to their high similarity in quantum numbers, all three 1596 G and 1717 G resonances show similar widths of 5 mG and 0.3 mG, respectively, which have been obtained by a CC calculation (see table 5.5). Furthermore by looking at the m_l quantum number, one sees that the observation of one triple feature might be explained in an s-wave scenario ($m_l = 0$), whereas seing a second triplet nearby is a clear hint that higher partial waves, i. e. d- or even g-waves ($m_l > 0$ possible), have to be involved in the explanation of the spectrum.

5.4.3. Resonance Widths

The resonance widths shown in table 5.5, which were obtained by a CC calculation, are all very small. To be quantitative, one can determine their resonance strengths s_{res} eq. (3.21) and sees that all resonances are weaker than $s_{\mathrm{res}} = 4 \cdot 10^{-4}$. This is due to a combination of factors: First, the singlet and triplet interaction potentials are far from being resonant, indicated by their scattering lengths which are of the same order as the van der Waals length eq. (2.2) $R_{\mathrm{vdW}} \approx 35 a_0$. Second, the effective coupling between singlet and triplet states is very small, indicated by $|a_s - a_t| \ll R_{\mathrm{vdW}}$. A similar situation can be found in homonuclear ^{87}Rb [79], where the narrowness of the Feshbach resonances and the smallness of the loss rates can be traced back to non-resonant and similar values of a_s and a_t [80]. The resulting long lifetimes of the mixture in all spin channels are an advantage over e. g. the Na^{40}K mixture. There, one has resonances nicely suited for tuning [81], but due to the large difference of singlet and triplet scattering length $|a_s - a_t| \approx 900 a_0$ [82] thermalization measurements with long timescales involved are only possible in selected spin state combinations.

Due to the small resonance widths $\Delta \leq 10\,\mathrm{mG}$ in combination with magnetic field fluctuations $\delta B \gg 10\,\mathrm{mG}$, the fitted loss feature width ΔB (see figure appendix B) is not a good experimental measure of the resonance width Δ. To be able to compare different resonances systematically, we took for each resonance a loss curve with a fixed magnetic field sweep range of $\sim 1\,\mathrm{G}$, an example of which is shown in figure 5.7 a). From an exponential fit, we get the hold time τ, whose inverse shows correlations to the calculated resonances width. The scatter though is far too high for a meaningful quantitative analysis.

The complete results of ABM fitting procedure, CC calculation and quantum number assignment are summarized in table 5.5. The fact that almost all resonances are fitted with less than 1 G deviation by only four ABM fit parameters is strongly supporting our scenario. The exceptions can be explained by the CC calculation: It shows that the resonances in the $M_F = 5/2$ channel have a high inelastic loss rate to lower lying atomar channels, so as we learned in section 3.3.4 their experimentally measured position of maximum loss might thus not be coincident with the resonance position.

The resonances at 800.9 G and 1700.4 G were measured *after* our model was made, which proves its accuracy and predictive power. The fact that the ABM yields way more resonances

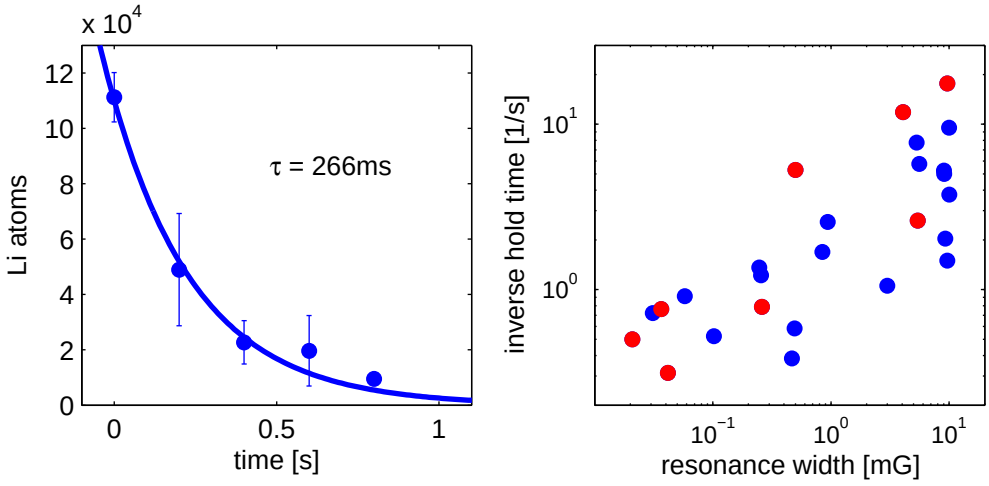

Figure 5.7.: *Left: Example of a loss curve with fixed magnetic field sweep range (800.9 G resonance). Right: Fitted inverse hold time vs. resonance width from CC calculation. The red dots, which are resonances from the lowest energetic atomic channel* $\mathrm{Na}\,|1,1\rangle\,\mathrm{Li}\,|1/2,1/2\rangle$*, show slightly less scatter and a better correlation.*

than we observed (see figure 5.4) is explained by the coupled channels calculation: Compared to the observed resonances, the width of the ones not found is simply too narrow to be detected by our apparatus.

The CC calculation yields for the scattering lengths $a_s = -73(8)a_0$ and $a_t = -76(5)a_0$, which shows in sign, magnitude and mutual difference excellent agreement with the experimental values obtained above.

5.5. Concluding Remarks

With the chapter about NaNa resonances in mind, one might ask why it was so much more difficult to explain the NaLi spectrum. First, much more data was known for NaNa from molecular spectroscopy, whereas the NaLi data has just recently been obtained [83]. Moreover, the early sodium BEC experiments started in 1995 were relying on the fact $a_{\mathrm{NaNa}} > 0$, otherwise condensates would have been unstable [84, 85]. Thus, the sign of the scattering length was known and the magnitude had to be consistent with the measured speed of sound $c \propto \sqrt{an}$ [86, 87], which pins down the molecular bound state energies quite well.

In contrast, in the case of NaLi there was only knowledge about good thermalization with sodium [42, 43], but not even the sign was assumed correctly (Ref. [30] in [76]). That together with only three measured resonances, which were interpreted as s-waves [75], was forming an almost consistent picture [76]. This is the reason why it took us so long to see the need of determining the scattering length a experimentally and completely changing our scenario

from s- to d-waves.

Although none of the resonances found is suitable for tuning due to their low widths, there is still possibilities to get an α big enough to observe polaronic behaviour in our experiments: According to our findings, a_{IB} is a factor of 5 bigger than assumed before, thus we got a factor of 25 increase in α 'for free'. With typical sodium numbers, we now have $\alpha \approx 0.02$, which would result in an increase in the effective mass of lithium by 0.7%. The tunability could then be achieved by changing a_{NaNa} using the Feshbach resonance at 1202.6 G which has been described in detail in chapter 4. At an experimentally feasible magnetic field stability of 50 mG, tuning could reach $\alpha \approx 0.028$ and thus a 10% increase in effective mass. A possible problem of this approach is the disappearance of Boguliubov modes for $a_{\mathrm{NaNa}} \to 0$, which are essential for the theoretical explanation of the polaron [21]. Thus another option is outlined in our paper [88], where the CC calculation yields widths suitable for tuning the interaction of ^{7}Li+Na, a mixture our apparatus could cool and trap after some changes in the laser setup.

^{6}Li+Na	Exp.	ABM	Coupled-Channels		Quantum Numbers				
M_F	B_0^{exp}(G)	$\delta B_0^{\mathrm{ABM}}$(G)	δB_0^{CC}(G)	Δ(mG)	M_S	m_i^{Na}	m_i^{Li}	l	m_l
$\|2\rangle+\|1\rangle$	771.8(5)	-0.7	-0.190	10	1	3/2	0	2	-2
1/2	822.9(5)	0.5	0.050	0.5	1	1/2	0	2	-1
	1596.8(4)	0.2	-0.314	5	0	3/2	0	2	-1
	1716.7(3)	0.0	0.231	0.2	0	1/2	0	2	0
$\|1\rangle+\|3\rangle$	1002.3(5)	-0.6	-0.209	9	1	-1/2	1	2	-2
$-1/2$	1088.5(5)	0.2	-0.301	0.9	1	-3/2	1	2	-1
$\|3\rangle+\|1\rangle$	800.9(2)	-0.4	0.096	10	1	3/2	-1	2	-2
$-1/2$	852.0(7)	0.2	-0.271	0.5	1	1/2	-1	2	-1
	1566.3(8)	0.1	0.023	0.03	1	-1/2	-1	0	0
	1597.5(7)	0.4	-0.144	6	0	3/2	-1	2	-1
	1717.3(2)	-0.2	0.038	0.3	0	1/2	-1	2	0
$\|1\rangle+\|1\rangle$	745.2(3)	-0.3	0.175	10	1	3/2	1	2	-2
3/2	759.0(3)	0.5	0.022	0.02	1	3/2	0	2	-1
	795.2(2)	0.5	-0.020	0.5	1	1/2	1	2	-1
	1510.4(3)	0.0	-0.024	0.04	1	-1/2	1	0	0
	1596.5(5)	0.5	0.009	5	0	3/2	1	2	-1
	1715.6(8)	-0.3	0.034	0.3	0	1/2	1	2	0
	1908.9(7)	0.4	-0.350	0.04	0	1/2	1	2	0
	2046.9(9)	0.5	-0.608	4	0	3/2	1	2	-1
$\|2\rangle+\|3\rangle$	1031.7(3)	-0.3	0.166	9	1	-1/2	0	2	-2
$-3/2$	1117.3(6)	0.0	-0.511	0.8	1	-3/2	0	2	-1
	1902.4(6)	-0.3	-0.045	0.1	0	-3/2	0	2	0
$\|3\rangle+\|2\rangle$	913.2(6)	-0.3	0.108	9	1	1/2	-1	2	-2
$-3/2$	**1720.5(3)**	0.0	-0.103	0.06	1	-3/2	-1	0	0
$\|6\rangle+\|1\rangle$	1575.8(9)	0.9	-0.014	—	1	3/2	1	2	-1
5/2	1700.4(7)	1.5	-0.040	—	1	1/2	1	2	0

Table 5.5.: *Overview of the experimentally and theoretically obtained results on Feshbach resonances, sorted by spin state and corresponding quantum number $|M_F|$. In column "Exp." the position of maximum loss B_0^{exp} is reported, which is determined by Gaussian fits to the loss features (s-waves in bold). As error we give the rms width of the RF calibration signal. The other columns show the Feshbach resonance positions from the ABM fit, and the positions and widths Δ from coupled-channels calculation. The theoretical positions are given by their deviation from the experimental value, i. e. $\delta B_0^{\mathrm{ABM}} \equiv B_0^{\mathrm{exp}} - B_0^{\mathrm{ABM}}$ and $\delta B_0^{\mathrm{CC}} \equiv B_0^{\mathrm{exp}} - B_0^{\mathrm{CC}}$. For the two resonances of asymptote $|6\rangle+|1\rangle$ no widths are given (see text). The assignment of each resonance in terms of the molecular quantum numbers $|M_S, m_i^{\mathrm{Na}}, m_i^{\mathrm{Li}}, l, m_l\rangle$ with $m_i^{\mathrm{Na}} + m_i^{\mathrm{Li}} + m_l = M_F$ is given in the last column. The spin quantum number S takes the value $S = 1$ if $M_S = 1$ and cannot be assigned for $M_S = 0$ due to the strong mixing of singlet and triplet.*

Part II.

Bose-Fermi Mixtures in Periodic Potentials

In the second part of this thesis, we investigate atoms in a species selective optical lattice. In order to be able to create one- and two-dimensional Fermi gases, we derive design criteria, which we use to determine the parameters of the optical lattice. Starting with an analytic harmonic oscillator approximation, we subsequently extend our calculations to describe the full periodic potential using Bloch states. With that knowledge at hand, we are able to explain the experimentally demonstrated phase lattice for sodium and the oscillations of lithium.

As a tool to analyze the momentum distribution of atoms in the lattice, we implement the technique of Brillouin zone mapping. As a first application, we use it to improve the loading process of the lattice by having a sodium background present. In the following, we further investigate the interspecies energy transfer from oscillating lithium to condensed sodium atoms.

By applying a periodic shaking of the lattice, we are able to do a controlled transfer of lithium atoms from first to second Bloch band. The subsequent relaxation in presence of a sodium background is used to estimate the absolute value of the interspecies scattering lenght a_{IB}. Finally, we demonstrate and analyze a Rabi oscillation of lithium atoms in the two-level system formed by the two lowest Bloch bands.

6. Design and Implementation of the Optical Lattice

With our goal to engineer polarons in ultracold atom systems in mind [21], we have to think about an appropriate experimental realization. As discussed in the first part of this thesis, the tuneability parameters a_{IB} and a_{BB} are now well studied, such that we know how to adjust α. A parameter characterizing the polaron is its effective mass, which scales in the weakly interacting regime as $m^* = m \cdot (1 + 0.3637\alpha)$ [89]. As it is easy to measure masses experimentally, e. g. via frequencies $\omega \propto 1/\sqrt{m}$ [17], we want to design a potential in which we can selectively excite oscillations of the lithium and map out their dependence on α.

The tool of choice for reaching that goal is the use of a species selective optical dipole trap (SSODT) [90]. As we will show in the following, by tuning the laser, which creates the SSODT, in close vicinity to the lithium transition, we obtain a trapping potential for lithium only while the impact on sodium is negligible. This way, we can not only excite oscillations of the lithium, but also drag it through the sodium background, which gives the possibility to map out the superfuid critical velocity. Similar experiments have been conducted using a blue detuned laser beam [91] and sodium atoms in different hyperfine states [92] for bosonic condensates and a moving optical lattice for a superfluid Fermi gas [93]. Due to the precise spatial control provided by dipole traps, lithium can this way even be used as a local probe for condensate properties, an aim which is currently being pursued by experiments moving ions through BECs [94].

There are numerous possibilities for the overall form of the SSODT potential: One could cover the issues mentioned above using e. g. a single focused laser beam. We decided to give our system more versatility by implementing the SSODT as a two-dimensional optical lattice potential[1], such that we can form a stack of lithium pancakes each containing a two-dimensional Fermi gas or even get an array of one-dimensional tubes. The interesting aspect about lowering the dimensionality is that for interacting particles we get easily into the strongly interacting regime, where $E_{int}/E_{kin} \gg 1$. Thus, fermion pairing in two-dimensional systems [95] and its evolution when dimensionality is increased to three [96] are objects of current research.

[1] At the time this thesis was written, only one axis had been implemented experimentally.

6.1. Design of the SSODT

6.1.1. Dimensionality criteria

Before starting with the design of the SSODT, we want to develop the criteria for a system to be considered one- or two-dimensional. Therefore, we recall the Fermi energy of N harmonically trapped atoms

$$E_F^{1\mathrm{d}} = N\omega_{||} \tag{6.1}$$

in one dimension and

$$E_F^{2\mathrm{d}} = \sqrt{2N} \cdot \omega_{||} \tag{6.2}$$

in two dimensions, respectively. The dimension in which the atoms are allowed to move is characterized by the frequency $\omega_{||}$, whereas the transversal direction in which motion shall be frozen out, has frequency $\omega_\perp \gg \omega_{||}$. For the gas to allow for a theoretical lower-dimensional treatment, we have to fulfil the following criteria:

- $E_F = \mu(T = 0) \ll \hbar\omega_\perp$: A new particle added must not occupy a transversally excited state. For N fermions in a lattice well, this reads $N \cdot \omega_{||} \ll \omega_\perp$ for one-dimensional and $\sqrt{2N} \cdot \omega_{||} \ll \omega_\perp$ for two-dimensional systems.
- $k_B T \ll \hbar\omega_\perp$: Temperature has to be so low that particles are not thermally excited to higher transversal states.
- $J \ll \mu$: In the case of an optical lattice, the tunneling energy J must be smaller than the chemical potential μ to suppress hopping of atoms between the different lattice sites [97].

Experimentally, we typically have $N_{\mathrm{Li}} = 10^5$ lithium atoms at a temperature of $T = 0.2\,\mu$K. Thus, temperature imposes an $\omega_\perp/2\pi \gg 4\,$kHz, while for the two-dimensional case with at most $N \approx 700$ atoms in the central sheet[2] we get from the chemical potential $\omega_\perp/2\pi \gg 8.4\,$kHz, where we assumed $\omega_{||}/2\pi = 224\,$Hz as the geometric mean of the ODT frequencies in y- and z-direction. Similarly, the tunneling condition yields $J/2\pi \ll 6\,$kHz.

In the following, we will derive some analytical formulas which will prove useful in the succesive lattice design.

6.1.2. Fundamentals of Optical Lattices

Optical Dipole Forces

In the field of ultracold quantum gases, a common way to design potentials for the atoms is to make use of the dipole force. In short, an atom with transition frequency ω_0 and decay

[2] This maximal value is reached for loading a $T = 0$ degenerate Fermi gas into a lattice formed by a $\lambda \approx 670\,$nm retroreflected laser beam.

rate Γ feels due to its polarizability the dipole potential

$$V_{dip}(\vec{r}) = \frac{3\pi c^2}{2\omega_0^3}\left(\frac{\Gamma}{\omega-\omega_0}+\frac{\Gamma}{\omega+\omega_0}\right) I(\vec{r}) \approx \frac{3\pi c^2}{2\omega_0^3}\left(\frac{\Gamma}{\Delta}\right) I(\vec{r}) \tag{6.3}$$

when exposed to a light field with intensity $I(\vec{r})$ oscillating at frequency ω [98]. The rotating wave approximation on the right hand side is valid for detunings $|\Delta| = |\omega - \omega_0| \ll \omega_0$. Spontaneous processes lead to a scattering rate

$$\Gamma_{sc}(\vec{r}) = \frac{3\pi c^2}{2\hbar\omega_0^3}\left(\frac{\omega}{\omega_0}\right)^3\left(\frac{\Gamma}{\omega-\omega_0}+\frac{\Gamma}{\omega+\omega_0}\right)^2 I(\vec{r}) \approx \frac{3\pi c^2}{2\hbar\omega_0^3}\left(\frac{\Gamma}{\Delta}\right)^2 I(\vec{r})\,. \tag{6.4}$$

Comparing eqs. (6.3) and (6.4), we see that $\Gamma_{sc}/V_{dip} \propto 1/\Delta$, i. e. choosing a large detuning helps us to reduce the scattering and thus heating of the atom sample. We further see that the dipole potential is attractive for red detuning $\Delta < 0$ and repulsive for blue detuning $\Delta > 0$. In latter case, the atoms are trapped in an intensity minimum, which minimizes the spontaneous scattering rate.[3]

As we want to have a species-selective lattice for lithium, we have to minimize its influence on sodium, i. e. keep the lattice depth lower than the chemical potential $V_{\mathrm{Na}} \ll \mu \approx 100\,\mathrm{nK}$. As we can already anticipate, the lattice wavelength will have to be close to the lithium D_2 transition $\lambda = 670.977\,\mathrm{nm}$, translating into $I \ll 2\cdot 10^5\,\mathrm{W/m^2}$. If a detuning $\Delta \approx 1\,\mathrm{nm}$ is chosen, the resulting lithium scattering rate in this light field is $\Gamma_{Sc} \approx 3/\mathrm{s}$, a value which would limit possible experiments to a duration on the order of $\sim 100\,\mathrm{ms}$.

Optical Lattices

A common way to create an optical lattice is to retroreflect a beam of wavelength λ and thus get a standing wave potential with periodicity $\lambda/2$,

$$V(x) = V_0 \sin^2\left(2\pi\frac{x}{\lambda}\right) = \frac{V_0}{2}\left(1-\cos\left(2\pi\frac{x}{\lambda/2}\right)\right), \tag{6.5}$$

where we get a lattice depth V_0 by interfering a single beam of potential of depth $V_0/4$ with its retroreflection. Approximating each lattice well as a harmonic oscillator $V(x) = \frac{1}{2}m\omega^2x^2$, we get from a taylor expansion of eq. (6.5)

$$\omega = \frac{2\pi}{\lambda}\sqrt{\frac{2V_0}{m}}\,. \tag{6.6}$$

It is convenient to introduce the lattice recoil energy $E_r = \frac{\hbar^2k^2}{2m}$ with the lattice wavevector $k = 2\pi/\lambda$, which describes the kinetic energy gain of a lithium atom when absorbing a

[3] Scattering can never be completely turned off due to the atom always having a thermal or quantum mechanical distribution with finite spatial width Δx, i. e. there will always be some light scattering.

photon from a lattice beam. Introducing $V_0 = sE_r$ we can express ω conveniently as

$$\omega = \frac{2E_r}{\hbar}\sqrt{s}\,. \tag{6.7}$$

With the intensity and detuning values from above, we get $V_0 \approx 2.6E_r$ with $E_r = 3.5\,\mu\text{K}= 73\,\text{kHz}$ for lithium and thus $\omega/2\pi \approx 235\,\text{kHz}$, which fulfils the frequency conditions for reaching lower dimensionality $\omega_\perp/2\pi \gg 8.4\,\text{kHz}$ easily.

So far, we were reducing our considerations to one lattice site only. Having several lattice sites, their connection can be discribed by a tunneling matrix element J, which can for $s \gg 1$ be approximated as [99]

$$J = \frac{4}{\sqrt{\pi}}\,(V_0/E_r)^{3/4}\,e^{-2\sqrt{V_0/E_r}}E_r = \frac{4}{\sqrt{\pi}}\,(s)^{3/4}\,e^{-2\sqrt{s}}E_r\,. \tag{6.8}$$

For $s = 2.6$, we get $J/2\pi \approx 14\,\text{kHz}$, i. e. it clearly violates the condition for no tunneling $J/2\pi \ll 6\,\text{kHz}$. A way this can be understood intuitively is that lithium can due to its light mass easily hop over the barrier between one lattice well and the next. A way to circumvent this is thus to make the lattice spacing larger, which can formally be seen as increasing λ and thus decreasing E_r. Due to the exponential scaling of J with $-1/\sqrt{E_r} \propto -\lambda$, we decrease the tunneling energy this way.

Experimentally, instead of creating the lattice by a retroreflected beam, we let two beams interfere under an angle 2α as shown in figure 6.1 and thus effectively change the wavelength $\lambda \to \lambda/\sin(\alpha)$. Due to space limitations, we choose $2\alpha = 35°$, which results in a effective $\lambda = 2.2\,\mu\text{m}$ or a lattice spacing of $\lambda/2 = 1.1\,\mu\text{m}$, respectively. The formulas derived above stay valid, with E_r now being calculated with the new λ, i. e. it decreases by about one order of magnitude to $E_r = 6.9\,\text{kHz}$.

The absolute lattice depth V_0 does not change, but due to $s = V_0/E_r$ we get $s = 28$ and thus for the tunneling coupling $J/2\pi = 50\,\text{Hz}$ at a vibrational frequency of $\omega/2\pi = 70\,\text{kHz}$, i. e. our conditions for reaching lower dimensionality are well fulfilled. With the lithium atoms being in the harmonic oscillator ground state, they scatter light at a rate $\Gamma_{sc} \approx 1/\text{s}$ from the blue detuned light sheets.[4] In figure 6.1 b) we can see how according to eq. (6.4) the scattering rate increases when the lattice depth is varied at constant power by changing the detuning.

[4]For a red detuned SSODT, the overlap integral with the lattice light would be about a factor of 10 higher, which increases the scattering rate by the same factor. Additionally to the advantage of the lower scattering rate, using a blue detuning drastically reduces the overall harmonic confinement induced by the gaussian shape of the lattice beams compared to the red detuned configuration [101].

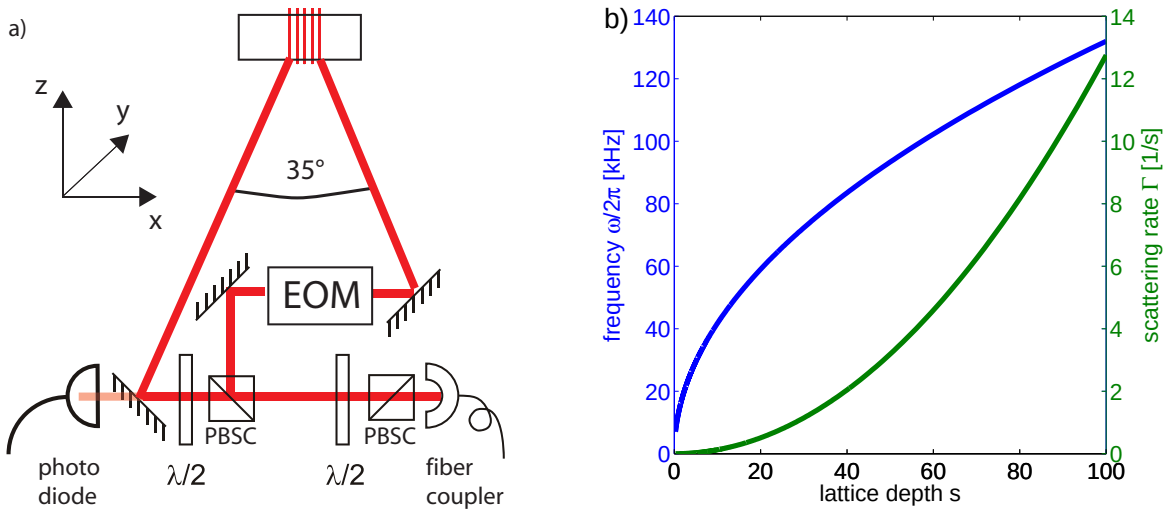

Figure 6.1.: ***a)*** *Experimental setup to create the optical lattice potential. For technical details, see Ref. [100].* ***b)*** *Oscillation frequency ω (blue line) and spontaneous scattering rate Γ_{sc} (red line) of lithium atoms in the blue detuned optical lattice in dependence of its depth s, latter being tuned by changing the detuning Δ. The fixed light intensity chosen here is such that the impact on sodium is kept sufficiently low, as described in the text.*

Inhomogeneity

So far, we have not taken the beam shape into account: The SSODT is formed by Gaussian beams, which are mathematically described by the intensity profile

$$I(x,y,z) = I_0 \left(\frac{w_0}{w(z)}\right)^2 \exp\left(-\frac{2(x^2+y^2)}{w^2(z)}\right) \tag{6.9}$$

for a beam propagating in z-direction. $w(z) = w_0\sqrt{1+(z/z_R)^2}$ is the waist, which takes the value w_0 at the beam focus and $z_R = \pi w_0^2/\lambda$ is called Rayleigh range. Normalization determines $I_0 = 2P_0/(\pi w_0^2)$ with P_0 being the total beam power.

In our experimental setup, the lattice beam has a waist of $w_0 \approx 400\,\mu$m at the fiber outcoupler, which expands on its way to the glas cell to $w \approx 550\,\mu$m, i. e. we can neglect the z-dependence of the intensity profile. Thus, two beams interfering under an angle 2α as shown in figure 6.1 a) have the overall intensity envelope

$$I(x,y,z) \propto \exp\left(-\frac{2(y^2+(x\cos(\alpha))^2+(z\sin(\alpha))^2)}{w^2}\right). \tag{6.10}$$

Plugging this result for intensity and thus potential depth V_0 into the formula for ω eq. (6.6), we see after a Taylor expansion that we get a frequency with spatial dependence

$$\omega(x,y,z) = \omega_0\left(1-\frac{y^2}{w^2}-\frac{(x\cos(\alpha))^2}{w^2}-\frac{(z\sin(\alpha))^2}{w^2}\right). \tag{6.11}$$

For an estimate of the anharmonicity $\Delta\omega$ experienced by the atoms, we can plug in the radii $(R_x, R_y, R_z) = (48, 46, 25)\,\mu$m of the $T = 0$ Fermi distribution and get

$$(\Delta\omega_x, \Delta\omega_y, \Delta\omega_z) = (7 \cdot 10^{-3}, 7 \cdot 10^{-3}, 2 \cdot 10^{-4})\omega_0 \tag{6.12}$$

We see that we can expect to observe about 50 oscillations until the atoms in the center are out of phase by π from the atoms at the cloud edge. This dephasing is independent of the value of the lattice depth s, in contrast to the dephasing due to the finite bandwith J, as we will see later.

Spatial Configuration and Implications for Polaron Experiments

At this point, we can develop a picture of our experimental situation: As to be seen in figure 6.2, lithium occupies about 80 lattice sites, the number being simply determined by the size of lithium density distribution of radius $R_x \approx 45\,\mu$m in the ODT. As we see in the figure and know from eq. (3.27), the sodium condensate has a Thomas-Fermi Radius of $R_{TF} \approx 13\,\mu$m and thus only partly overlaps with the lithium in the lattice.

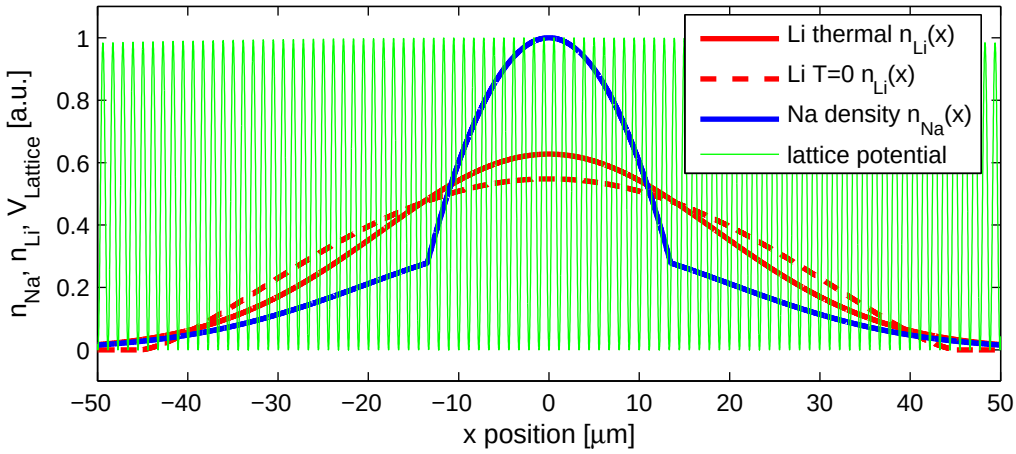

Figure 6.2.: *SSODT potential (green) and cut through atomic density distributions in x-direction. For plotting, we chose typical values (see section 8.4): At a temperature $T = 240\,$nK, we have $2.6 \cdot 10^5$ sodium atoms with a condensate fraction of $\eta = 0.4$ (blue line). The $7 \cdot 10^4$ lithium atoms at this particular temperature show a similar density distribution if assumed to be distinguishable particles (red solid line) or $T = 0$ fermions (red dashed line).*

For performing polaron experiments, it is of course desirable to have all lithium atoms in contact with a BEC. This could be reached by opening the ODT after loading lithium into the optical lattice, which means that in x-direction the lithium density distribution is frozen whereas the extension of the sodium condensate can increase. As one can easily see from eqs. (3.27) and (3.28), $R_{TF} \propto \omega_x^{-2/3}$ and thus we would have to decrease ω_x by a

factor of ~ 8 to have a condensed background gas in contact with each occupied lattice site. A rather technical difficulty stems from the implementation of the ODT in our experiment, i. e. simultaneously to ω_x we also ramp down ω_z, whose value is given by the same IR-beam. This would cause overlap problems due to the differential gravitational sag $\Delta z = (g/\omega^2_{z,\mathrm{Na}} - g/\omega^2_{z,\mathrm{Li}})$, which grows with decreasing trap frequencies.

An additional overlap problem could arise due the condensate Thomas-Fermi radius being dependent on the intraspecies scattering lenght a_{BB}. Combining eqs. (3.27) and (3.28), we get $R_{TF} \propto \sqrt[5]{a_{BB}}$, i. e. decreasing a_{BB} by one order of magnitude decreases R_{TF} by 1.6, being for $a_{BB} \to 0$ ultimately limited by the harmonic oscillator length $a_{ho} = 2.4\,\mu$m. Reaching this limit is - even apart from experimental challenges with regard to magnetic field stability - problematic anyway, as in this non-interacting case the Bogoliubov modes vanish. Without those phonon-like excitations, which are essential to explain the Fröhlich polaron, the validity of the whole theoretical analysis of Ref. [21] has to be scrutinized.

6.1.3. Full QM Description of a Particle in a Periodic Potential

Bloch functions

So far, we have derived the design criteria for our SSODT in a simple harmonic oscillator approximation, i. e. we constrained our considerations to independent lattice wells with vanishing tunneling coupling among each other. In the following, we will give a complete theoretical treatment of the lattice Hamiltonian

$$H = \frac{p^2}{2m} + \frac{V_0}{2}\left(1 - \cos(2kx)\right) \tag{6.13}$$

describing an atom of mass m in the SSODT potential[5] eq. (6.5) with periodicity $d = \pi/k = \lambda/2$. The famous Bloch-Theorem [102] tells us that we can write the eigenfunctions of the periodic Hamiltonian as

$$\psi_{n,q}(x) = e^{iqx/\hbar} u_{n,q}(x) \tag{6.14}$$

with the periodic function $u_{n,q}(x) = u_{n,q}(x + d)$. We see that the eigenfunction $\psi_{n,q}(x)$ does not necessarily show the same periodicity as the Hamiltonian, as it can have an additional phase factor $e^{iqx/\hbar}$. Here, n denotes the so-called bandindex and $q \in [-\hbar k; \hbar k]$ the quasimomentum, which will both be explained in detail later. Due to its periodicity, we can expand the Bloch function $u_{n,q}(x)$ in a Fourier series as

$$u_{n,q}(x) = \sum_{l \in \mathbb{Z}} c_l^{n,q} e^{i2lkx} \tag{6.15}$$

[5] The inhomogeneity of the optical potential discussed above is neglected in the following to allow for an analytical treatment.

with $2lk$ being the reciprocal lattice vectors. Analog, the potential reads

$$V(x) = \sum_{l\in\mathbb{Z}} V_l e^{i2lkx} = \frac{V_0}{2} - \frac{V_0}{4}\left(e^{i2kx} + e^{-i2kx}\right) . \tag{6.16}$$

It is interesting to note that in the case of an optical lattice the only nonvanishing Fourier components of the potential are V_{-1}, V_0 and V_{+1}, whereas in the case of condensed matter systems constraining the calculations to those three components is always an approximation. Inserting the Fourier expansions and the Hamiltonian eqs. (6.15), (6.16) and (6.13) into the Schrödinger equation $H\psi_{n,q}(x) = E_{n,q}\psi_{n,q}(x)$, we get

$$\sum_{l\in\mathbb{Z}} e^{i(q/\hbar+2kl)x}\left[\left(\frac{(q+2\hbar kl)^2}{2m} - E_{n,q}\right)c_l^{n,q} + \sum_{l'\in\mathbb{Z}} V_{l'}c_{l-l'}\right] = 0 . \tag{6.17}$$

We see that due to the orthogonality of plane waves the bracketed term must vanish for all l and thus we can obtain the eigenenergies $E_{n,q}$ and eigenvectors $c_l^{n,q}$ by diagonalization of the matrix

$$\begin{pmatrix} T_{q,z} - E_{n,q} + \frac{V_0}{2} & -\frac{V_0}{4} & 0 & \cdots & 0 \\ -\frac{V_0}{4} & T_{q,z-1} - E_{n,q} + \frac{V_0}{2} & -\frac{V_0}{4} & & \\ 0 & -\frac{V_0}{4} & T_{q,z-2} - E_{n,q} + \frac{V_0}{2} & & \vdots \\ \vdots & & & \ddots & \\ 0 & & \cdots & & T_{q,-z} - E_{n,q} + \frac{V_0}{2} \end{pmatrix} . \tag{6.18}$$

where $T_{q,l} = \frac{(q+2\hbar kl)^2}{2m}$ is the kinetic energy and the truncation parameter $z \geq l \geq -z$ is chosen appropriately. Thus, for each quasimomentum q, we get $2z+1$ eigenvalues $E_{n,q}$, which are shown for different lattice depths V_0 in figure 6.3. For $V_0 \to 0$, we see how the dispersion relation for a free particle reduced to the first Brillouin zone is reproduced, where we can retrieve the momentum $p = q + 2m\hbar k$ from quasimomentum q and reciprocal lattice vector $2m\hbar k$ with $m \in \mathbb{Z}$ chosen appropriately. $n = 1, 2, ...$ is the so-called band index, a denotation which becomes clear when looking at the energy levels for $V_0 > 0$, which are forming certain energy bands, also called Bloch bands. In the deep lattice limit $V_0 \gg E_r$, these bands coincide with the equally spaced harmonic oscillator levels for small n, i. e. in states which only probe the harmonic part of the sinusoidal potential.

The wavefunctions can be obtained by inserting the eigenvectors $c_l^{n,q}$ resulting from the diagonalization of eq. 6.18 into eqs. (6.14) and (6.15). In figure 6.4, we can see that in the lowest Bloch band the wavefunction for $q = 0$ has no nodes, whereas for $q = \pm\hbar k$, i. e. at the Brillouin zone edge, the wavefunction has nodes at all maxima of the optical lattice potential. For the second band , all wavefunctions have a node at the potential minimum, as expected for the first excited state, but the $q = 0$ and not the $q = \pm\hbar k$ state has additionally nodes at the potential maxima. These characteristics of the wavefunction explain the quasimomentum dependence of the band energies $E_{n,q}$ shown in figure 6.3.

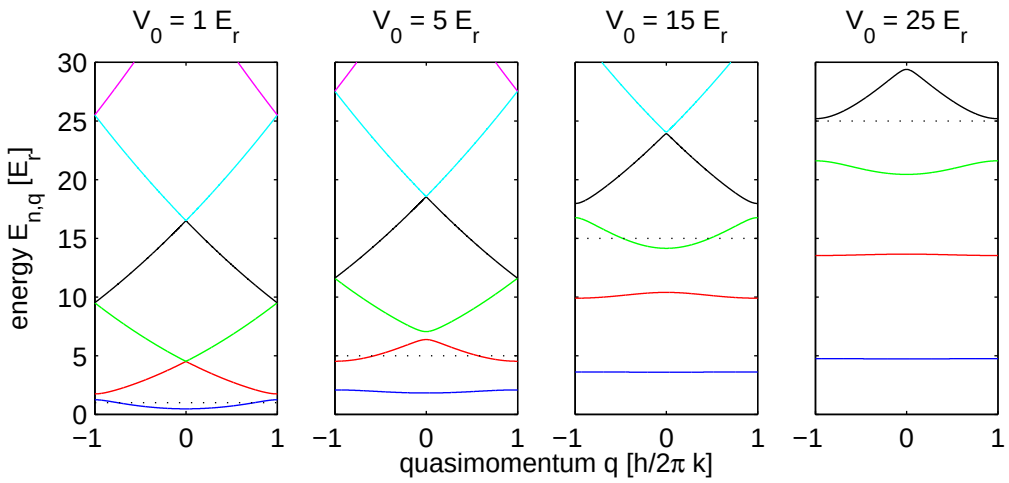

Figure 6.3.: *Bloch band energies $E_{n,q}$ obtained from diagonalization of matrix eq. (6.18) for different lattice depths V_0. The different Bloch bands are colour coded, whereas the respective lattice depth V_0 is shown as black dotted line. We see that for small lattice depth we approximately get the free particle dispersion relation in the reduced Brillouin zone scheme. For deeper lattices, the bandgap starts opening in the lower bands first, until for deep lattices the harmonic oscillator limit of (almost) flat bands is reached.*

Wannier Functions

In deep lattices, instead of working with the Bloch wavefunctions delocalized over the entire lattice it is more intuitive to use wavefunctions localized on one lattice site. For that purpose, we introduce the Wannier functions

$$w_n(x - x_j) = \mathcal{N}^{-1/2} \sum_{q \in [-\hbar k; \hbar k]} e^{-iqx_j/\hbar} \psi_{q,n}(x) \tag{6.19}$$

with $\mathcal{N}$ being an appropriately chosen normalization factor. In the sum above, one has to be careful to sum up all Bloch functions $\psi_{q,n}(x)$ with equal phases enforced at $x = 0$ for getting the correct $w_1(x)$ [103]. Whereas the Bloch states $\psi_{q,n}(x)$ are characterized by their quasimomentum q and are delocalized over the entire lattice, the Wannier functions $w_n(x - x_j)$ are localized at $x = x_j$. In figure 6.4, we can see a comparison of Bloch and Wannier functions, latter being also approximated with the harmonic oscillator wavefunctions, which are a good description for deep lattices. We see how our considerations to design the optical lattice, which were done in the harmonic oscillator approximation, are justified: Starting from the Bloch functions, which are the exact eigenfunctions of the lattice, we can do a basis change to Wannier functions. In the deep lattice limit, those become identical with the harmonic oscillator states.

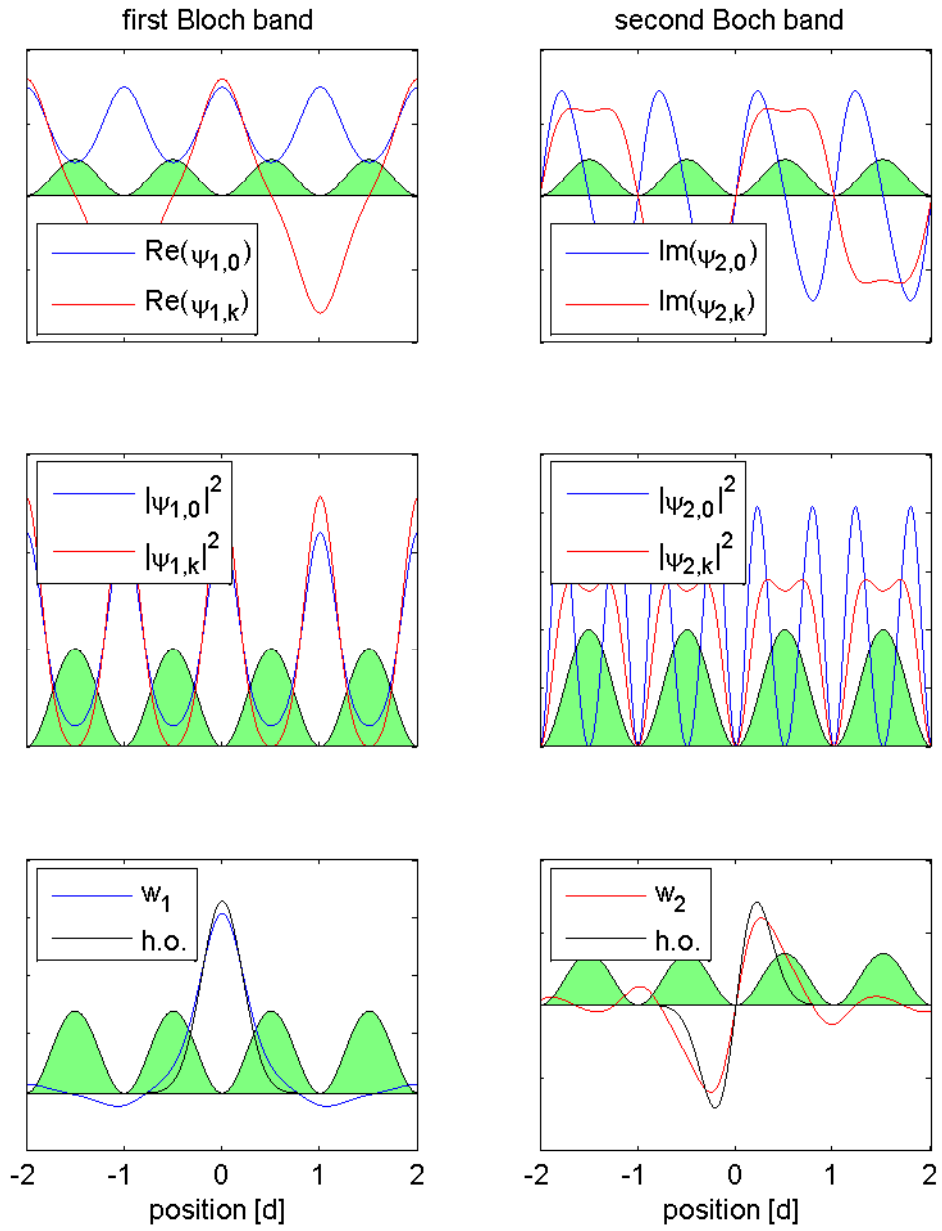

Figure 6.4.: *First Row: Wavefunctions $\psi_{q,n}(x)$ for $q = 0$ and $q = \hbar k$, i. e. in the middle and at the edge of the first Brilloin zone, respectively. Second row: Corresponding probability densities $|\psi_{q,n}(x)|^2$. Third row: Wannier functions $w_n(x)$ in comparison with the harmonic oscillator functions for comparable trap frequency. The larger spatial extent of the Wannier functions due to tunneling is obvious. In all graphs the depth of the lattice, which is depicted in green, is $s = 5$. For $s \approx 25$, a typical value used in our experiments, the difference between Wannier functions and harmonic oscillator states is not recognizable any more.*

Tunneling

When implementing lower-dimensional systems experimentally using an optical lattice, it is crucial that there is no tunneling between the distinct systems localized on neighbouring lattice sites i and j. The associated tunneling matrix element can be calculated as

$$J = \int w_n(x - x_j) \left(-\frac{\hbar^2}{2m} \frac{d^2}{dx^2} + V(x) \right) w_n(x - x_i) \, . \tag{6.20}$$

Here, the approximation of the Wannier functions by a simple harmonic oscillator is not correct, as for the tunneling process the sidelobes of $w_n(x - x_j)$ on lattice site i become important. From the results above, we can determine J in tight-binding approximation $s \gg 1$ by [104]

$$J = \frac{1}{4} \left(\max_q(E_{n,q}) - \min_q(E_{n,q}) \right) \, , \tag{6.21}$$

i. e. it is proportional to the width of the Bloch band. Plotting eq. 6.21 together with the approximate expression eq. (6.8) we see that for deep lattices $s \gg 1$ numeric and approximate analytic solution can be used likewise (figure 6.5 a).

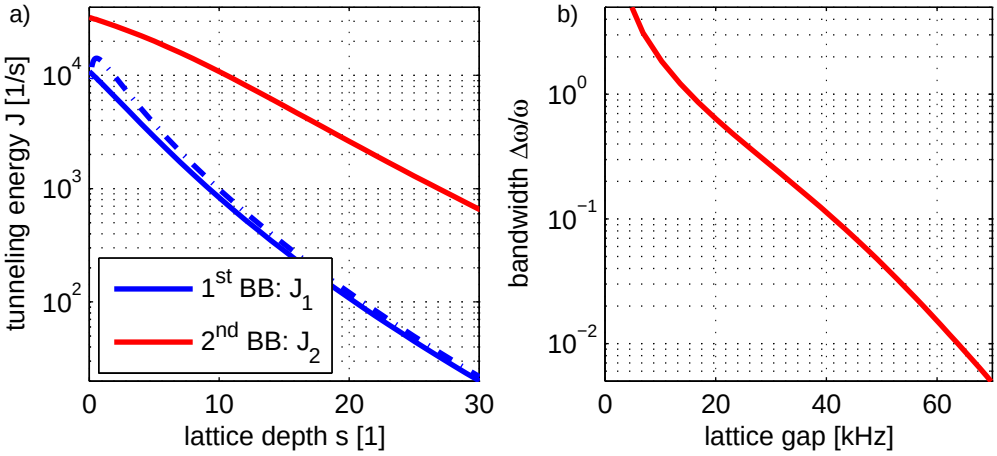

Figure 6.5.: ***a)*** *Tunneling energies J_1 and J_2 of first (blue) and second (red) Bloch band, respectively, in dependence of the lattice depth s. The approximate formula for the first Bloch band eq. (6.8) is shown as dashed blue line and is seen to be valid for $s \gg 1$. We clearly recognize that tunneling in the second band is always higher than in the first, which is explained by the higher spatial extent and thus overlap of the associated Wannier functions.* ***b)*** *Bandwidth $\Delta\omega$ in dependence of bandgap. For deep lattices, the bands get flat and the bandgap can be approximated by the lattice frquency ω. The bandwidth $\Delta\omega$ is defined here as the sum $\Delta\omega = 4(J_1 + J_2) \approx 4J_2$ of first and second Bloch band bandwidth and is responsible for dephasing of oscillations [105].*

To finish the theoretical part of this chapter, in order to prevent misunderstandings in nomenclature we want to discuss shortly the term of the 'effective mass': In condensed matter systems, the band structure gives rise to an effective mass

$$m^* = \left(\frac{d^2 E_{n,q}}{dq^2} \right)^{-1} \tag{6.22}$$

of the particle moving through the periodic potential. It is a useful term when explaining e. g. Bloch oscillations [106] induced by applying a force $F = m^* a$. However, this is a pure single particle effect appearing due to the band structure of the lattice. Throughout this thesis however, the term 'effective mass' is used to describe the mass increase of an impurity immersed in a bosonic background, which obviously is a many-body effect and not connected to the physics of periodic potentials.

6.2. Characterization of the Optical Lattice

Having designed the optical lattice, next we want to show how to characterize it by means of experiments with ultracold atoms. For that purpose, we first demonstrate the effect of a phase lattice on sodium and subsequently excite oscillations of lithium atoms.

6.2.1. Phase Lattice for Sodium

Before implementing the optical lattice for lithium, we used the dye laser as repumper for sodium [38]. Therefore it was convenient to first try and see effects of the lattice on sodium, before switching the dye from Rhodamine 6G to DCM to form a SSODT for lithium. For the measurements reported here, we chose a detuning of $\Delta/2\pi \approx 2\,\mathrm{GHz}$ and a lattice beam power of $\sim 21\,\mu\mathrm{W}$.

First, in order to see an impact of the lattice on the atoms, it would be desirable to observe some structure being connected to the periodic potential, even better if this structure could in some way be utilized to calibrate the lattice depth s. For that purpose, one can make use of a phase lattice [101]: For a short time t, the lattice is pulsed on and in dependence of this pulse duration, the diffracted momentum components $2l\hbar k$ of the atoms after a TOF-expansion are recorded.

To analyze this process analytically, let us start with a sodium condensate described by the wavefunction $|\Psi\rangle = |q_0\rangle$, i. e. being in a certain momentum state. For simplicity, we assume that q_0 is in the lowest Bloch band. By making use of the fact that the Bloch wavefunctions $\psi_{n,q}$ form a basis set for a certain $q = q_0$, we can write

$$\mathbb{1} = \sum_n |\psi_{n,q_0}\rangle \langle \psi_{n,q_0}| \tag{6.23}$$

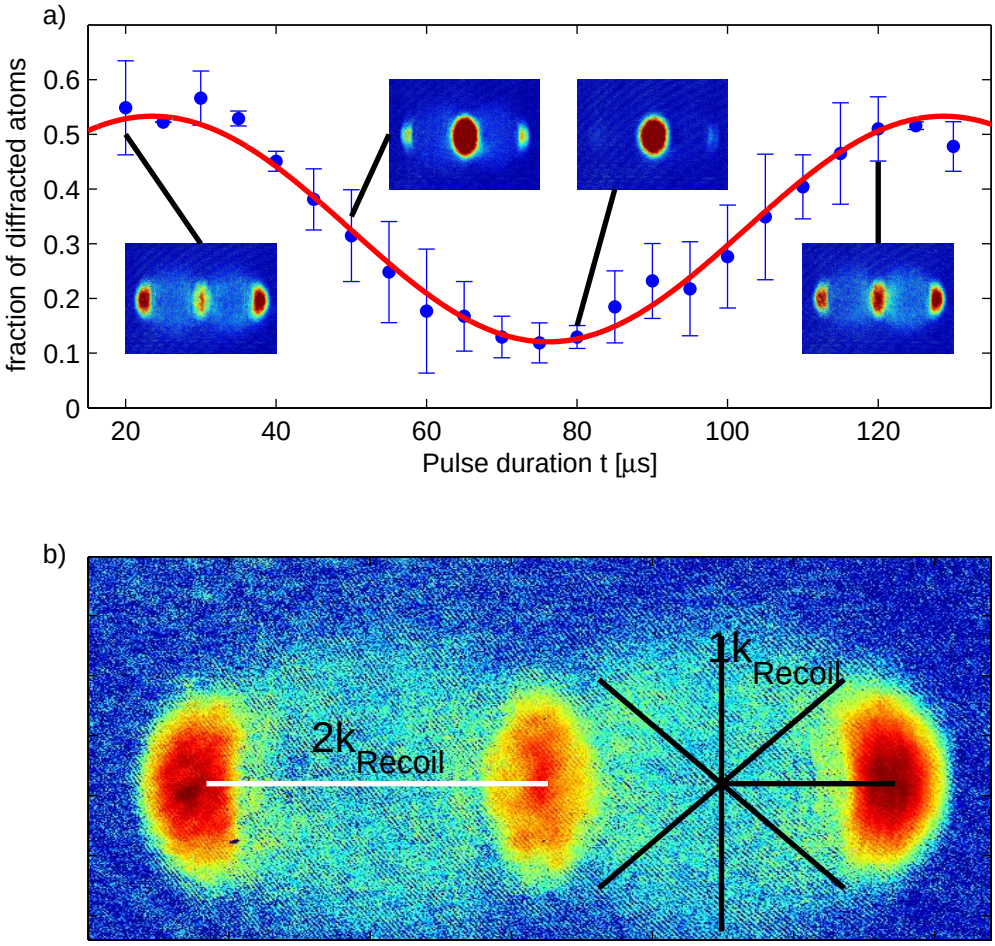

Figure 6.6.: ***a)*** *Sodium phase lattice for different pulse times t. The blue dots with errorbars are an average over two experimental runs. The frequency of the oscillation obtained from a sinusoidal fit (red line) is $\omega/2\pi = (9.5 \pm 1.1)\,\mathrm{kHz}$, which translates to $s \approx 1.8$. The insets show TOF-pictures the data have been obtained from.* ***b)*** *Picture showing s-wave scattering between $|p\rangle = |0\rangle$ and $|p\rangle = |\pm 2\hbar k\rangle$ atoms. To increase the visibility of the scattered with respect to the diffracted atoms, the color scale has been chosen logarithmic.*

and thus expand the condensate wavefunction as

$$|\Psi(t=0)\rangle = \sum_n |\psi_{n,q_0}\rangle \langle \psi_{n,q_0}|q_0\rangle \ . \tag{6.24}$$

With the Bloch wavefunction eq. (6.14), we get $\langle \psi_{n,q_0}|q_0\rangle = (c_0^{n,q_0})^*$ and thus the time evolution of the condensate wavefunction reads

$$|\Psi(t)\rangle = \sum_n e^{-iE_{n,q_0}t/\hbar}(c_0^{n,q_0})^* \, |\psi_{n,q_0}\rangle \tag{6.25}$$

if the lattice has been pulsed on for a time t. When it is turned off again, the wavefunction is projected onto plane waves, which are the appropriate basis states to describe the free atoms. The respective probability amplitude of the atom to end up in the momentum state $|q_0 + 2l\hbar k\rangle$ reads

$$\langle q_0 + 2l\hbar k|\Psi(t)\rangle = \sum_n e^{-iE_{n,q_0}t/\hbar}(c_0^{n,q_0})^*(c_l^{n,q_0})\,. \tag{6.26}$$

Making use of the fact that the condensate starts in a symmetric state $|q_0\rangle = |0\rangle$, it can due to parity reasons only be excited to bands with odd n (see wavefunction plots in figure 6.4). In the weak lattice limit, the atoms will thus only populate the $q = 0$ state of the third band, i. e. it they will be diffracted into the momentum state $|p\rangle = |\pm 2\hbar k\rangle$, as can be visualized from the reduction to the first Brillouin zone depicted in figure 6.3. Thus we can simplify eq. (6.26) to

$$|\,\langle \pm 2\hbar k|\Psi(t)\rangle\,|^2 = \alpha_1 + \alpha_2 \cos\left((E_{3,0} - E_{1,0})t/\hbar\right)\,, \tag{6.27}$$

where the α_i are a function of the $c_l^{n,q}$. The periodic diffraction of atoms into the momentum states $|\pm 2k\rangle$ can be mapped out in a TOF-series for different lattice pulse times t, as to be seen in figure 6.6. From the frequency of the oscillation $\omega/2\pi = (9.5 \pm 1.1)\,\mathrm{kHz}$, we get the energy difference between first and third Bloch band $(E_3 - E_1)$ for quasimomentum $q = 0$ and can thus determine the associated lattice depth $s \approx 1.8$.

An interesting feature can be seen in figure 6.6 b). Besides the $|p\rangle = |\pm 2\hbar k\rangle$ diffraction peaks, there are also atoms in the region between $|p\rangle = |0\rangle$ and $|p\rangle = |\pm 2\hbar k\rangle$. This can be understood as follows: When being diffracted, some of the atoms in $|p\rangle = |\pm 2\hbar k\rangle$ have to travel through the remaining condensate at rest $|p\rangle = |0\rangle$. The resulting scattering process of atoms from the two different velocity classes can be described in the center-of-mass system with momentum $|p\rangle = |\pm\hbar k\rangle$. The atom distributions after scattering, which appear in the absorption image as circular discs centered around $|p\rangle = |\pm\hbar k\rangle$, can be clearly identified as the results of s-wave scattering [107].

In the following, we will present further possibilities how to characterize the optical lattice by means of oscillations of lithium.

6.2.2. SSODT for Lithium

To follow the goal of our experiment to observe polaronic behaviour of lithium, we changed the wavelength of the dye laser to form an SSODT with wavelength of $\sim 670\,\mathrm{nm}$. After cooling the atoms in MT and ODT, we load them into the lattice, a process which is investigated in detail in the next chapter. In short, we ramp up the SSODT with a sodium background, such that the atoms have sufficient time for thermalization and a possible spatial rearrangement by tunneling. Depending on the kind of experiment, the sodium background is removed subsequently by a resonant light pulse.

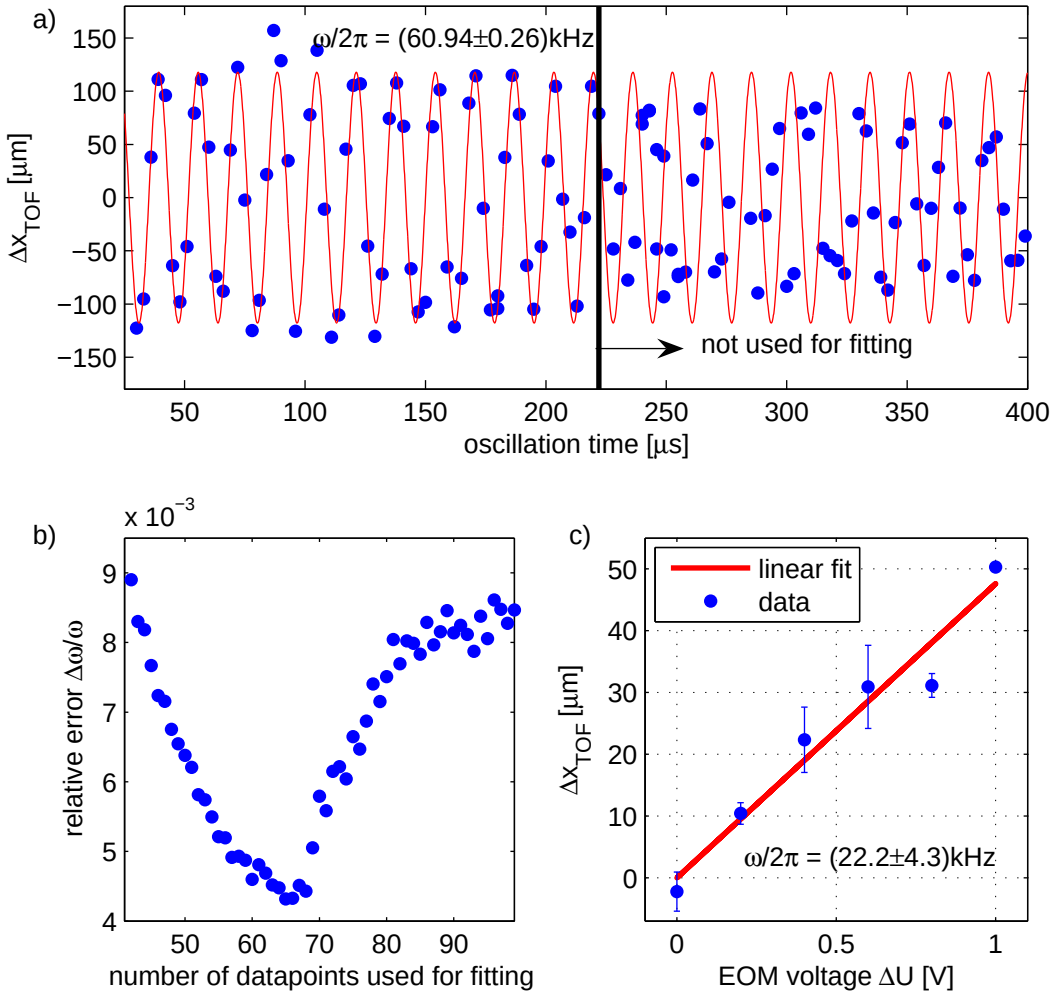

Figure 6.7.: ***a)*** *Oscillation of lithium in the lattice. The blue dots represent the center of mass after TOF, the red line is a sinusoidal fit to the data for $t < 222\,\mu$s.* ***b)*** *Relative frequency fit error $\Delta\omega/\omega$ in dependence of the number of datapoints used for fitting. The dataset minimizing the fit error $\Delta\omega/\omega$ has been used for the fit shown in a).* ***c)*** *Displacement Δx_{TOF} in dependence of EOM voltage ΔU (note that a different lattice than in a) and b) was used!). With $t_{\mathrm{TOF}} = 3\,\mathrm{ms}$, we get $\omega/2\pi = (22.2 \pm 4.3)\,\mathrm{kHz}$.*

To characterize the lattice for lithium, we excite oscillations. For that purpose, the voltage applied on the EOM[6] (see figure 6.1) is suddenly switched by an amount ΔU. This induces a phase shift between the two beams of $\Delta\phi = \phi' \Delta U$, where $\phi' = (0.414 \pm 0.003)1/\mathrm{V}$ in our

[6]For simplicity, we ΔU given here is the voltage from our experiment control system. For inducing phase shifts, this voltage is amplified by a factor of 20 by a high voltage amplifier and then directed to the EOM.

setup [100]. The resulting spatial displacement of the lattice structure is

$$\Delta x = \frac{\lambda}{4\pi}\phi' \Delta U = (72.5 \pm 0.5)\frac{\mathrm{nm}}{\mathrm{V}}\Delta U\,. \tag{6.28}$$

By switching lattice and ODT off a certain time t after the displacement, we can map out the oscillation in a TOF-series. The induced oscillation shown in figure 6.7 has a frequency of $\omega/2\pi = (60.94 \pm 0.26)\,\mathrm{kHz}$, which translates into $s = 26.2$. A feature which is not yet understood is depicted in figure 6.7 b): $\Delta\omega/\omega$ increases, i. e. the fit quality decreases when we take the datapoints for $t > 222\,\mu\mathrm{s}$ into account. From the lattice inhomogeneity and the confining ODT potential eq. (6.12), one would expect a timescale $\tau \approx 100/\omega \approx 2\,\mathrm{ms}$ for this process, which for longer times experimentally manifests as amplitude decrease. A possible explanation could be an improper alignment of SSODT with respect to the ODT, which would result in a faster dephasing than theoretically expected [105].

By fitting only the first ∼11 oscillations, we get for the frequency $\omega/2\pi = (60.94 \pm 0.26)\,\mathrm{kHz}$, i. e. without further effort we can determine it with a relative accuracy of ∼0.4%. This means that we are able detect an effective mass increase of $m^* = 1.008m$, which can be achieved by $\alpha = 0.02$, a value that can easily be reached by reducing a_{BB} only slightly as the background value $\alpha_{\mathrm{bg}} = 0.018$ is not much smaller.

In order to develop a deeper understanding for the oscillations, one can map out the amplitude of the first maximum in dependence of the applied voltage jump ΔU. The maximal atom velocity is $v = \omega\Delta x$, which translates in TOF into $\Delta x_{\mathrm{TOF}} = v t_{\mathrm{TOF}}$. From the fit of the data in figure 6.7, we get $\omega/2\pi = (22.2 \pm 4.3)\,\mathrm{kHz}$, which is in excellent agreement with $\omega/2\pi = (22.6 \pm 1.3)\,\mathrm{kHz}$ determined from a direct measurement of the oscillation frequency.

In chapter 8, we will further investigate controlled excitations in the SSODT. For that purpose, we apply the technique of Brillouin zone mapping, which will be described in detail in the next chapter.

7. Brillouin Zone Mapping

In order to map out the momentum distribution of atoms in an optical lattice, a commonly used tool is Brillouin zone mapping. In the following, we will explain its basic principles and apply it to understand and improve the lattice loading procedure.

7.1. Basic Principles

As we have seen in the previous chapter, to atoms in different Bloch bands different momenta can be assigned. Although the quasimomentum q can only take values within the first Brillouin zone $q \in [-\hbar k; \hbar k]$, it can be adiabatically mapped onto a real momentum $p = q + 2m\hbar k$ with $m \in \mathbb{Z}$. The way this works is visualized in figure 7.1: Starting from a deep lattice, its depth s is ramped down and the Bloch bands start more and more to resemble the free particle dispersion relation. In this process the quasimomentum q is conserved and the real momentum p is retrieved when the lattice has been turned off completely. A subsequent TOF translates the obtained momentum distribution into a spatial distribution, which we record via an absorption image.

Experimentally, the Brillouin zone mapping has to fulfill several requirements: On the one hand, it has to be slow with respect to the vibrational frequencies, such that the ramp-down is adiabatic and does not induce transitions between the different bands. On the other hand, it has to be fast with respect to collision times changing the momentum distribution (which is not an issue for fermions though). Moreover, as the confining ODT is turned off during the Brillouin zone mapping, thermally driven expansion of the lithium has to be considered as well.

We found that an exponential ramp $\propto \exp(-t/\tau)$ with time constant $\tau = 125\,\mu$s and duration $500\,\mu$s fulfils those requirements. With this tool at hand, we will in the following analyze the lattice loading process.

7.2. Lattice Loading

Looking at the evolution of Bloch bands when changing the lattice depth (figures 6.3 and 7.1), it is obvious that free atom states with energy $E > E_R$ can end up in an excited band $n > 1$ when the lattice is ramped up, a process which can not be prevented by adiabatic loading [108]. In our system, $E_R \approx 320\,\text{nK}$ and $E_F \approx 760\,\text{nK}$, thus with the help of the

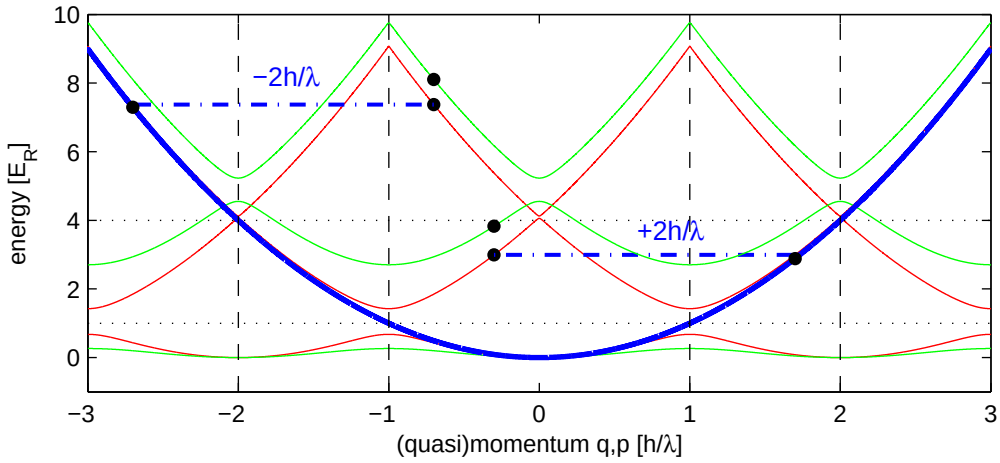

Figure 7.1.: *Basic scheme of Brillouin zone mapping. The atoms (black dots) in the lattice of depth $s = 5$ (green line) have a certain quasimomentum q, which is conserved during a ramp down to e. g. $s = 1.5$ (red line). When the lattice is turned off completely, the atom's quasimomentum is mapped onto the free particle dispersion relation (blue line) by adding a reciprocal lattice vector $\pm 2\hbar k = \pm 2h/\lambda$ to the quasimomentum q.*

intuitive picture figure 7.3 a) we can estimate that even at $T = 0$ about 40% the atoms will naturally end up in the second band. This theoretical prediction is confirmed by the Brillouin zone mapping shown in figure 7.2 a), where 44% of the atoms are in excited states. This energetically excited configuration is stable, as it can not relax due to the fermionic nature of the lithium atoms.

This constraint is lifted if we have a sodium background present when the lattice is being loaded: The lithium atoms in the excited states can scatter with the bosonic bath, thereby relaxing to lower bloch bands, a process schematically shown in figure 7.3 a). In figure 7.2 b) and c), we clearly see this effect, which we will investigate quantitatively in the following.

For the ramp-up of the lattice we choose an exponential ramp $s(t) \propto \exp(-t/\tau)$ with time constant τ and duration t_r. Fixing $\tau = t_r/4$ is commonly done in ultracold atom experiments [109, 110], but the ramp duration has to be adapted to our specific requirement that the lithium in the lattice has to thermalize with the sodium background. Figure 7.3 b) shows the result of loading the lattice with different ramp times: We see that for $t_r \approx 100\,\mathrm{ms}$, the fraction of atoms in the second Bloch band has reached its steady state value.[1] As a comparison, the case of lithium only is shown, which clearly does not show any relaxation from its metastable state.

[1] Due to the finite overlap of lithium atoms and sodium background (see figure 6.2), it is not surprising that some of the lithium atoms cannot relax to the first Bloch band due to the lack of sodium scattering partners, especially at the trap edges in the outer part of the lattice.

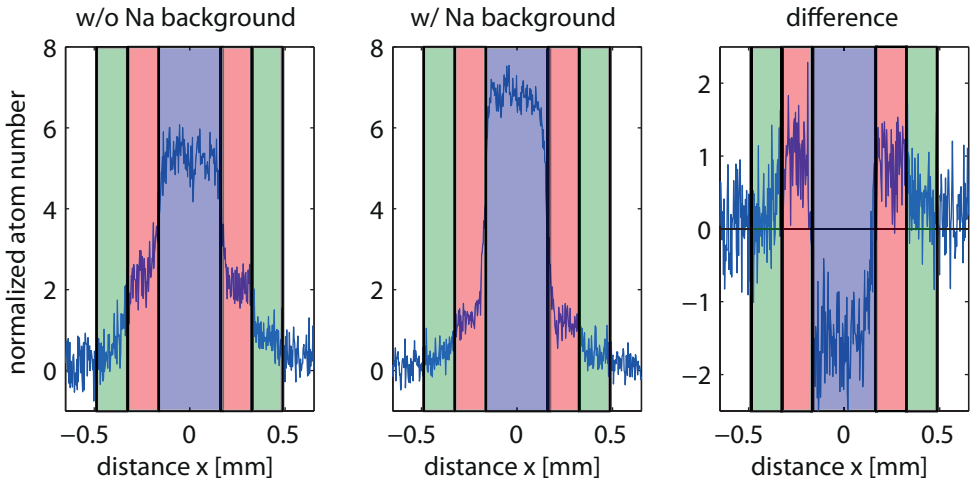

Figure 7.2.: *Left: Brillouin zone mapping of lithium loaded into the lattice without sodium background. About 44% of the atoms end up in excited states, which appear in TOF as higher Brillouin Zones depicted by different shadowing. Middle: If the lattice is loaded with a sodium background present, 86% of the atoms are in the lowest Bloch band. Right: The direct plot of the difference clarifies the effect of the bosonic background.*

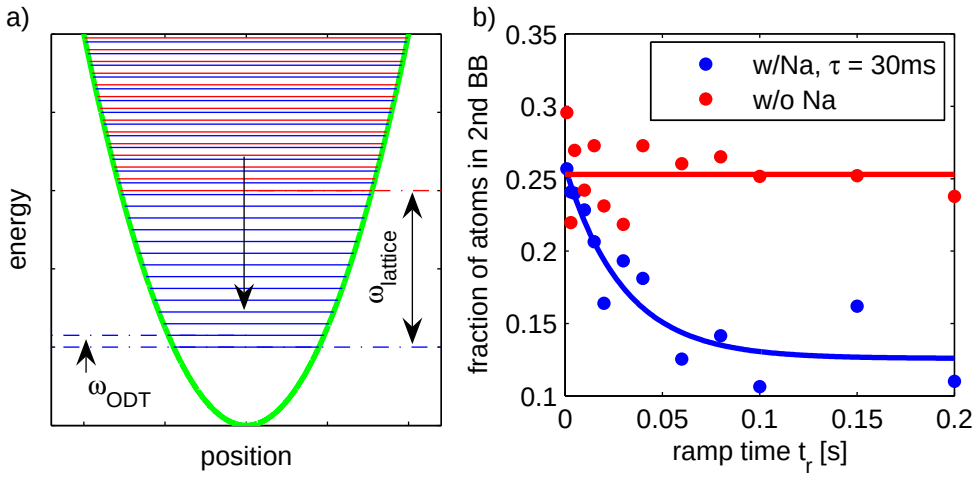

Figure 7.3.: ***a)*** *Lattice site in harmonic approximation. Shown are the potential (green) with the states of first (blue) and second (red) Bloch band, spaced by $\omega_{\mathrm{lattice}}$. The energetic distance between the transversally excited states is given by the ODT frequency ω_{ODT}. Note that $\omega_{\mathrm{lattice}} \gg \omega_{\mathrm{ODT}}$ and thus the picture is not to scale.* ***b)*** *Fraction of atoms in the second band in dependence of the lattice ramp time t_r. Without sodium (red dots), lithium stays in the metastable state, whereas with sodium (blue dots), the atoms are allowed to relax to the first Bloch band. The exponential fit (blue line) with a time constant $\tau = 30\,\mathrm{ms}$ leads to the choice of $t_r = 100\,\mathrm{ms}$.*

In the next chapter, we will investigate the lithium relaxation process quantitatively in detail. To understand it qualitatively, figure 7.3 a) is useful: With the help of sodium, the lithium atom can relax from second (red) to first (blue) Bloch band. The fact that this process is possible, i. e. the final state is not already occupied by another fermionic lithium atom and thus Pauli blocked, is a peculiarity of the one-dimensional lattice system. A manifold of transversal states from the ODT belongs to each Bloch band, as also depicted in figure 7.3 a). This way, to a certain energy $E > E_{2,q}$ there exists one state of the first *and* one of the second Bloch band. With typical values of $\omega_{\text{lattice}} \approx 50\,\text{kHz}$ and $\omega_{\text{ODT}} \approx 210\,\text{Hz}$, we find that there are about $3 \cdot 10^4$ states in the first Bloch band with energy E lower than the second band's energy. This means that with typically not more than $3 \cdot 10^3$ atoms per sheet, there is sufficient states for the fermionic atoms to relax to.

In the following, we will investigate how this configuration of states, which is specific to our setup, leads to the steep Brillouin zone edges as we can see in figure 7.2, which are in the case of a 3D lattice only obtained for certain fillings [111].

7.3. Brillouin Zone Edges

With some thousand atoms per lattice site, it is well justified to assume that the atoms' quasimomentum distribution more or less uniformly covers the entire first Brillouin zone $-\hbar k \leq q \leq \hbar k$. This means that when we do a BZ mapping, from each lattice site atoms start travelling with all those momenta q. Thus, the result of the bandmapping can be explained by summing over in-situ distributions, each displaced by q with $-\hbar k \leq q \leq \hbar k$, as schematically depicted in figure 7.4.

To quantify our so far only theoretical considerations, we map out the steepness of the Brillouin zone edges in dependence of different ODT frequencies, which change the slope of the in-situ distributions. Experimentally, we choose a TOF of 5 ms for the Brillouin zone mapping and obtain the prediction of the momentum distribution by summing over in-situ pictures taken at the same ODT frequency ω_{ODT}. The resulting spatial distributions, which have been calculated without free parameters, are linearly fitted at their respective Brillouin zone edges. The results plotted in dependence of ω_{ODT} can be seen in figure 7.4 b)[2].

The linear fits of the Brillouin zone edge slopes, depicted as solid lines in figure 7.4 b), are consistent within their uncertainties. Of course, agreement is not perfect due to several reasons: As already pointed out in chapter 3, in-situ pictures are quantitatively only limited trustworthy due to the high optical density. As the atom density increases with increasing ω_{ODT}, due to saturation effects in imaging we expect a lower slope for those in-situ pictures and the resulting sum. This explains why theory and experiment deviate more strongly for high ω_{ODT}, as can be seen in figure 7.4 b). Another source of errors is the anharmonic part of the in-situ distribution: Due to the ODT being formed by Gaussian beams of finite waist,

[2] Due to the maximum slope of a Gaussian distribution being proportional to $1/\sigma \propto \omega$, it is reasonable to plot the slope of the BZ edge in dependence of ω.

the wings of the atom distribution are broader than expected in a pure harmonic potential. This leads to the theoretically predicted shape of the Brillouin zone mapping having rather smooth edges, whereas the experimentally obtained shape can be almost approximated by a box as it mostly stems from atoms being trapped in the harmonic part of the ODT potential.

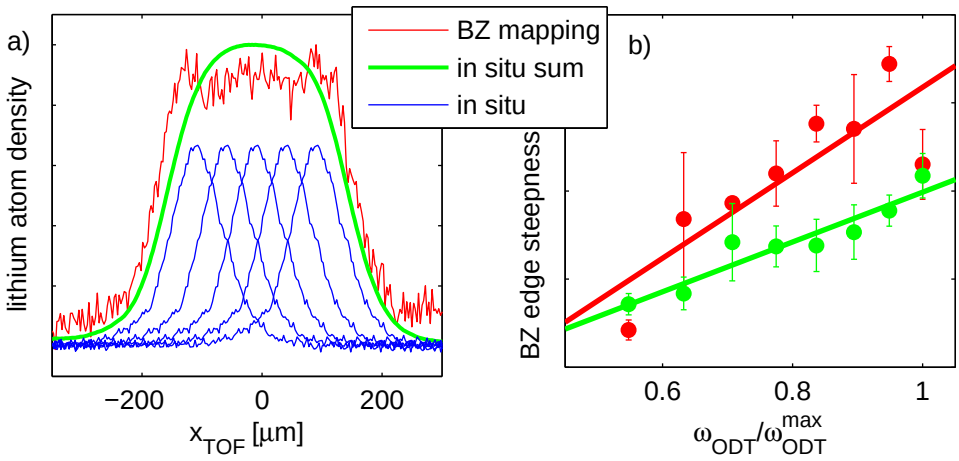

Figure 7.4.: a) *Schematic of the emergence of a typically observed spatial distribution in BZ mapping: By summing over in-situ distributions with all different quasimomenta q (blue), we get a theoretical predicition for the result of the BZ mapping (green). The result shows astonishing similarity to the results obtained experimentally (red).* ***b)*** *Slope of the Brillouin zone edges in dependence of the ODT frequency ω_{ODT}, color coding as in a). Errorbars are due to taking the mean of slope of left and right BZ edge. The lines are linear fits to the data with slopes $a_{\mathrm{BZ}} = 24 \pm 10$ and $a_{\mathrm{IS}} = 14 \pm 4$, agreeing within their uncertainties.*

In this chapter, we have introduced the tool of Brilloun zone mapping. By analyzing the relaxation of excitations, we have applied it to optimize the loading procedure of the SSODT. In the next chapter, we will go one step further and deliberately transfer atoms to higher Bloch bands, a process which can be analyzed with the Brillouin zone mapping technique.

8. Controlled Excitations in the Optical Lattice

In this chapter, we will investigate excitations of the atoms in the optical lattice in detail. We start with a derivation of a quantum mechanical picture of oscillations in the harmonic oscillator limit, which we extend to the full treatment using Bloch wavefunctions and compare to experimental data. To get a quantitative understanding of the interspecies energy transfer in a Bose-Fermi mixture, we analyze heating of the condensed Bose gas in dependence of the lithium oscillation energy.

In order to be able to excite lithium to one specific Bloch band instead of preparing it in a superposition as done in the case of oscillations, we apply an oscillatory displacement of our lattice and are thus able to spectroscopically determine the bandgap. When the lithium atoms are transferred to the excited state of the two-level system consisting of the mechanically coupled first and second Bloch band, a sodium background can induce their relaxation to the first Bloch band, as we have already seen in the previous chapter. By employing a controlled excitation and quantitatively analyzing its relaxation, we can determine the absolute value of the interspecies scattering length a_{IB}. To give an outlook on the rich spectrum of physics that can be investigated using this two-level system coupled to a bath, we finally demonstrate Rabi oscillations between first and second Bloch band.

8.1. Quantum Mechanical Picture of Oscillations

In the limit of a deep lattice, where the Bloch wavefunctions can be approximated by simple harmonic oscillator wavefunctions, an oscillation can be described analytically. To excite the oscillation, we displace the wavefunction $|\psi(x)\rangle$ by Δx, which can be described by applying the displacement operator

$$e^{-\frac{i}{\hbar}\Delta x\hat{p}}\,|\psi(x)\rangle = |\psi(x-\Delta x)\rangle\ , \tag{8.1}$$

which is well-known from basic quantum mechanics [28]. Introducing the harmonic oscillator length scale $x_0 = \sqrt{\frac{2\hbar}{m\omega}}$ and the raising and lowering operators $\hat{a}^\dagger$ and $\hat{a}$, we can rewrite

$$e^{-\frac{i}{\hbar}\Delta x\cdot\hat{p}} = e^{-\frac{i}{\hbar}\Delta x\cdot i\sqrt{\frac{\hbar m\omega}{2}}(\hat{a}^\dagger-\hat{a})} = e^{\frac{\Delta x}{x_0}(\hat{a}^\dagger-\hat{a})} = D(\alpha)\,. \tag{8.2}$$

Here, we defined $\alpha \equiv \frac{\Delta x}{x_0}$ and introduced the displacement operator $D(\alpha) = \exp(\alpha \hat{a}^\dagger - \alpha^* \hat{a})$, which is also used in Quantum Optics [112].

Starting with atoms in the harmonic oscillator ground state $|\psi(x)\rangle = |0\rangle$, we obtain its decomposition in energy eigenstates $|n\rangle$ after the displacement

$$\begin{aligned} |\psi(x-\Delta x)\rangle &= \sum_n |n\rangle \langle n|\psi(x-\Delta x)\rangle \\ &= \sum_n |n\rangle \langle n|D(\alpha)|0\rangle \\ &= \sum_n |n\rangle \langle n| \sum_{n'} e^{-\frac{|\alpha|^2}{2}} \frac{\alpha^{n'}}{\sqrt{n'!}} |n'\rangle \\ &= \sum_n e^{-\frac{|\alpha|^2}{2}} \frac{\alpha^n}{\sqrt{n!}} |n\rangle \ . \end{aligned} \tag{8.3}$$

In the case of a lattice with finite depth s, we obtain the result analog to eq. (8.3) with $|n\rangle$ in this case being the Bloch wavefunctions of the different bands. The overlap integrals can be evaluated numerically using the eigenstates obtained in chapter 6. Note that in this case, the expansion of the displaced state is weakly dependent on the quasimomentum q, an effect which decreases for increasing lattice depth and vanishes in the harmonic oscillator limit.

In figure 8.1, oscillations with different amplitudes are shown for a lattice of depth $s = 14$. In order to be able to compare theory with experiment, the theoretical data has been appropriately averaged over all quasimomenta $q \in [-\hbar k; \hbar k]$ of the first Brillouin zone. The experimental data has been obtained by excitation of oscillations with different amplitude and subsequent BZ mapping. We see qualitative agreement, but a quantitative discrepancy which could e. g. be due to the imperfect preparation of the initial state, which still contains a considerable fraction of atoms in the second Bloch band (see datapoints for zero displacement).

Very insightful is the comparison of the calculation involving the full set of Bloch states with the harmonic oscillator approximation, which is for reasons of clarity in figure 8.1 only shown for $\Delta x < 0$. We see that for small displacements approximation and exact calculation agree well for the three lowest bands. The fourth band, which is completely in the continuum for $s = 14$, is for that reason qualitatively not correctly described by the harmonic oscillator approximation.

8.2. Interspecies Energy Transfer

As we have the possibility to study not only lithium alone in the SSODT, but can also add a sodium background, a question that comes up naturally is how thermalization between the two works. In chapter 5, we have already studied the damping of oscillations in the case of

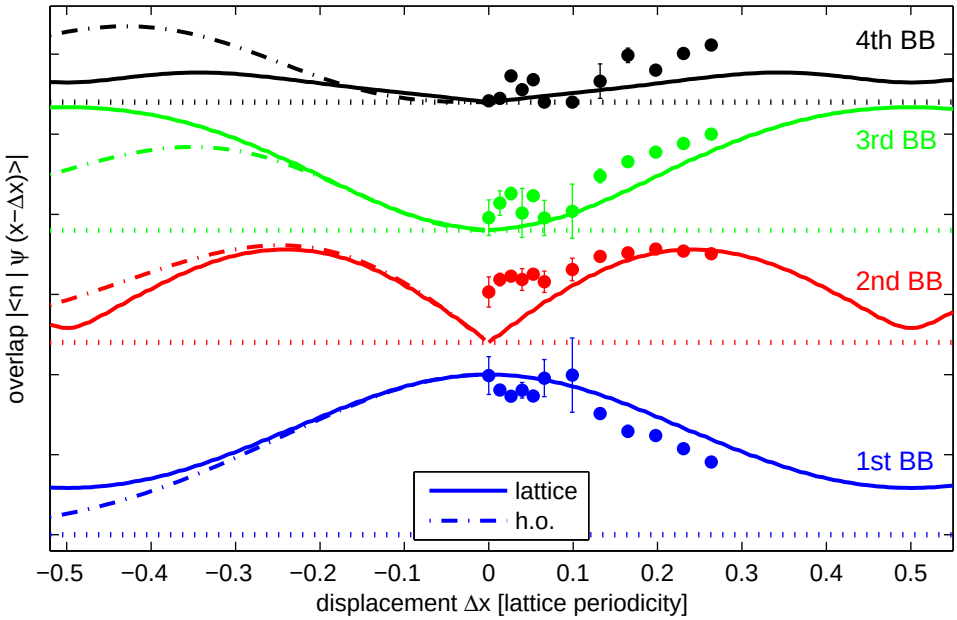

Figure 8.1.: *Overlap of the displaced wavefunction $|\psi(x-\Delta x)\rangle$ with the respective eigenstates $|n\rangle$. The first to fourth Bloch band are depicted in blue, red, green and black, respectively, and have been offset for clarity, the respective zeros shown as dotted horizontal lines. The experimental data (dots) have been obtained by Brillouin zone mapping and are averaged over two experimental runs. The qualitative agreement with the theoretical calculation using Bloch wavefunctions (solid lines) is obvious. For small oscillation amplitudes, the harmonic oscillator approximation (dashed-dotted lines, for clarity only shown for $\Delta x < 0$) gives a good description for the three lowest Bloch bands. Note the symmetry in the case of Bloch wavefunctions around a displacement of half a lattice period.*

both species being excited. Working with an SSODT for lithium, we will thus study how energy is transferred from the excited lithium atoms to the sodium condensate.

For that purpose, we prepare lithium in the SSODT with a sodium condensate background. An oscillation of the fermions is excited and after a certain hold time t_h a TOF picture is taken. Experimentally, we choose $t_h = 1\,\mathrm{s}$, a value which ensures that lithium and condensate are well thermalized (see chapter 5). Figure 8.2 shows the resulting sodium condensate fraction in dependence of the lithium oscillation amplitude. In the following, we will develop a quantitative understanding of this energy transfer process.

The specific heat of an ideal Bose gas of N_{Na} sodium atoms in a three-dimensional harmonic trap is given by [31]

$$C = 3 \cdot 4 \cdot \frac{\zeta(4)}{\zeta(3)} N_{\mathrm{Na}} \cdot k_B \left(\frac{T}{T_c}\right)^3 \approx 10.8 \cdot N_{\mathrm{Na}} \cdot k_B \left(\frac{T}{T_c}\right)^3 \tag{8.4}$$

with $\zeta(x)$ denoting the Riemann zeta function. A temperature increase from T_i to T_f is

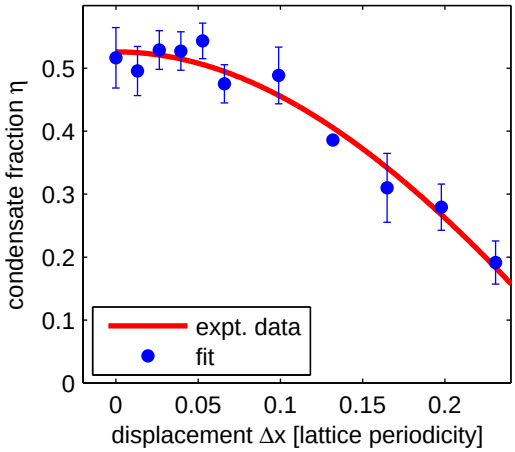

Figure 8.2.: *Sodium condensate fraction η in dependence of the lithium displacement. The experimental data (blue dots) are an average over two runs and over the condensate fraction fitted in x- and y-direction. The red line is a fit based on the specific heat of the ideal Bose gas as described in the text. The data were obtained in a lattice with frequency $\omega/2\pi = 45\,\mathrm{kHz}$.*

connected with a heat input

$$\Delta Q = \int_{T_i}^{T_f} C(T)\,\mathrm{d}T\,. \tag{8.5}$$

Evaluating this integral and inserting it into the formula for the condensate fraction eq. (3.30) $\eta = 1 - \left(\frac{T}{T_c}\right)^3$, we get

$$\eta = 1 - \left(\frac{\Delta Q}{2.7 N_{\mathrm{Na}} k_B T_c} + \left(\frac{T_i}{T_c}\right)^4\right)^{3/4}\,. \tag{8.6}$$

Knowing the lattice frequency ω and the lithium atom number N_{Li}, we can determine the heat transfer

$$\Delta Q = N_{\mathrm{Li}} V_0 \sin^2(k\Delta x) \approx \frac{1}{2} N_{\mathrm{Li}} m_{\mathrm{Li}} \omega^2 \Delta x^2 \tag{8.7}$$

in dependence of oscillation amplitude, i. e. the displacement Δx. Fitting the data in figure 8.2 with eqs. (8.6) and (8.7), we get when leaving the critical temperature as free parameter $T_c = (355 \pm 74)\,\mathrm{nK}$, with the error given by the uncertainties in N_{Na}, N_{Li} and the fit. The corresponding ODT trapping frequency $\bar{\omega}/2\pi = (118 \pm 25)\,\mathrm{Hz}$ is in good agreement with the value $\sqrt[3]{\omega_x\omega_y\omega_z}/2\pi = 93\,\mathrm{Hz}$ which we obtain from the direct measurement of the trapping frequencies.

From theoretical work [113] we know that for a harmonically trapped weakly interacting Bose gas the specific heat scales as $(T/T_c)^\alpha$ with $\alpha < 3$ opposed to $\alpha = 3$ in the non-interacting case. The scaling has experimentally been determined to be $\alpha = (2.7 \pm 0.7)$ in

the case of rubidium [114], but leaving α as a free parameter for the fit of our data sample results in a value being meaningless due to its large uncertainty.

This first measurement of lithium oscillating in a sodium background can be extended in many ways: If the bosons form a pure condensate, the impurity should perform a frictionless oscillation as long as the associated velocity is slower than the superfluid critical velocity v_c. Thus, a measurement of the energy transfer in dependence of the oscillation amplitude can be used to determine v_c. Moreover, if one is able to load just a few lattice sites, the lithium can even be used as a local probe to map out its spatial, i. e. density dependence. So far, the superfluid critical velocity has been determined experimentally by moving a blue detuned laser beam [91] and sodium atoms in different hyperfine states [92] through a bosonic condensate. The idea of dragging an impurity through a condensed background to determine v_c has just recently been implemented with an ion moved through a BEC [94].

In the following, we want to study the dynamics of the energy transfer from excited lithium atoms to the sodium bath. Instead of exciting an oscillation of the lithium, which involves several Bloch bands in the theoretical description, we rather want to drive the transition between first an second band, which allows for a theoretical modelling as a two-level system.

8.3. Coherent Transfer Between Different Bloch Bands

From perturbation theory, we know that we can drive transitions between two states of a system by applying an appropriate excitation at the associated frequency. Mathematically speaking, the unperturbed time-independent Hamiltonian eq. (6.13)

$$H_0(x) = \frac{p^2}{2m} + V_0 \sin^2(kx) \tag{8.8}$$

experiences a time-dependent perturbation $H'(x,t)$ such that

$$H(x,t) = H_0(x) + H'(x,t)\,. \tag{8.9}$$

One sees that there is two obvious ways to achieve a time-dependent perturbation by manipulating $V(x)$: One can give the lattice depth V_0 a time dependence, i. e. $V_0 \to V_0(1+\varepsilon\sin(\omega_{\mathrm{ex}}t))$, which can be realized experimentally by modulating the lattice beam's intensity. In this case $H'(x,t) = V_0\varepsilon\sin(\omega_{\mathrm{ex}}t)\sin^2(kx) = H'(-x,t)$, i. e.it is an even-parity excitation which couples Bloch bands with $\Delta n = 2m$ with $m \in \mathbb{Z}$.

Another way to induce an excitation is to shake the lattice, i. e. $V(x) \to V(x+x_0\sin(\omega_{\mathrm{ex}}t)) = V_0\sin^2(k(x+x_0\sin(\omega_{\mathrm{ex}}t)))$. In the harmonic oscillator limit, we can do a Taylor expansion around $x=0$ and get to leading order in $x_0\sin(\omega_{\mathrm{ex}}t)$

$$H'(x,t) = 2V_0\cdot(kx_0)(kx)\sin(\omega_{\mathrm{ex}}t)\,. \tag{8.10}$$

We see that in this case $H'(x,t) = -H'(-x,t)$, thus this odd-parity excitation couples Bloch bands with $\Delta n = 2m+1$ with $m \in \mathbb{Z}$, in particular first and second Bloch band.

Experimentally, we realize the driving using the EOM to periodically modulate the phase of one beam with respect to the other and thus get a periodic displacement of the lattice wells.

A first example of the effect of the periodic shaking at the resonance frequency between first and second Bloch band can be seen in figure 8.3 a): After a Brillouin zone mapping, we clearly see that most atoms are transferred into the second Bloch band.

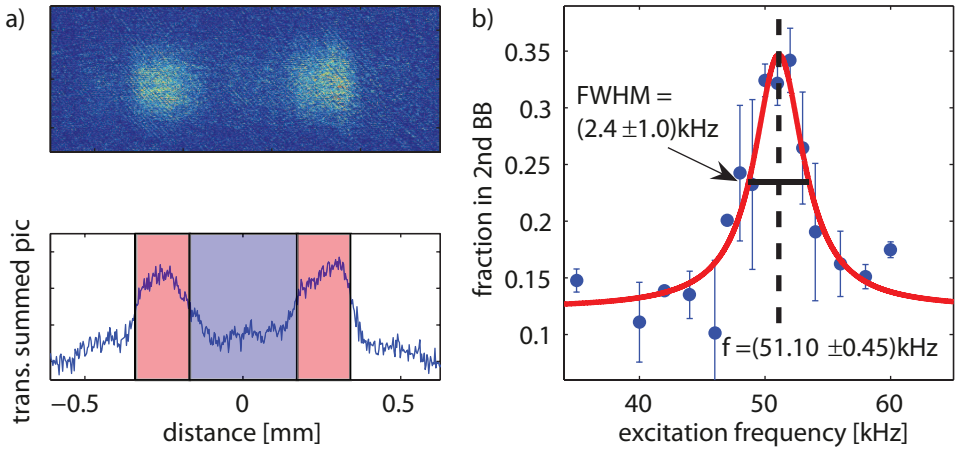

Figure 8.3.: ***a)*** *Excitation of lithium atoms to the second Bloch band by periodic lattice shaking.* ***b)*** *Spectroscopy of lithium atoms in the SSODT. In contrast to a), the excitation amplitude x_0 is kept as low as $3.3 \cdot 10^{-3}$ lattice periods in order to minimize the power broadening. The shaking duration of $\sim 200\,\mu$s corresponds to about 10 periods needed to excite the atoms.*

Next, we want to improve our understanding of the excitation by doing spectroscopy of the atoms in the lattice: We map out the fraction of atoms in the second Bloch band in dependence of the excitation frequency at fixed amplitude x_0 and duration of the shaking. The resulting data are fitted with a Lorentzian lineshape, as to be seen in figure 8.3 b). The fit determines $\omega/2\pi = (51.10 \pm 0.45)\,$kHz, i. e. we can determine the lattice frequency with an accuracy of $9 \cdot 10^{-3}$. In chapter 6, we obtained a relative uncertainty of $4.3 \cdot 10^{-3}$ when determining ω by means of a spatial oscillation of Lihtium atoms, thus the spectroscopy method as applied here can not (yet) compete with the 'simple' oscillation measurement.

Another insightful parameter obtained by the fit is the width of the Lorentzian $\Delta\omega = (2.4 \pm 1.0)\,$kHz. We see that $\Delta\omega/\omega = (47 \pm 20) \cdot 10^{-3}$, while we expect from the bandwidth $\Delta\omega/\omega = 39 \cdot 10^{-3}$, as graphically shown in figure 6.5. The agreement between theory and experiment is good, advantaged by the large fit uncertainty. For a more accurate spectroscopy, one expects to measure experimentally a slightly higher value of $\Delta\omega/\omega$ than expected from the theoretically obtained band structure due to power broadening, an effect known from quantum optics [46].

With the ability to transfer the lithium atoms from the first to the second Bloch band of

the SSODT, we will in the following analyze the subsequent relaxation process which can be induced by a sodium background.

8.4. Determination of the Interspecies Scattering Length

One can evaluate the measurement of sodium induced lithium relaxation from the second to the first BB in order to extract information about the interspecies scattering length. Therefore, we start with the simple formula

$$\Gamma = n\sigma v \tag{8.11}$$

describing the scattering rate Γ of particles with velocity v travelling through a medium of density n. The scattering cross section $\sigma = 4\pi a_{BF}^2$ gives us information about the absolute value of the scattering length. In our experimental situation, in dependence of its lattice site and transversal state each lithium atom probes a different bosonic background density $n = n_{\mathrm{Na}}$. Therefore, if we attribute a relaxation rate Γ_i to each lattice site i, the number of atoms in the second Bloch band $N(t)$ will be described by

$$N(t) = \sum N_i e^{-\Gamma_i t}, \tag{8.12}$$

where N_i denotes the number of atoms in the second BB on lattice site i at time $t = 0$. As already done in chapter 5, we approximate the envelope shape of the atoms in the lattice by the factorizable Maxwell-Boltzmann distribution $n_{\mathrm{Li}}(x, y, z) = Nf(x)f(y)f(z)$ and can thus write

$$\begin{aligned} N(t) = \sum N_i e^{-\Gamma_i t} &= \int \mathrm{d}x\ Nf(x)e^{-\Gamma(x)t} \\ &\approx \int \mathrm{d}x\ Nf(x)\left(1 - \Gamma(x)t\right) = N\left(1 - \int \mathrm{d}x\ f(x)\Gamma(x)t\right) \end{aligned} \tag{8.13}$$

with the Taylor approximation being valid for small $\Gamma(x)t$. Experimentally, we measure and fit a total relaxation

$$N(t) = Ne^{-\Gamma t} \approx N\left(1 - \Gamma t\right) \tag{8.14}$$

and thus by equating eqs. (8.13) and (8.14) we get

$$\Gamma = \int \mathrm{d}x\ f(x)\Gamma(x) \tag{8.15}$$

Noting that we have to weight the background boson density n_{Na} in eq. (8.11) for a certain lattice site with the two-dimensional fermionic density $f(y)f(z)$, we finally arrive at

$$\begin{aligned} \Gamma = \int \mathrm{d}x\ f(x)\Gamma(x) &= \int \mathrm{d}x\ f(x) \int \mathrm{d}y\ \mathrm{d}z\ \sigma v n_{\mathrm{Na}}(x, y, z)f(y)f(z) \\ &= \sigma v \int \mathrm{d}V\ n_{\mathrm{Na}}(x, y, z)\frac{n_{\mathrm{Li}}(x, y, z)}{N}\,. \end{aligned} \tag{8.16}$$

As we experimentally deal with two-dimensional lithium clouds, the velocity v along the x-direction will be given by the confinement, whereas in y and z it is determined by temperature. For those three independent directions, the velocities add quadratically, thus we have to ask about the mean squared velocities. For a harmonic oscillator, the wavefunction in the first excited state (i. e. in the second Bloch band of our lattice) reads in momentum space

$$\psi(p) = \frac{\sqrt{2}p}{(\pi(m\hbar\omega)^3)^{1/4}} e^{-\frac{p^2}{2m\hbar\omega}} \tag{8.17}$$

and thus

$$\left\langle p_{ho}^2 \right\rangle = \langle \psi(p)|p^2|\psi(p)\rangle = \frac{3}{2} m\hbar\omega \,. \tag{8.18}$$

Similarly, we get with the Maxwell-Boltzmann Distribution in a harmonic trap

$$f(p) = \frac{1}{\sqrt{2\pi m k_B T}} e^{-\frac{p^2}{2mk_BT}} \tag{8.19}$$

the thermal velocity for one dimension

$$\left\langle p_{th}^2 \right\rangle = \int \mathrm{d}p \; p^2 f(p) = m k_B T \,. \tag{8.20}$$

For the experimental data presented in figure 8.4, the temperature is $T = (240 \pm 9)\,\mathrm{nK}$ and the lattice frequency $\omega/2\pi = 40\,\mathrm{kHz}$, thus $p_{th}^2/p_{ho}^2 = 0.08$, so most collisions happen in the direction of the lattice. Moreover, the thermal velocity effects being almost negligibe also justifies the assumption of the sodium background to be at rest, i. e. not to contribute to v. The velocity associated to atoms in the second Bloch band $v_{ho} = \sqrt{\langle p_{ho}^2 \rangle}/m \approx 6\,\mathrm{cm/s}$ is much higher than the superfluid critical velocity of the condensate $v_c \approx 1\,\mathrm{cm/s}$, thus the excited lithium atoms interact both with sodium atoms in the condensate and the thermal cloud. Momentum and energy conservation yield that in a collision of lithium with a sodium background atom, the fermion in the second band loses so much energy that it will most probably end up in the lowest Bloch band. Therefore, as an approximation we can equalize the collision rate Γ from eq. (8.14) with the relaxation rate we get from the fit to our experimental data in figure 8.4, $\tau = (42 \pm 12)\,\mathrm{ms}$[1]. With an overlap integral of

$$\frac{1}{N} \int \mathrm{d}V \; n_{\mathrm{Na}}(x,y,z) n_{\mathrm{Li}}(x,y,z) = (20.1 \pm 2.3) \cdot 10^{17} \frac{1}{\mathrm{m}^3} \tag{8.21}$$

we finally get

$$|a_{BF}| = (70 \pm 12) a_0. \tag{8.22}$$

[1] It is important to note that this timescale τ is much larger than the $\sim 200\,\mu\mathrm{s}$ needed to transfer the atoms with a periodic lattice shaking from first to second Bloch band. This means that the transfer is not influenced by the relaxation dynamics and thus both processes can be safely considered as independent.

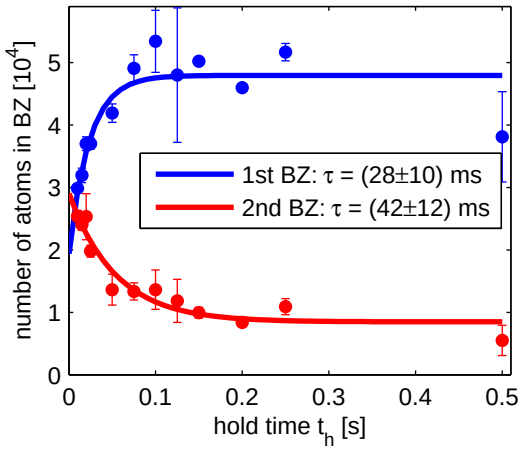

Figure 8.4.: *Relaxation of lithium $|1/2, 1/2\rangle$ atoms from second to first Bloch band induced by a sodium $|1, 1\rangle$ background. The time constants τ are obtained from an exponential fit to the data. τ is higher for the first than for the second Brillouin Zone due to an additional contribution of atoms relaxing from the third Bloch band. For long hold times $t_h \approx 0.5\,s$, an overall atom loss due to spontaneous processes is observed.*

As the whole measurement has been done for sodium in $|1, 1\rangle$ and lithium in $|1/2, 1/2\rangle$, a_{BF} is a linear combination of triplet and singlet scattering length, which are from the measurements in chapter 3 known to fulfil $|a_s - a_t| = (5.9 \pm 1.7)\, a_0$. This means that due to the large uncertainty in a_{BF} we can compare it directly to the result $|a_t| = (69 \pm 13) a_0$ from the oscillation damping measurement in chapter 5 and see that they show great agreement.

Finally, we want to discuss the systematic errors in the determination of a_{BF} presented above:

- Instead of considering the whole momentum distribution eq. (8.17) of atoms in the second Bloch band, for simplicity we take the rms momentum eq. (8.18) as a measure of the atoms' motion.

- Moreover, our result is obtained under the approximation that every interspecies scattering event leads to a relaxation of lithium from the second to the first Bloch band. A refined model has to involve e. g. also the energy spread of the atoms in the second band given by the two-dimensional Fermi energy due to the preparation process. This width has to be compared to the energy loss in a collision with the sodium background, since only collisions with an energy loss bigger than this width necessarily lead to a relaxation to the lower band. In the measurement presented above, we had a Fermi energy of $\sim$5 kHz and the lithium atoms' kinetic energy due to their confinement in the lattice was 30 kHz. If we assume s-wave scattering between sodium background and lithium atoms, we see that only $\sim$64% of the lithium atoms scatter at an angle which makes them lose more than the Fermi energy and thus relax to the lower band.

This additional prefactor leads to a 20% increase in the experimentally determined scattering length, which is within the given error bars.

Those two issues can be overcome by making use of Fermi's golden rule: One could integrate the whole momentum distribution eq. (8.17), while accounting for energy and momentum conservation by the appropriately chosen δ-distributions. This way, in principle the exact rate of atoms relaxing due to scattering events can be determined.

Some complications, which should have a minor effect on the result, arise due to the density distributions of the atoms:

- For the lithium, we use a Boltzmann instead of a (finite temperature) Fermi distribution, which seems well justified by their small differences depicted in figure 6.2. Indeed, using a $T = 0$ Fermi distribution for lithium changes our overlap integral eq. (8.21) by less than 5% and thus our result for a_{BF} by only 2%, which is way smaller than the statistical error of 17%.

- A small error stems from the fact that the effect of the lattice on sodium is not completely negligible. While the detuning is blue for lithium, the lattice is red detuned and $\sim 40\,\mathrm{nK}$ deep for sodium. Thus the condensate background density is reduced by about 4% on the lithium lattice sites, as one can show by integrating the GPE eq. (3.25) numerically with the ODT and SSODT potential inserted.

- Another effect on the density of sodium has the attractive interspecies interaction $a_{BF} < 0$, which enhances the sodium density at the lithium lattices sites. Even numerically calculating the resulting density profile of the Bose-Fermi mixture for a given $a_{BF} \neq 0$ is challenging on its own and would have to be done iteratively if – as in our case – the interspecies scattering length a_{BF} is unknown.

- For simplicity, we assumed the sodium atoms to be at rest and not to contribute to the velocity v in eq. (8.11). At least, sodium has a finite momentum due to occupying the harmonic oscillator states of the ODT, and additionally the small periodic potential from the SSODT increases their velocity v.

Also the dynamics of the decay process have been severely simplified:

- When the lithium relaxes, it transfers energy to the sodium atoms, which has to result in a decrease of the condensate fraction η, which we assumed to be constant throughout the relaxation process.

- In our derivation, the result for the relaxation rate eq. (8.15) is based on a Taylor approximation valid for $\Gamma t \ll 1$. Nevertheless, due to the insufficient number of data points for small times t, we use the entire experimentally measured relaxation curve to determine Γ.

- We cannot apply our model to data obtained at low temperatures, where the condensate fraction $\eta \to 1$. In this case, due to the insufficient overlap of the atomic density distributions (see figure 6.2) our model does not include the effect that the outer lattice sites are not covered by a bosonic background and thus the atoms there cannot relax, i. e. $\Gamma = 0$.

We see that there are still many more effects to be considered when trying to analyze the relaxation process of atoms from first to second Bloch band quantitatively. The model introduced here can at most serve as a starting point for future work. Despite all the approximations, the result for the scattering length fits the value obtained by the CC calculation well.

8.5. Rabi Oscillations

Finally, we want to show the coherent character of the excitations induced by the periodic shaking. For that purpose, we excite Rabi oscillations, i. e. monitor the oscillatory evolution of atom number in first and second Bloch band. The Rabi freqeuncy Ω is as usual defined via the relation

$$\langle e|H'(x,t)|g\rangle = H_{eg} \equiv \hbar\Omega \sin(\omega_{ex} t)\,. \tag{8.23}$$

With eq. (8.10) we thus get

$$\hbar\Omega = 2V_0(kx_0)\,\langle e|kx|g\rangle = \sqrt{2}V_0(kx_0)(ka_{\mathrm{ho}})\,, \tag{8.24}$$

where $a_{\mathrm{ho}} = \sqrt{\hbar/m\omega}$ denotes the harmonic oscillator length. For the evaluation of the dipole matrix element $\langle e|x|g\rangle$, we have applied the approximation for deep lattices and used the harmonic oscillator wavefunctions to be able to calculate analytic results.

Experimentally, we excite Rabi oscillations by applying a periodic shaking of the lattice at resonance frequency $\omega_{ex} = \omega$ with fixed amplitude x_0 and variable duration. As to be seen in figure 8.5, we obtain a damped sinusoidal oscillation between first and second Bloch band, which we can fit to deduce the Rabi frequency $\Omega/2\pi = (3.58 \pm 0.03)\,\mathrm{kHz}$. With $\omega/2\pi = 47.5\,\mathrm{kHz}$ and an excitation amplitude $x_0 = 14.5\,\mathrm{nm}$, the theoretical prediction eq. (8.24) yields $\Omega/2\pi = 3.77\,\mathrm{kHz}$, i. e. it does not yet agree with the experimental observation.

As a possible source of the deviation, we identify the approximation done in the derivation of eq. (8.10). There we just did a Taylor expansion up to first order in kx, but in the measurement presented above, $ka_{\mathrm{ho}} = 0.54$ and thus the higher order terms can not be neglected. Including the next orders as well[2] we get

$$H'(x,t) = 2V_0(kx_0)(kx - \frac{2}{3}(kx)^3)\sin(\omega_{\mathrm{ex}} t)\,. \tag{8.25}$$

[2]We only include terms oscillating at frequency ω_{ex} and disregard higher orders. This is the rotating wave approximation, which is valid as long as the detuning is small, i. e. $|\delta| = |\omega_{\mathrm{ex}} - \omega| \ll \omega_{\mathrm{ex}}$.

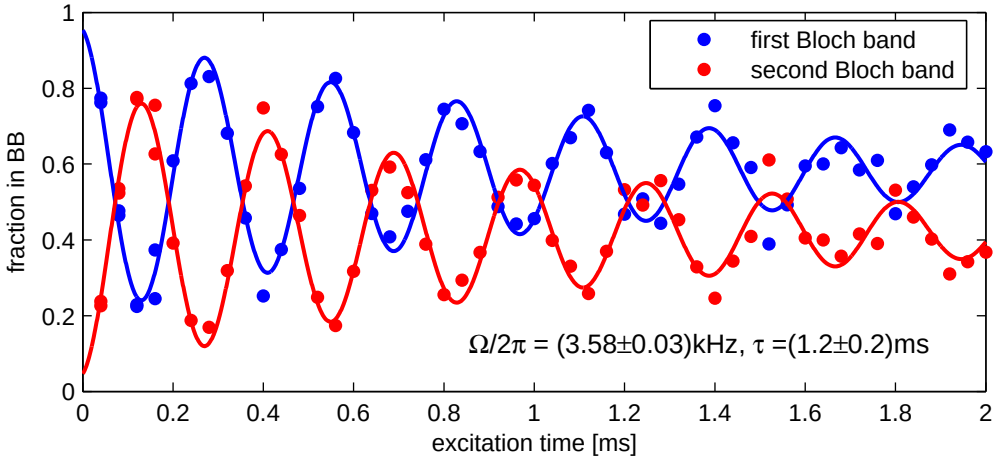

Figure 8.5.: *Rabi oscillations between first and second Bloch band. The periodic displacement of the lattice was applied with a frequency* $\omega_{\mathrm{ex}}/2\pi = 47.5\,\mathrm{kHz}$ *and an amplitude* $x_0 = 14.5\,\mathrm{nm}$*. The experimental data (dots) are fitted with a damped sinusoidal (solid lines), yielding a Rabi frequency of* $\Omega/2\pi = (3.58 \pm 0.03)\,\mathrm{kHz}$*.*

The Rabi frequency including the energy correction reads

$$\hbar\Omega = 2V_0(kx_0)(k\,\langle e|kx|g\rangle - \frac{2}{3}\,\langle e|(kx)^3|g\rangle) = \sqrt{2}V_0(kx_0)(ka_{\mathrm{ho}} - (ka_{\mathrm{ho}})^3)\,. \tag{8.26}$$

The resulting new theoretically predicted Rabi frequency of $\Omega = 2.69\,\mathrm{kHz}$ even deviates more from the experimentally obtained value. Thus a more elaborate theory, which e. g. involves Wannier functions instead of harmonic oscillator wavefunctions, is needed to understand the observed Rabi oscillations quantitatively.

In this chapter, we have studied excitations in the optical lattice. A quantum mechanical picture of spatial oscillations has been developed and the interspecies energy transfer from oscillating lithium atoms to a condensed sodium background has been analyzed quantitatively. By periodically displacing the lattice, we are able to excite lithium atoms from first to second Bloch band in a controlled way, which has enabled us to get a measure of the interspecies scattering length a_{IB} by analyzing the subsequent relaxation induced by a bosonic background. Finally, the coherence of the excitations has been proven by exciting Rabi oscillations, which could be explained in time-dependent perturbation theory. In the Outlook, we will further elucidate which physics can be explored with the presented tools at hand.

9. Conclusion and Outlook

Das, was hinter dir liegt, hast du erlebt, was vor dir liegt, ist unbekannt. Das mag verunsichernd sein, macht es aber auch interessant.

Walter Bonatti

With this thesis, we paved the way to measure polarons in ultracold atom systems, in particular in the Bose-Fermi mixture of sodium and lithium. For that purpose, we analyzed the tuning parameters in detail and developed possible detection schemes for an increased effective mass m^*. As outlined in the introduction, there are in principle two ways to change the coupling parameter α, which characterizes the polaron: On the one hand, one can vary the background intraspecies interaction a_{BB}, on the other hand the dependence on a_{IB} is even stronger.

In our experiments, the background is formed by a condensate of sodium, whose scattering properties were already known to a good accuracy before the Heidelberg experiment started. With our measurements of the sodium Feshbach resonance spectrum, we gave valuable input to a coupled-channels calculation, which improved the accuracy of the last bound triplet state in the NaNa-potential by a factor of 50. Moreover, the refined model provides us with a reliable prediction of the width of the 1202.6 G resonance, $\Delta = -1.473\,\mathrm{G}$, making it well suited for tuning a_{BB}.

To determine a_{IB} and analyze its tuning properties, we had to spend a higher effort. A general procedure, which can be applied to any combination of atoms with unknown interspecies scattering properties, has been developed and tested by means of the sodium-lithium mixture. The difference between singlet and triplet scattering length can be determined via a loss measurement, whereas for obtaining the absolute value of the scattering length we presented two different procedures, which yielded the same result. With this at hand, we could set limits to the s-wave bound state energy and thus develop a model explaining all 26 Feshbach resonances, which were measured in the course of this thesis. Most of them turned out to have d-wave character, and a coupled-channels approach yielded as largest width $\Delta = 10\,\mathrm{mG}$, which is not suited for tuning a_{IB}. In agreement with our experimental results,

the background scattering length was theoretically calculated to be $a_{IB} = -(75 \pm 5)a_0$, being in its absolute value a factor of five higher than previously assumed.

For measuring the polaron effective mass m^*, we have implemented a species selective optical dipole trap in form of an optical lattice. Without further effort, we were able to determine the lithium oscillation frequency with a relative accuracy of better than 0.5%, which brings a measurement of the polaron effective mass in our system within reach. Moreover, with the tool of Brillouin zone mapping, we are able to analyze excitations in the lattice. Rabi oscillations induced by a periodic lattice shaking were analyzed this way, which paves the way to a wealth of interesting physics, as will be outlined in the following.

Outlook

As already to be seen in the last chapter in figure 8.5, the Rabi oscillation damps out on a time scale of about 2 ms. This behaviour can be caused by both dephasing and decoherence, but by implementing an appropriate spin-echo experiment one could extract the T_2-time, a well-known measure to characterize decoherence processes in NMR [115]. This timescale can be related to the T_1-time, which we have measured as the time constant of lithium relaxation from second to first Bloch band: If $T_2 = T_1/2$, which is e. g. the case for a two-level atom with spontaneous emission [112], our bath is Markovian, i. e. has no memory. In our experimental situation of a trapped BEC as background, it is not a priori clear if the system is Markovian, as the phonons, which carry the energy resulting from the relaxation of the two-level system, do not simply vanish as the photons in the case of spontaneous emission.

But even the precise investigation of the relaxation dynamics of the two-level system can give some deeper insight into the underlying physics: If the process would prove to be non-exponential, i. e. follow a power-law, this could be caused by an energy-dependent relaxation rate as expected if correlations in the bath build up.

We see that investigating thermodynamic processes in our system could reveal a lot of interesting physics. With a controlled local heat input on the lithium, one could try and see collisionless superfluid internal convection in the sodium condensate, an effect which has been theoretically predicted recently [116].

The geometry of our species selective optical dipole trap, being realized as an optical lattice, also provides us with the possibility to study lower-dimensional systems. It has been shown that in this case the amplitude of possible polaronic features is enhanced [117], which facilitates the experimental observation. Moreover, the use of confinement-induced resonances in the low-dimensional system [118] provides a possibility to tune the polaronic coupling strength α.

Recently, pairing of fermions in a two-dimensional configuration [119] and its evolution from two to three dimensions [96] has been studied experimentally, but the properties of

the Fermi polaron in 2D has so far only been investigated theoretically [120]. The interlayer coupling model of high-T_c superconductivity [121], which attributes an enhancement of superconductivity due to coupling between the two-dimensional layers, could be realized in our system by allowing for a finite tunneling coupling between the different lattice sites.

Following a more complex proposal [122], one could also explore the rich phase diagram of a Bose-Fermi mixture with both gases being confined to one dimension, after the lattice setup has been extended appropriately.

Whereas the last experiments outlined are rather goals to pursue in the far future, measuring an increase in polaron effective mass m^* in our setup is feasible under the current conditions: By tuning a_{BB} with a Feshbach resonance, we can bring the coupling parameter α in a regime, where the resulting increase in effective mass m^* can be detected via a shift in oscillation frequency.

A. List of Constants

The following table gives the values and abbreviations of constants used in this thesis. The species specific constants have been taken from [123] and [124] for sodium and lithium, respectively.

symbol	constant	value
a_0	Bohr radius	$5.29177249 \cdot 10^{-11}\,\mathrm{m}$
$\hbar$	Planck constant	$1.05457266 \cdot 10^{-34}\,\mathrm{Js}$
h	Planck constant	$\hbar \cdot 2\pi$
k_B	Boltzmann constant	$1.380658 \cdot 10^{-23}\,\mathrm{J/K}$
μ_B	Bohr magneton	$9.2740154 \cdot 10^{-24}\,\mathrm{J/T}$
c	Speed of light	$299{,}792{,}458\,\mathrm{m/s}$
μ_0	magnetic constant	$4\pi \cdot 10^{-7}\,\mathrm{H/m}$
	Sodium-specific constants	
m_{Na}	mass	$3.81754035 \cdot 10^{-26}\,\mathrm{kg}$
ω_{Na}	D_2-line transition frequency	$2\pi \cdot 508.8487162\,\mathrm{THz}$
Γ_{Na}	Natural linewidth	$2\pi \cdot 9.7946\,\mathrm{MHz}$
$a_{\mathrm{hfs}}^{\mathrm{Na}}$	hyperfine constant	$885.81306440\,\mathrm{MHz}$
g_s	Electron spin g-factor	2.0023193043622
i^{Na}	nuclear spin	3/2
g_i^{Na}	nuclear g-factor	-0.00080461080
	Lithium-specific constants	
m_{Li}	mass	$9.9883414 \cdot 10^{-27}\,\mathrm{kg}$
ω_{Li}	D_2-line transition frequency	$2\pi \cdot 446.799677\,\mathrm{THz}$
Γ_{Li}	Natural linewidth	$2\pi \cdot 5.8724\,\mathrm{MHz}$
$a_{\mathrm{hfs}}^{\mathrm{Li}}$	hyperfine constant	$152.1368407\,\mathrm{MHz}$
g_s	Electron spin g-factor	2.0023193043622
i^{Li}	nuclear spin	1
g_i^{Li}	nuclear g-factor	-0.000447654

B. All NaLi Resonance Data

In the following, all NaLi resonances measured in the different spin channels are shown. All pictures were taken in an ODT with ω usw. , a temperature of $T \approx 1\mu$K and atom numbers of $N_{\mathrm{Na}} \approx 10^6$ and $N_{\mathrm{Li}} \approx 10^5$. Each loss curve is fitted with a Gaussian, which is shown as solid line. The averaged lithium atom numbers with their statistical errors plotted on the y-axis are normalized, the magnetic field [G] is the x-axis of each graph, inside which four parameters characterizing the resonance are shown:

- B_0: The resonance position
- ΔB: The $1/e^2$ half width of the fit to the resonance data
- τ: The hold time calculated from an exponential fit to the atom loss curve on resonance
- Δ: The theoretical resonance width from a coupled channels calculation

d-wave resonances are plotted in red and s-wave resonances in blue.

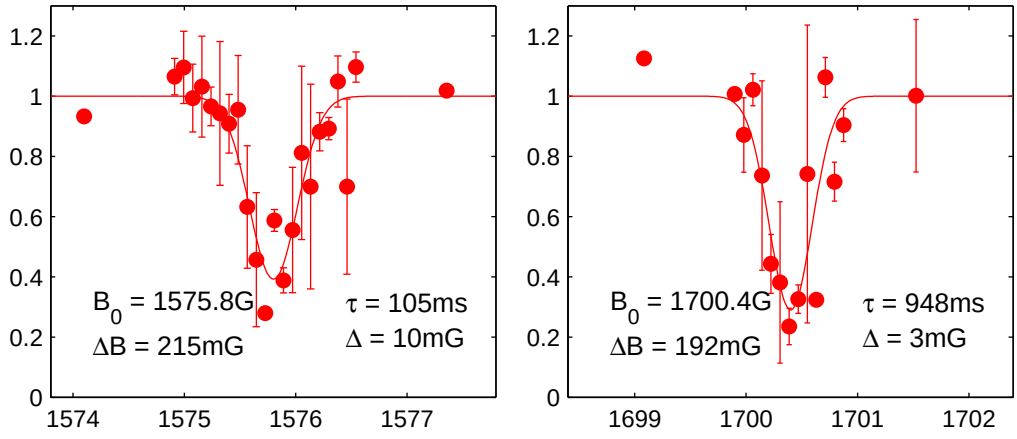

Figure B.1.: *$M_F = 5/2$, $\mathrm{Li}\,|3/2, 3/2\rangle + \mathrm{Na}\,|1, 1\rangle$ Feshbach resonances.*

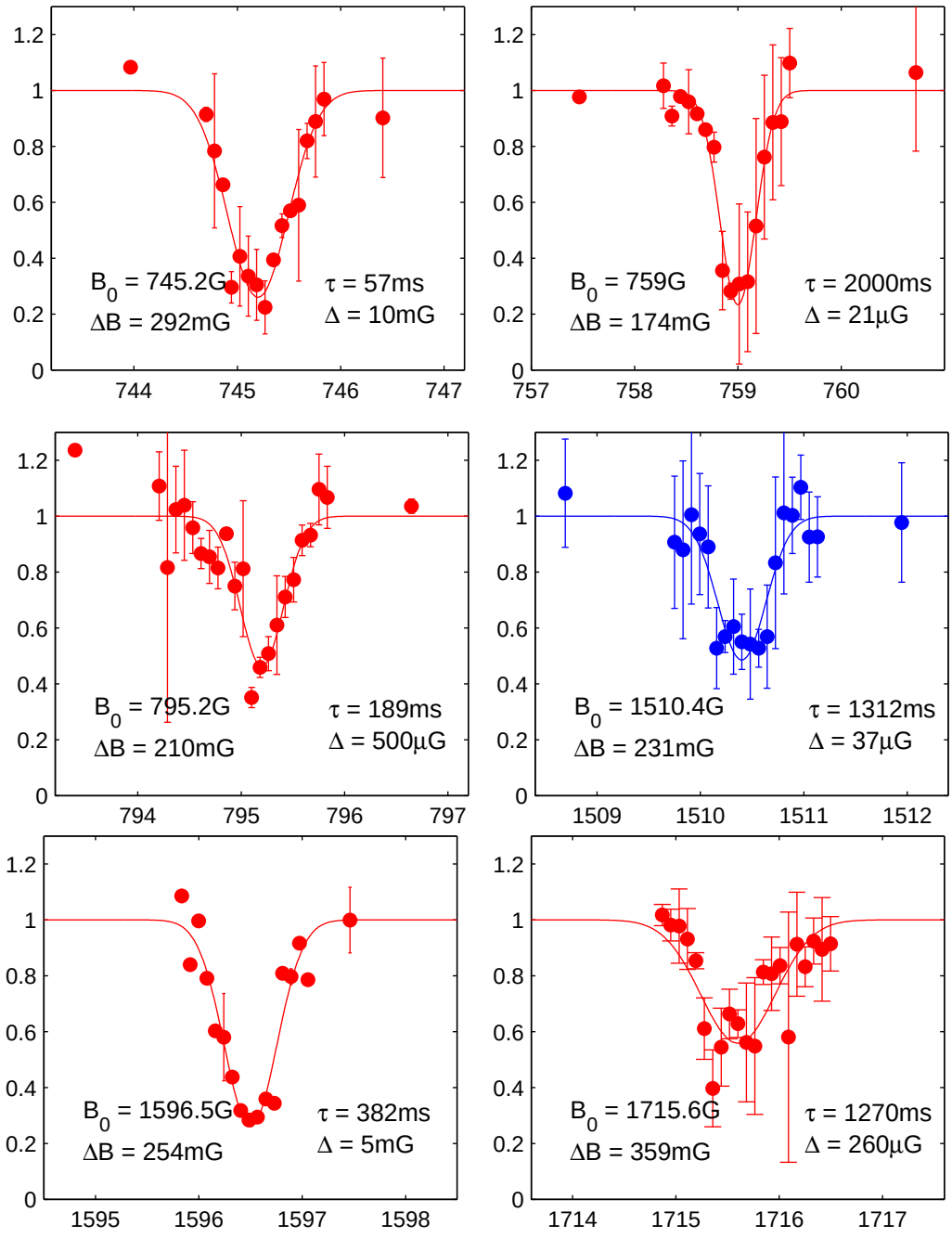

Figure B.2.: *$M_F = 3/2$, $\mathrm{Li}\,|1/2, 1/2\rangle + \mathrm{Na}\,|1, 1\rangle$ Feshbach resonances (I).*

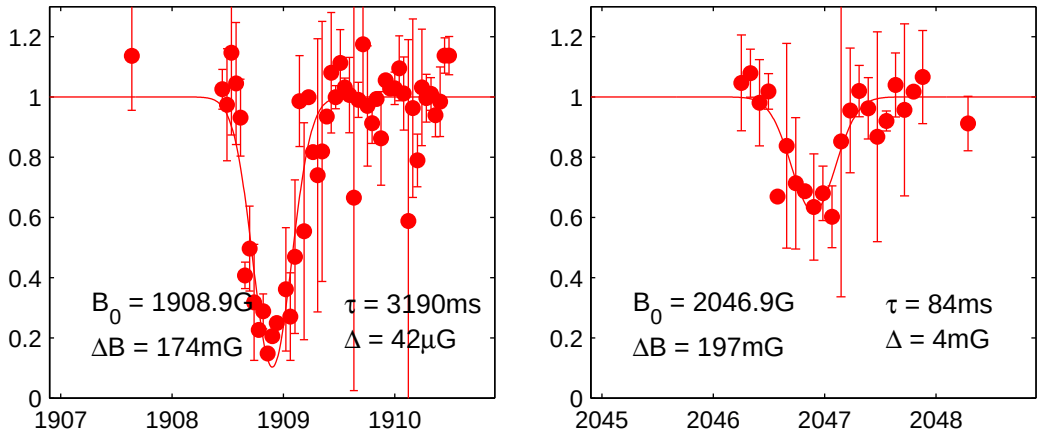

Figure B.3.: *$M_F = 3/2$, $\mathrm{Li}\,|1/2, 1/2\rangle + \mathrm{Na}\,|1, 1\rangle$ Feshbach resonances (II).*

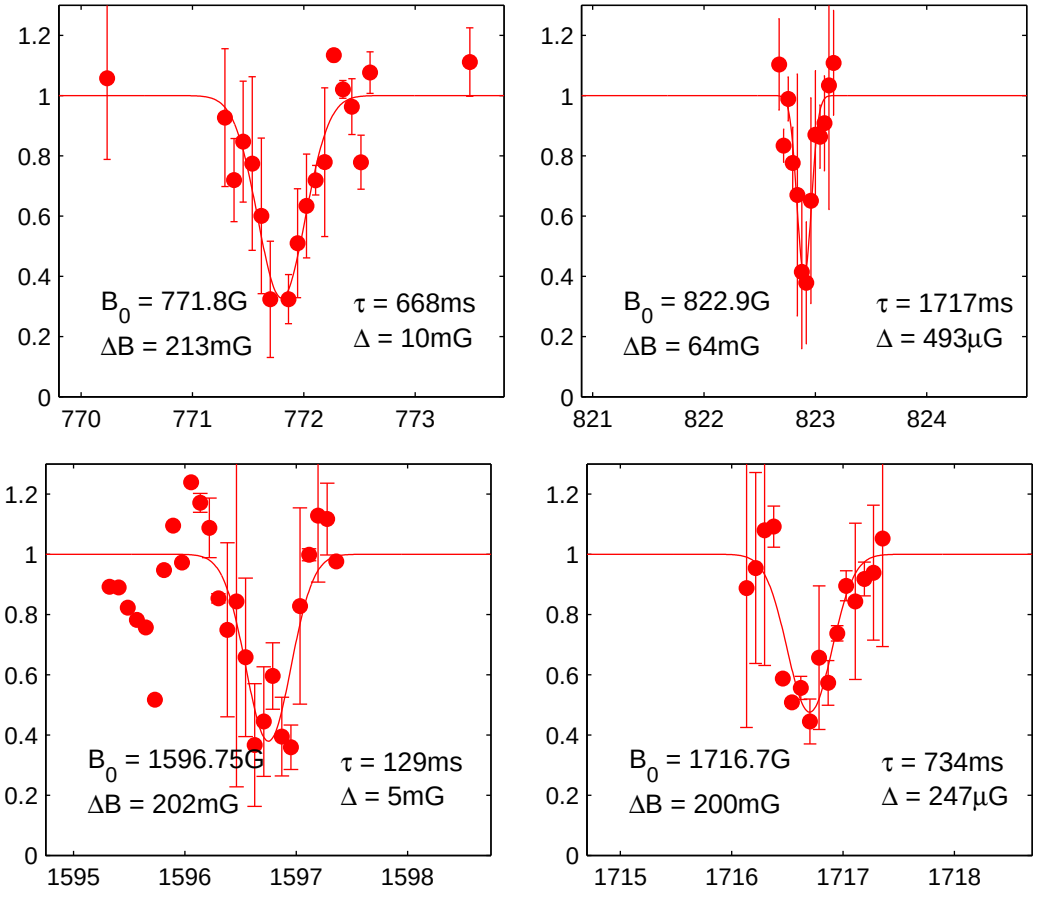

Figure B.4.: *$M_F = 1/2$, $\mathrm{Li}\,|1/2, -1/2\rangle + \mathrm{Na}\,|1, 1\rangle$ Feshbach resonances.*

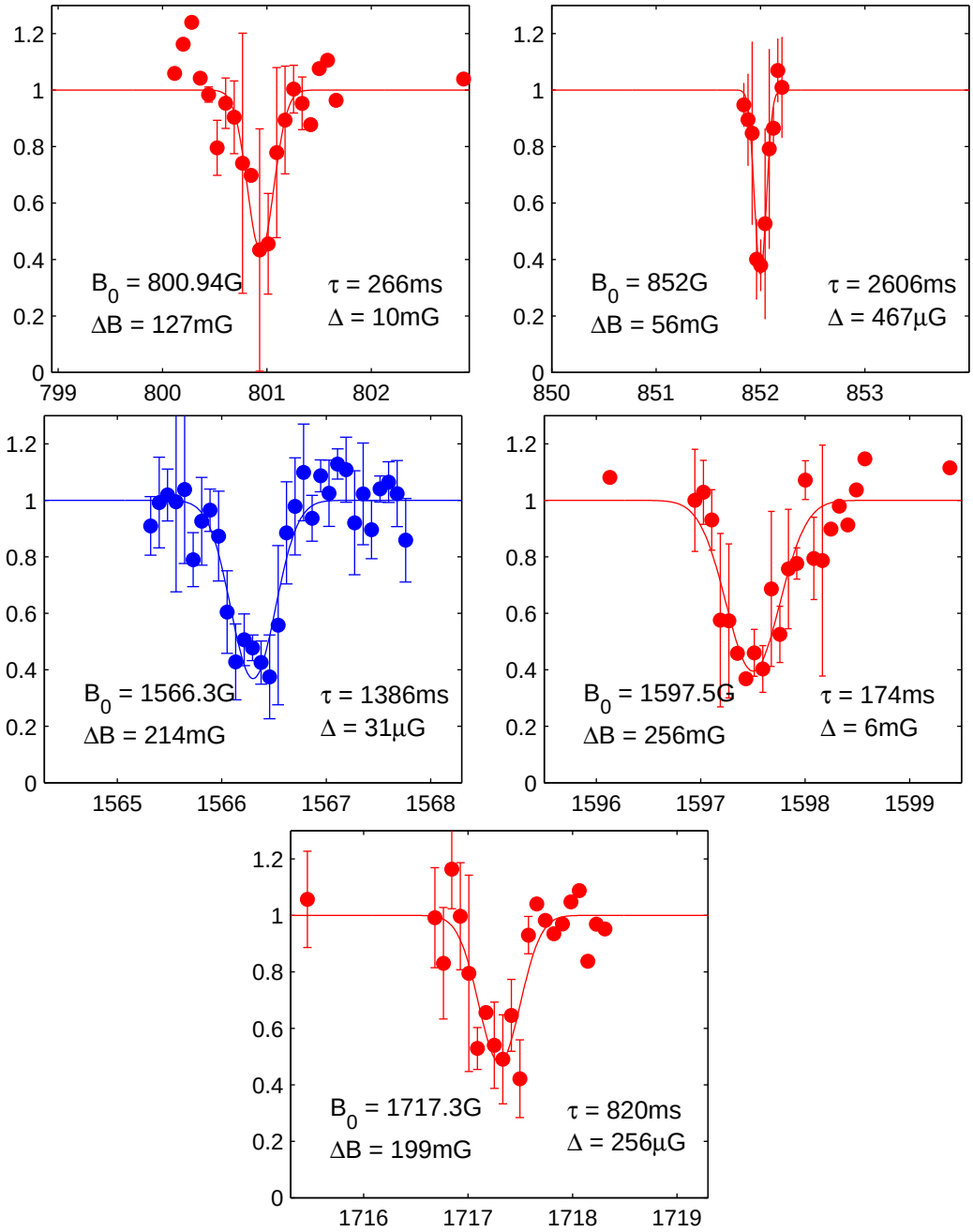

Figure B.5.: *$M_F = -1/2$, $\mathrm{Li}\,|3/2,-3/2\rangle + \mathrm{Na}\,|1,1\rangle$ Feshbach resonances.*

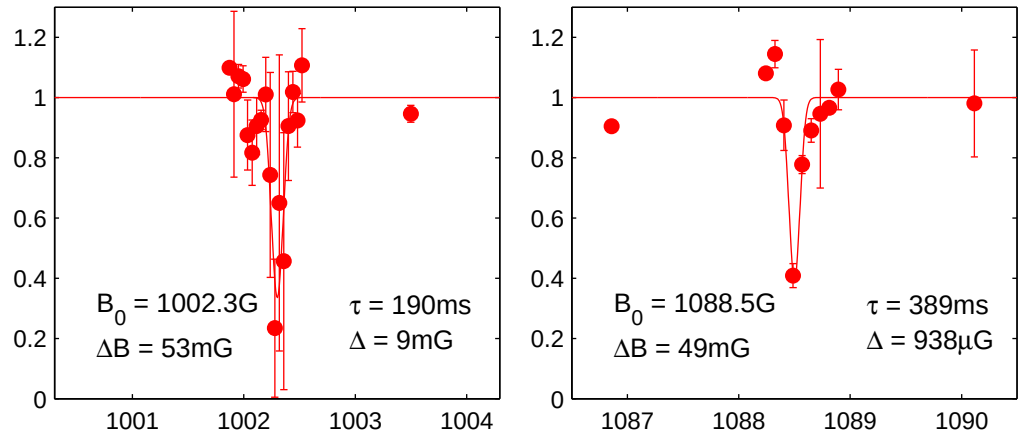

Figure B.6.: *$M_F = -1/2$,* $\mathrm{Li}\,|1/2, 1/2\rangle + \mathrm{Na}\,|1, -1\rangle$ *Feshbach resonances.*

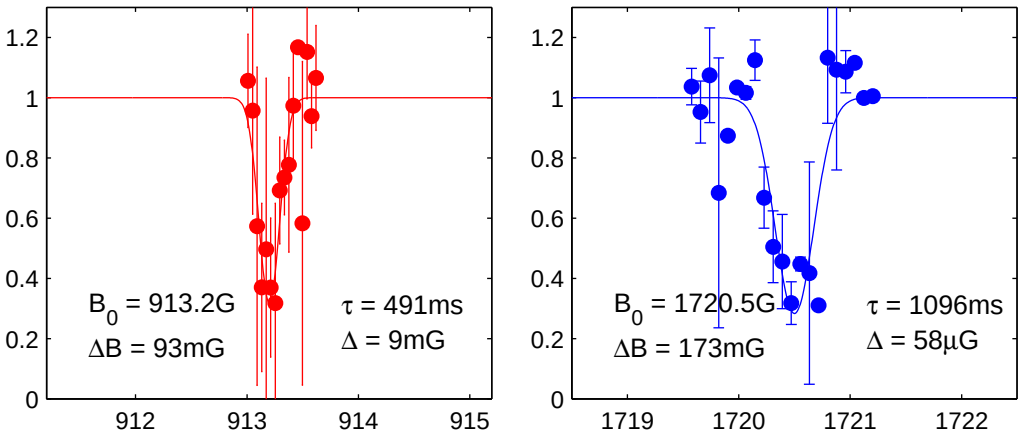

Figure B.7.: *$M_F = -3/2$,* $\mathrm{Li}\,|3/2, -3/2\rangle + \mathrm{Na}\,|1, 0\rangle$ *Feshbach resonances.*

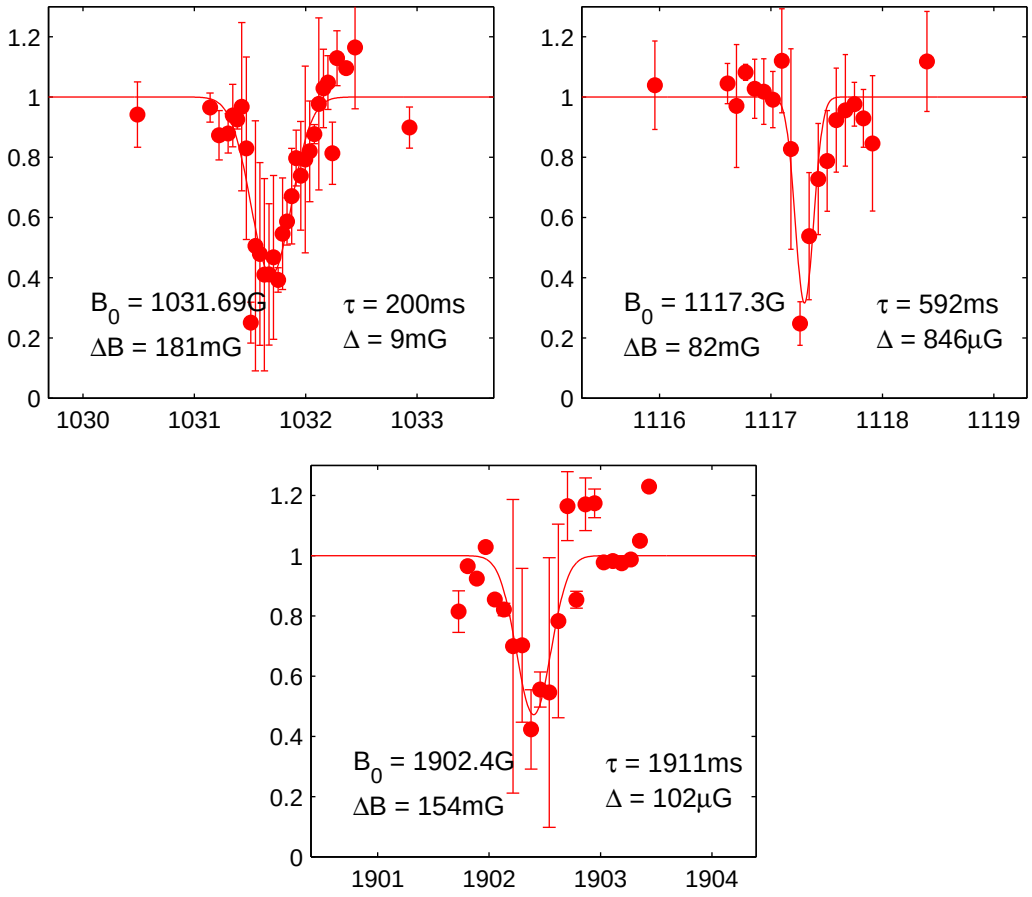

Figure B.8.: $M_F = -3/2$, $\mathrm{Li}\,|1/2,-1/2\rangle + \mathrm{Na}\,|1,-1\rangle$ *Feshbach resonances.*

Bibliography

[1] M. H. Anderson, J. R. Ensher, M. R. Matthews, C. E. Wieman, and E. A. Cornell. Observation of Bose-Einstein Condensation in a Dilute Atomic Vapor. *Science*, 269(5221):198–201, 1995.

[2] K. B. Davis, M. O. Mewes, M. R. Andrews, N. J. van Druten, D. S. Durfee, D. M. Kurn, and W. Ketterle. Bose-Einstein Condensation in a Gas of Sodium Atoms. *Phys. Rev. Lett.*, 75:3969–3973, 1995.

[3] I. Bloch, J. Dalibard, and W. Zwerger. Many-body physics with ultracold gases. *Rev. Mod. Phys.*, 80:885–964, 2008.

[4] S. Inouye, M. R. Andrews, J. Stenger, H.-J. Miesner, D. M. Stamper-Kurn, and W. Ketterle. Observation of Feshbach resonances in a Bose-Einstein condensate. *Nature*, 392:151–154, 1998.

[5] C. Chin, R. Grimm, P. Julienne, and E. Tiesinga. Feshbach resonances in ultracold gases. *Rev. Mod. Phys.*, 82:1225–1286, 2010.

[6] M. Greiner, O. Mandel, T. Esslinger, T. W. Hänsch, and I. Bloch. Quantum phase transition from a superfluid to a Mott insulator in a gas of ultracold atoms. *Nature*, 415:39–44, 2002.

[7] T. Kinoshita, T. Wenger, and D. S. Weiss. Observation of a One-Dimensional Tonks-Girardeau Gas. *Science*, 305(5687):1125–1128, 2004.

[8] Z. Hadzibabic, P. Krüger, M. Cheneau, B. Battelier, and J. Dalibard. Berezinskii-Kosterlitz-Thouless crossover in a trapped atomic gas. *Nature*, 441:1118–1121, 2006.

[9] R. P. Feynman. Simulating physics with computers. *Int. J. Theor. Phys*, 21:467–488, 1982.

[10] J. Bardeen, L. N. Cooper, and J. R. Schrieffer. Theory of Superconductivity. *Phys. Rev.*, 108:1175–1204, 1957.

[11] M. W. Zwierlein, J. R. Abo-Shaeer, A. Schirotzek, C. H. Schunck, and W. Ketterle. Vortices and superfluidity in a strongly interacting Fermi gas. *Nature*, 435:1047–1051, 2005.

[12] M. W. Zwierlein, C. H. Schunck, A. Schirotzek, and W. Ketterle. Direct observation of the superfluid phase transition in ultracold Fermi gases. *Nature*, 442:54–58, 2006.

[13] A. M. Clogston. Upper Limit for the Critical Field in Hard Superconductors. *Phys. Rev. Lett.*, 9:266–267, 1962.

[14] B.S. Chandrasekhar. A note on the maximum critical field of high-field superconductors. *Appl. Phys. Lett.*, 1:7–8, 1962.

[15] M. W. Zwierlein, A. Schirotzek, C. H. Schunck, and W. Ketterle. Fermionic Superfluidity with Imbalanced Spin Populations. *Science*, 311(5760):492–496, 2006.

[16] A. Schirotzek, C.-H. Wu, A. Sommer, and M. W. Zwierlein. Observation of Fermi Polarons in a Tunable Fermi Liquid of Ultracold Atoms. *Phys. Rev. Lett.*, 102:230402, 2009.

[17] S. Nascimbène, N. Navon, K. J. Jiang, L. Tarruell, M. Teichmann, J. McKeever, F. Chevy, and C. Salomon. Collective Oscillations of an Imbalanced Fermi Gas: Axial Compression Modes and Polaron Effective Mass. *Phys. Rev. Lett.*, 103:170402, 2009.

[18] C. Kohstall, M. Zaccanti, M. Jag, A. Trenkwalder, P. Massignan, G. M. Bruun, F. Schreck, and R. Grimm. Metastability and Coherence of Repulsive Polarons in a Strongly Interacting Fermi Mixture. *ArXiv*:1112.0020, 2011.

[19] L. D. Landau. Über die Bewegung der Elektronen in Kristalgitter. *Phys. Z. Sowjetunion*, 3:644–645, 1933.

[20] F. M. Cucchietti and E. Timmermans. Strong-Coupling Polarons in Dilute Gas Bose-Einstein Condensates. *Phys. Rev. Lett.*, 96:210401, 2006.

[21] J. Tempere, W. Casteels, M. K. Oberthaler, S. Knoop, E. Timmermans, and J. T. Devreese. Feynman path-integral treatment of the BEC-impurity polaron. *Phys. Rev. B*, 80:184504, 2009.

[22] Stefan Maier. *Effect of electron-phonon interaction in nanostructures and ultracold quantum gases*. PhD thesis, Universität Heidelberg, 2011.

[23] V. Z. Kresin and S. A. Wolf. *Colloquium*: Electron-lattice interaction and its impact on high T_c superconductivity. *Rev. Mod. Phys.*, 81:481–501, 2009.

[24] J. Catani, G. Lamporesi, D. Naik, M. Gring, M. Inguscio, F. Minardi, A. Kantian, and T. Giamarchi. Quantum dynamics of impurities in a one-dimensional Bose gas. *Phys. Rev. A*, 85:023623, 2012.

[25] E. M. Lifschitz L. D. Landau. *Quantenmechanik*. Akademie-Verlag Berlin, 1979.

[26] S. Knoop, T. Schuster, R. Scelle, A. Trautmann, J. Appmeier, M. K. Oberthaler, E. Tiesinga, and E. Tiemann. Feshbach spectroscopy and analysis of the interaction potentials of ultracold sodium. *Phys. Rev. A*, 83:042704, 2011.

[27] W. Ketterle, D. S. Durfee, and D. M. Stamper-Kurn. Making, probing and understanding Bose-Einstein condensates. In *Bose-Einstein condensation in atomic gases, Proceedings of the International School of Physics "Enrico Fermi", Course CXL, edited by M. Inguscio, S. Stringari and C.E. Wieman*. IOS Press, Amsterdam, 1999.

[28] F. Schwabl. *Quantenmechanik*. Springer, Berlin, 2004.

[29] T. Koch, T. Lahaye, J. Metz, B. Fröhlich, A. Griesmaier, and T. Pfau. Stabilization of a purely dipolar quantum gas against collapse. *Nature Physics*, 4:218–222, 2008.

[30] K.-K. Ni, S. Ospelkaus, D. Wang, G. Quemener, B. Neyenhuis, M. H. G. de Miranda, J. L. Bohn, J. Ye, and D. S. Jin. Dipolar collisions of polar molecules in the quantum regime. *Nature*, 464:1324–1328, 2010.

[31] L. P. Pitaevskii and S. Stringari. *Bose-Einstein Condensation*. Oxford University Press, 2003.

[32] H. Feshbach. Unified theory of nuclear reactions. *Annals of Physics*, 5(4):357–390, 1958.

[33] U. Fano. Effects of Configuration Interaction on Intensities and Phase Shifts. *Phys. Rev.*, 124:1866–1878, 1961.

[34] Marc Repp. Aufbau einer Vakuumapparatur für Experimente mit ultrakalten fermionischen und bosonischen Quantengasen. Master's thesis, Universität Heidelberg, 2007.

[35] Stefan Weis. Setup of a Laser System for Ultracold Sodium - Towards a Degenerate Gas of Ultracold Fermions. Master's thesis, Universität Heidelberg, 2007.

[36] Jan Krieger. Zeeman-Slower und Experimentsteuerung für das NaLi-Experiment. Master's thesis, Universität Heidelberg, 2008.

[37] Jens Appmeier. *Immersed Quantum Systems: A Sodium Bose-Einstein Condensate for Polaron Studies*. PhD thesis, Universität Heidelberg, 2010.

[38] Arno Trautmann. Feshbach Spectroscopy of Sodium and Sodium-Lithium Mixtures. Master's thesis, Universität Heidelberg, 2011.

[39] B. H. Bransden and Charles J. Joachain. *Physics of Atoms and Molecules*. Longman, 1982.

[40] A. Wachter and H. Hober. *Repetitorium Theoretische Physik*. Springer, 2005.

[41] G. Breit and I. I. Rabi. Measurement of Nuclear Spin. *Phys. Rev.*, 38:2082–2083, 1931.

[42] Z. Hadzibabic, C. A. Stan, K. Dieckmann, S. Gupta, M. W. Zwierlein, A. Görlitz, and W. Ketterle. Two-Species Mixture of Quantum Degenerate Bose and Fermi Gases. *Phys. Rev. Lett.*, 88:160401, 2002.

[43] Z. Hadzibabic, S. Gupta, C. A. Stan, C. H. Schunck, M. W. Zwierlein, K. Dieckmann, and W. Ketterle. Fiftyfold Improvement in the Number of Quantum Degenerate Fermionic Atoms. *Phys. Rev. Lett.*, 91:160401, 2003.

[44] Raphael Scelle. Cooling, Plugging, Trapping: Exploiting Optical Dipole Potentials For Polaron Experiments. Master's thesis, Universität Heidelberg, 2009.

[45] A. Görlitz, T. L. Gustavson, A. E. Leanhardt, R. Löw, A. P. Chikkatur, S. Gupta, S. Inouye, D. E. Pritchard, and W. Ketterle. Sodium Bose-Einstein Condensates in the $F = 2$ State in a Large-Volume Optical Trap. *Phys. Rev. Lett.*, 90:090401, 2003.

[46] H. J. Metcalf and P. van der Straten. *Laser Cooling and Trapping*. Springer (New York), 1999.

[47] L. D. Landau. Zur Theorie der Energieübertragung. II. *Physics of the Soviet Union*, 2:46–51, 1932.

[48] Christian Groß. *Spin squeezing and non-linear atom interferometry with Bose-Einstein condensates*. PhD thesis, Universität Heidelberg, 2010.

[49] D. J. Papoular, G. V. Shlyapnikov, and J. Dalibard. Microwave-induced Fano-Feshbach resonances. *Phys. Rev. A*, 81:041603, 2010.

[50] C.J. Pethick and H. Smith. *Bose-Einstein Condensation in Dilute Gases*. Cambridge University Press, 2004.

[51] E. Tiesinga, B. J. Verhaar, and H. T. C. Stoof. Threshold and resonance phenomena in ultracold ground-state collisions. *Phys. Rev. A*, 47:4114–4122, 1993.

[52] P. O. Fedichev, M. W. Reynolds, and G. V. Shlyapnikov. Three-Body Recombination of Ultracold Atoms to a Weakly Bound s Level. *Phys. Rev. Lett.*, 77:2921–2924, 1996.

[53] T. Kraemer, M. Mark, P. Waldburger, J. G. Danzl, C. Chin, B. Engeser, A. D. Lange, K. Pilch, A. Jaakkola, H.-C. Naegerl, and R. Grimm. Evidence for Efimov quantum states in an ultracold gas of cesium atoms. *Nature*, 440:315–318, 2006.

[54] E.P. Gross. Structure of a quantized vortex in boson systems. *Il Nuovo Cimento*, 20:454–457, 1961.

[55] L.P. Pitaevskii. Vortex Lines in an Imperfect Bose Gas. *Soviet Physics JETP*, 13:451–454, 1961.

[56] M. Holland and J. Cooper. Expansion of a Bose-Einstein condensate in a harmonic potential. *Phys. Rev. A*, 53:R1954–R1957, 1996.

[57] T. Weber, J. Herbig, M. Mark, H.-C. Nägerl, and R. Grimm. Three-Body Recombination at Large Scattering Lengths in an Ultracold Atomic Gas. *Phys. Rev. Lett.*, 91:123201, 2003.

[58] J. Zhang, E. G. M. van Kempen, T. Bourdel, L. Khaykovich, J. Cubizolles, F. Chevy, M. Teichmann, L. Tarruell, S. J. J. M. F. Kokkelmans, and C. Salomon. *P*-wave Feshbach resonances of ultracold ^{6}Li. *Phys. Rev. A*, 70:030702, 2004.

[59] C. H. Schunck, M. W. Zwierlein, C. A. Stan, S. M. F. Raupach, W. Ketterle, A. Simoni, E. Tiesinga, C. J. Williams, and P. S. Julienne. Feshbach resonances in fermionic ^{6}Li. *Phys. Rev. A*, 71:045601, 2005.

[60] Ch. Lisdat, O. Dulieu, H. Knöckel, and E. Tiemann. Inversion analysis of **K2** coupled electronic states with the Fourier grid method. *EPJ D*, 17:319–328, 2001.

[61] A. J. Moerdijk, B. J. Verhaar, and A. Axelsson. Resonances in ultracold collisions of ^{6}Li, ^{7}Li, and ^{23}Na. *Phys. Rev. A*, 51:4852–4861, 1995.

[62] T. G. Tiecke, M. R. Goosen, J. T. M. Walraven, and S. J. J. M. F. Kokkelmans. Asymptotic-bound-state model for Feshbach resonances. *Phys. Rev. A*, 82:042712, 2010.

[63] T. Laue, E. Tiesinga, C. Samuelis, H. Knöckel, and E. Tiemann. Magnetic-field imaging of weakly bound levels of the ground-state Na_2 dimer. *Phys. Rev. A*, 65:023412, 2002.

[64] E. Wille, F. M. Spiegelhalder, G. Kerner, D. Naik, A. Trenkwalder, G. Hendl, F. Schreck, R. Grimm, T. G. Tiecke, J. T. M. Walraven, S. J. J. M. F. Kokkelmans, E. Tiesinga, and P. S. Julienne. Exploring an Ultracold Fermi-Fermi Mixture: Interspecies Feshbach Resonances and Scattering Properties of ^{6}Li and ^{40}K. *Phys. Rev. Lett.*, 100:053201, 2008.

[65] J. T. M. Walraven. Elements of Quantum Gases: Thermodynamic and Collisional Properties of Trapped Atomic Gases. 2010.

[66] J. Stenger, S. Inouye, M. R. Andrews, H.-J. Miesner, D. M. Stamper-Kurn, and W. Ketterle. Strongly Enhanced Inelastic Collisions in a Bose-Einstein Condensate near Feshbach Resonances. *Phys. Rev. Lett.*, 82:2422–2425, 1999.

[67] L. E. E. de Araujo, J. D. Weinstein, S. D. Gensemer, F. K. Fatemi, K. M. Jones, P. D. Lett, and E. Tiesinga. Two-color photoassociation spectroscopy of the lowest triplet potential of Na_2. *J. Chem. Phys.*, 119:2062, 2003.

[68] E. Tiemann. Width of the Sodium 1202.6 G Resonance. Private Communication, 2011.

[69] C. Samuelis, E. Tiesinga, T. Laue, M. Elbs, H. Knöckel, and E. Tiemann. Cold atomic collisions studied by molecular spectroscopy. *Phys. Rev. A*, 63:012710, 2000.

[70] M. Elbs, H. Knöckel, T. Laue, C. Samuelis, and E. Tiemann. Observation of the last bound levels near the Na_2 ground-state asymptote. *Phys. Rev. A*, 59:3665–3672, 1999.

[71] F. K. Fatemi, K. M. Jones, P. D. Lett, and E. Tiesinga. Ultracold ground-state molecule production in sodium. *Phys. Rev. A*, 66:053401, 2002.

[72] P. Kusch and M. M. Hessel. An analysis of the $B^1\Pi_u X^1\Sigma_g^+$ band system of Na_2. *J. Chem. Phys.*, 68:2591, 1978.

[73] R.F. Barrow, J. Verges, C. Effantin, K. Hussein, and J. D'incan. Long-range potentials for the $X^1\Sigma_g^+$ And $(1)^1\Sigma_g$ states and the dissociation energy of Na_2. *Chemical Physics Letters*, 104(23):179–183, 1984.

[74] Li Li, Steven F. Rice, and R. W. Field. The Na_2 $a^3\Sigma_u^+$ state. Rotationally resolved OODR $^3\Pi_g - a^3\Sigma_u^+$ fluorescence spectroscopy. *J. Chem. Phys*, 82:1178, 1984.

[75] C. A. Stan, M. W. Zwierlein, C. H. Schunck, S. M. F. Raupach, and W. Ketterle. Observation of Feshbach Resonances between Two Different Atomic Species. *Phys. Rev. Lett.*, 93:143001, 2004.

[76] M. Gacesa, P. Pellegrini, and R. Côté. Feshbach resonances in ultracold ^{6,7}Li $+^{23}$ Na atomic mixtures. *Phys. Rev. A*, 78:010701, 2008.

[77] A. Derevianko, J. F. Babb, and A. Dalgarno. High-precision calculations of van der Waals coefficients for heteronuclear alkali-metal dimers. *Phys. Rev. A*, 63:052704, 2001.

[78] P. Raab and H. Friedrich. Quantization function for deep potentials with attractive tails. *Phys. Rev. A*, 78:022707, 2008.

[79] A. Marte, T. Volz, J. Schuster, S. Dürr, G. Rempe, E. G. M. van Kempen, and B. J. Verhaar. Feshbach Resonances in Rubidium 87: Precision Measurement and Analysis. *Phys. Rev. Lett.*, 89:283202, 2002.

[80] S. J. J. M. F. Kokkelmans, H. M. J. M. Boesten, and B. J. Verhaar. Role of collisions in creation of overlapping Bose condensates. *Phys. Rev. A*, 55:R1589–R1592, 1997.

[81] J. W. Park, C.-H. Wu, I. Santiago, T. G. Tiecke, P. Ahmadi, and M. W. Zwierlein. Quantum degenerate Bose-Fermi mixture of chemically different atomic species with widely tunable interactions. To be published in *Phys. Rev. A* Rapid Comm., 2012.

[82] A. Gerdes, M. Hobein, H. Knöckel, and E. Tiemann. Ground state potentials of the NaK molecule. *Eur. Phys. J. D*, 49(1):67–73, 2008.

[83] M. Steinke, H. Knöckel, and E. Tiemann. The $(X)1^1\Sigma^+$ state of LiNa studied by Fourier-transform spectroscopy. Accepted for publication in *Phys. Rev. A*, 2012.

[84] A. J. Moerdijk, W. C. Stwalley, R. G. Hulet, and B. J. Verhaar. Negative scattering length of ultracold ^{7}Li gas. *Phys. Rev. Lett.*, 72:40–43, 1994.

[85] C. C. Bradley, C. A. Sackett, and R. G. Hulet. Bose-Einstein Condensation of Lithium: Observation of Limited Condensate Number. *Phys. Rev. Lett.*, 78:985–989, 1997.

[86] M. R. Andrews, D. M. Kurn, H.-J. Miesner, D. S. Durfee, C. G. Townsend, S. Inouye, and W. Ketterle. Propagation of Sound in a Bose-Einstein Condensate. *Phys. Rev. Lett.*, 79:553–556, 1997.

[87] M. R. Andrews, D. M. Stamper-Kurn, H.-J. Miesner, D. S. Durfee, C. G. Townsend, S. Inouye, and W. Ketterle. Erratum: Propagation of Sound in a Bose-Einstein Condensate [Phys. Rev. Lett. 79, 553 (1997)]. *Phys. Rev. Lett.*, 80:2967–2967, 1998.

[88] T. Schuster, R. Scelle, A. Trautmann, S. Knoop, M. K. Oberthaler, M. M. Haverhals, M. R. Goosen, S. J. J. M. F. Kokkelmans, and E. Tiemann. Feshbach spectroscopy and scattering properties of ultracold Li+Na mixtures. Accepted for publication in *Phys. Rev. A*, 2012.

[89] W. Casteels. Effective mass in the weak Coupling regime. Private Communication, 2010.

[90] L. J. LeBlanc and J. H. Thywissen. Species-specific optical lattices. *Phys. Rev. A*, 75:053612, 2007.

[91] C. Raman, M. Köhl, R. Onofrio, D. S. Durfee, C. E. Kuklewicz, Z. Hadzibabic, and W. Ketterle. Evidence for a Critical Velocity in a Bose-Einstein Condensed Gas. *Phys. Rev. Lett.*, 83:2502–2505, 1999.

[92] A. P. Chikkatur, A. Görlitz, D. M. Stamper-Kurn, S. Inouye, S. Gupta, and W. Ketterle. Suppression and Enhancement of Impurity Scattering in a Bose-Einstein Condensate. *Phys. Rev. Lett.*, 85:483–486, 2000.

[93] D. E. Miller, J. K. Chin, C. A. Stan, Y. Liu, W. Setiawan, C. Sanner, and W. Ketterle. Critical Velocity for Superfluid Flow across the BEC-BCS Crossover. *Phys. Rev. Lett.*, 99:070402, 2007.

[94] C. Zipkes, S. Palzer, C. Sias, and M. Köhl. A trapped single ion inside a Bose-Einstein condensate. *Nature*, 464:388–391.

[95] B. Fröhlich, M. Feld, E. Vogt, M. Koschorreck, W. Zwerger, and M. Köhl. Radio-Frequency Spectroscopy of a Strongly Interacting Two-Dimensional Fermi Gas. *Phys. Rev. Lett.*, 106:105301, 2011.

[96] Ariel T. Sommer, Lawrence W. Cheuk, Mark J. H. Ku, Waseem S. Bakr, and Martin W. Zwierlein. Evolution of Fermion Pairing from Three to Two Dimensions. *Phys. Rev. Lett.*, 108:045302, 2012.

[97] P. Pedri and L. Santos. Three-Dimensional Quasi-Tonks Gas in a Harmonic Trap. *Phys. Rev. Lett.*, 91:110401, 2003.

[98] R. Grimm, M. Weidemüller, and Y. B. Ovchinnikov. Optical Dipole Traps for Neutral Atoms. volume 42 of *Advances In Atomic, Molecular, and Optical Physics*, pages 95–170. Academic Press, 2000.

[99] W. Zwerger. Mott-Hubbard transition of cold atoms in optical lattices. *J. Opt. B*, 5(2):S9, 2003.

[100] Elisabeth Brühl. A Species Selective Optical Dipole Trap for the NaLi Experiment. Master's thesis, Universität Heidelberg, 2011.

[101] Tim Rom. *Bosonische und fermionische Quantengase in dreidimensionalen optischen Gittern*. PhD thesis, Ludwig-Maximilians-Universität München, 2009.

[102] N. W. Ashcroft and N. D. Mermin. *Solid State Physics*. Cengage Learning Emea, 1976.

[103] A. Klöckner. On the Computation of Maximally Localized Wannier Functions. Master's thesis, University of Karlsruhe, 2004.

[104] Dieter Jaksch. *Bose-Einstein condensation and applications*. PhD thesis, Universität Innsbruck, 1999.

[105] Raphael Scelle. *To be published*. PhD thesis, Universität Heidelberg, 2013.

[106] M. B. Dahan, E. Peik, J. Reichel, Y. Castin, and C. Salomon. Bloch Oscillations of Atoms in an Optical Potential. *Phys. Rev. Lett.*, 76:4508–4511, 1996.

[107] M. Greiner, I. Bloch, O. Mandel, T. W. Hänsch, and T. Esslinger. Exploring Phase Coherence in a 2D Lattice of Bose-Einstein Condensates. *Phys. Rev. Lett.*, 87:160405, 2001.

[108] L. Viverit, C. Menotti, T. Calarco, and A. Smerzi. Efficient and Robust Initialization of a Qubit Register with Fermionic Atoms. *Phys. Rev. Lett.*, 93:110401, 2004.

[109] Markus Greiner. *Ultracold quantum gases in three-dimensional optical lattice potentials.* PhD thesis, Ludwig-Maximilians-Universität München, 2003.

[110] Henning Moritz. *One-dimensional Atomic Gases.* PhD thesis, Swiss Federal Institute of Technology, Zürich, 2006.

[111] M. Köhl, H. Moritz, T. Stöferle, K. Günter, and T. Esslinger. Fermionic Atoms in a Three Dimensional Optical Lattice: Observing Fermi Surfaces, Dynamics, and Interactions. *Phys. Rev. Lett.*, 94:080403, 2005.

[112] M. O. Scully and M. S. Zubairy. *Quantum Optics.* Cambridge University Press, 1997.

[113] A. Minguzzi, S. Conti, and M. P. Tosi. The internal energy and condensate fraction of a trapped interacting Bose gas. *J. Phys.: Condens. Matter*, 9(5):L33, 1997.

[114] R. Gati, B. Hemmerling, J. Fölling, M. Albiez, and M. K. Oberthaler. Noise Thermometry with Two Weakly Coupled Bose-Einstein Condensates. *Phys. Rev. Lett.*, 96:130404, 2006.

[115] E. L. Hahn. Spin Echoes. *Phys. Rev.*, 80:580–594, 1950.

[116] L. Gilz and J. R. Anglin. Quantum Kinetic Theory of Collisionless Superfluid Internal Convection. *Phys. Rev. Lett.*, 107:090601, 2011.

[117] W. Casteels, J. Tempere, and J. T. Devreese. Polaronic properties of an impurity in a Bose-Einstein condensate in reduced dimensions. *ArXiv*:1203.4420, 2012.

[118] M. Olshanii. Atomic Scattering in the Presence of an External Confinement and a Gas of Impenetrable Bosons. *Phys. Rev. Lett.*, 81:938–941, 1998.

[119] M. Feld, B. Fröhlich, E. Vogt, M. Koschorreck, and M. Köhl. Observation of a pairing pseudogap in a two-dimensional Fermi gas. *Nature*, 480:75–78, 2011.

[120] J. Levinsen and S. K. Baur. Ground state of an impurity in a quasi-two-dimensional Fermi gas. *ArXiv*:1202.6564, 2012.

[121] S. Chakravarty, A. Sudbo, P. W. Anderson, and S. Strong. Interlayer Tunneling and Gap Anisotropy in High-Temperature Superconductors. *Science*, 261(5119):337–340, 1993.

[122] M. A. Cazalilla and A. F. Ho. Instabilities in Binary Mixtures of One-Dimensional Quantum Degenerate Gases. *Phys. Rev. Lett.*, 91:150403, 2003.

[123] D. A. Steck. Sodium D Line Data, 2003.

[124] M. E. Gehm. Properties of ^{6}Li, 2003.

Danksagung

Der Schlüssel zum Erfolg ist Kameradschaft und der Wille, alles für den anderen zu geben.

Fritz Walter

An dieser Stelle möchte ich den Menschen danken, die – auf verschiedenste Art und Weise – entscheidend zum Gelingen dieser Arbeit beigetragen haben.

- Meinem Betreuer Herrn Prof. Dr. M. K. Oberthaler möchte ich recht herzlich dafür danken, dass er nach dem „Super-Gau“ ein NaLi 2.0 möglich gemacht hat und auch in schweren Stunden versucht hat, uns durch seine Begeisterung für die Physik und seinen Optimismus (der uns in solchen Situationen dann meist recht unangebracht schien) zu motivieren. Auch wenn seine „fetzigen“ Ideen die Grundrichtung des Experiments prägen, so hatte ich doch stets neben seinen Anregungen genug wissenschaftliche Freiheiten.

- Herrn Prof. Dr. S. Jochim für die Zweitkorrektur dieser Arbeit. Die Tipps, insbesondere was das Lithium-Setup angeht, waren ähnlich wichtig wie die gemeinsamen Pizza- und Feuerzangenbowle-Abende mit seiner Gruppe.

- Steven Knoop, der als Postdoc beim Wiederaufbau des NaLi Experiments großartiges geleistet hat. Nur holländisch fest geschraubte (Opto-)Mechanik hat er dadurch mehr als wett gemacht, dass er bei beiden Publikationen die treibende Kraft war, insbesondere bei der Lösung des NaLi Feshbach Resonanz Problems. Gemeinsame Grill- und Fußballabende - letztere wie wohl auch bei der kommenden EM meist mit negativem Ausgang für die Elftal - werden in guter Erinnerung bleiben.

- Raphael Scelle, der das NaLi-Experiment während der vergangenen vier Jahre geprägt hat wie kein anderer. Ohne seine sorgfältige Arbeit beim Wiederaufbau wären die meisten der Ergebnisse dieser Doktorarbeit nicht zustande gekommen. Aus (selten auftretenden) Meinungsverschiedenheiten in gemeinsamen Diskussionen über experimentellen Aufbau und Physik war es stets möglich, gemeinsam mit ihm produktiv das

Beste für das Experiment zu erarbeiten. Einen angenehmeren Kollegen hätte ich mir für die letzten dreieinhalb Jahre nicht wünschen können.

- Jens Appmeier für die Pionierarbeit bei NaLi 1.0 und seinen Beitrag zu NaLi 2.0, wo er im gemeinsamen Aufbau dank seines unerschöpflichen guten Humors über manche Durststrecke hinwegtrösten konnte. Glücklicherweise sind seine Fähigkeiten im Umgang mit der Grillzange besser als seine Kenntnis der ruhmreichen Fußballgeschichte des 1. FC Kaiserslautern.

- Arno Trautmann für den Interlock, den er zwar meist selbst in Anspruch nimmt, ohne den das Experiment aber schon mehrfach wieder abgebrannt wäre. Sein Sinn für gute Satire ist fast so ausgeprägt wie seine LaTeX-Kenntnisse, die auch zum Entstehen dieses Dokuments mehrfach dankbar in Anspruch genommen wurden.

- Tobias Rentrop, der sich trotz der Widerspenstigkeit des Experiments in der Anfangsphase seiner Doktorarbeit nicht entmutigen lässt und durch seinen trockenen Humor das Laborleben bereichert.

- Den Bachelor-Studenten Andrea Bergschneider, Elisabeth Brühl und Mathias Neidig, die weit über den Umfang ihrer Arbeit hinaus viel für das Experiment geleistet haben und Pionierarbeit beim Lithium-Laser-System sowie dem Gitteraufbau erbracht haben.

- Und zu guter Letzt, da das Ganze mehr ist als die Summe seiner Teile: Dem gesamten NaLi-Team, bei dem trotz sich ändernder Personalstruktur eine Sache stets gleich geblieben ist: Der Zusammenhalt, ohne den es mir nicht möglich gewesen wäre, mich jeden Tag aufs neue dem gemeinsamen Kampf gegen die Maschine auszusetzen und ihr auch das ein oder andere Ergebnis abzuringen.

- Gedankt sei hier auch den Fachkollegen aus Kollaborationen, die während dieser Arbeit entstanden sind. Besonders hervorzuheben sind hier Prof. Dr. E. Tiemann, der mit seiner Coupled-Channels Rechnung das NaLi Feshbach Resonanz Paper auf ein solides Fundament gestellt hat und Prof. Dr. A. Komnik, mit dem wir uns gemeinsam in vielen Diskussionen dem Polaron angenähert haben.

- Dank auch an Herrn Prof. Dr. P. Bachert für die Übernahme des angewandten Teils der Prüfung und aufschlussreiche Erklärungen zur NMR.

- Den Mitgliedern des BEC(K)-Experiments, insbesondere Helmut für seine Expertise in Elektronik und Tilman für hitzige, aber nichtsdestotrotz ergiebige Diskussionen über Physik und vieles mehr. Und allen dafür, dass ständig Equipment aus unserem Labor verschwindet und komischerweise im Nachbarlabor wieder auftaucht – „die [...] sind

raffiniert“ (V. A. Toni). Wenn nach B. Stromberg „Büro ist Krieg“ gilt, so wäre Labor mindestens Weltkrieg.

- Den ATTA-Mitgliedern für ihre Standhaftigkeit im Kampf gegen die Überinterpretation von Messdaten ($t = (500 \pm 500)$ Jahre).

- Dem Aegis-Experiment, insbesondere Fabienne Haupert für ihre stete Hilfsbereitschaft in Gruppen- und persönlichen Angelegenheiten.

- Den Mitfahrern und -fallern bei Stützrad, insbesondere den Gründungsmitgliedern Eike Nicklas und Christian Groß, mit denen es bei Wind und Wetter gemeinsam auf den Weißen Stein und den Königstuhl hoch ging. Des weiteren der Hochtourengruppe und Moritz Höfer, auf den man sich bei einem Spaltensturz hätte verlassen können.

- Den Mitglidern der Werkstatt, insbesondere Herrn Lamade, Morris Weißer für seine hervorragende Arbeit insbesondere beim Anfertigen der Spulenhalter, Herrn Herdt für seine einfallsreichen Lösungen bei Mechnik-Problemen und Herrn Spiegel für seine Nachsicht, wenn in der Diplomanden-Werkstatt mal wieder was unerklärlicherweise fast von selbst kaputt gegangen war.

- Den Mitgliedern der Elektronik-Abteilung, Jürgen Schölles als Ansprechpartner für alles, Alexander Leonhardt für unzählige Netzteilreparaturen, Herrn Azeroth für sichere Hochstromeinrichtungen und Herrn Kiworra für die Beantwortung aller Fragen zu Masseschleifen.

- Den „Team Assistants“ Dagmar Hufnagel und Christiane Jäger, die für einen reibungslosen Ablauf organisatorischer Dinge innerhalb der Gruppe, insbesondere der finanziellen Angelegenheiten sorgen.

- Der HGSFP und insbesondere Frau Prof. Dr. S. Klevansky für die hervorragende Graduiertenausbildung, die die Fakultät für Physik der Universität Heidelberg bietet.

- Der Klaus Tschira Stiftung für das großzügige Stipendium, das mir zur Verfügung gestellt wurde. Dank des erfreulich geringen Verwaltungsaufwands und der somit unkomplizierten Finanzierung meiner Promotion konnte ich meine Aufmerksamkeit fernab von Geldsorgen voll den Forschungsprojekten widmen.

- Der Laserbrücke zwischen KIP und Neuenheimer Feld, die in ihrer Sinnhaftigkeit nur durch ihre Tragfähigkeit überboten wurde. Und für deren Zustandekommen geht mein besonderer Dank an alle, die die Courage haben, die Wahrheit und nicht immer nur

„ja“ zu sagen.

- Martin Aeschlimann, der mir in schwierigen Situationen des Lebens stets beratend zur Seite stand.
- Michael Müller, der meinen Rücken immer wieder aufgerichtet hat, wenn er unter der Last der Arbeit und Probleme eingeknickt ist.
- Thomas Czarnecki für sein Mentoring in beruflichen Fragen.

- Meinen Freunden, auf die ich mich in guten und schlechten Zeiten verlassen kann. Danke an Frederik für viele gemeinsame Mittagessen, Nicki für gemeinsames Kochen und geteilten Humor, gracias a Antonia para bailar juntos y enseñarme español, Katharina für mehr als fünf Jahre Freundschaft, Stephan für so viele gemeinsame Gespräche über alle wichtigen Themen des Lebens und Martin für all das, was wir seit dem 1. Semester erlebt haben.

- Christoph und Bianca für gemeinsame Urlaube, geteilte Zeiten der Trauer und Momente des Glücks, und natürlich für eure Katzen. Und Christoph insbesondere dafür, dass er mich 24 Jahre lang ertragen hat und trotzdem noch mit mir redet.
- Meiner Mama dafür, dass sie meine Begeisterung für die Physik schon zu Schulzeiten geweckt hat. Aber auch außerfachlich hat sie mich stets in jeder Hinsicht unterstützt und ich habe mich in allen noch so verfahrenen Lebenslagen auf sie verlassen können. Dank auch an ihren Freund Reiner, auf dessen Hilfe stets Verlass ist.
- Meinem Papa, der das Ende dieser Doktorarbeit leider nicht mehr miterleben durfte. Sein bewundernswerter Kampfgeist und seine Aufmunterung „die Ohren steif zu halten“, mit der er mich auf Durststrecken jedweder Art zum Durchhalten motivierte, werden unvergessen bleiben.

- Meiner Freundin Anne, die mir weitaus mehr bedeutet, als dass ich es hier in Worte fassen könnte.

Enden möchte ich mit den versöhnlichen Worten des großen Johannes Brahms: „Und sollte ich vergessen haben, jemanden zu beschimpfen, dann bitte ich um Verzeihung!“